RESEARCH MEMORANDUM

TIME-VECTOR DETERMINED LATERAL DERIVATIVES OF A SWEPT-WING FIGHTER-TYPE AIRPLANE WITH THREE DIFFERENT VERTICAL TAILS AT MACH NUMBERS BETWEEN 0.70 AND 1.48

By Chester H. Wolowicz

High-Speed Flight Station
Edwards, Calif.

NATIONAL ADVISORY COMMITTEE
FOR AERONAUTICS
WASHINGTON
June 5, 1956

iP

NATIONAL ADVISORY COMMITTEE FOR AERONAUTICS

RESEARCH MEMORANDUM

TIME-VECTOR DETERMINED LATERAL DERIVATIVES OF A SWEPT-WING FIGHTER-TYPE AIRPLANE WITH THREE DIFFERENT VERTICAL TAILS AT MACH NUMBERS BETWEEN 0.70 AND 1.48

By Chester H. Wolowicz

SUMMARY

As part of the flight research program conducted on a swept-wing fighter-type airplane, rudder-pulse maneuvers were performed at altitudes from 30,000 to 43,000 feet over a Mach number range of 0.71 to 1.48 to determine the lateral stability characteristics relative to the stability axes, in general, and the lateral derivative characteristics, in particular. The time-vector method of analysis was used. Four configurations were employed in the investigation. Three configurations involved three different vertical tails with varying aspect ratio or area, or both. The fourth configuration employed a large tail, which had been used in the third configuration, and an extension of the wing tips.

The time-vector method of analysis is capable of producing good values of the lateral derivatives C_{Y_β}, C_{n_β}, C_{l_β}, and C_{l_p} providing the damping ratio is less than approximately 0.3. Reliable values of lateral derivatives $(C_{n_r} - C_{n_{\dot\beta}})$ are difficult to determine because of the sensitivity of this quantity to other factors. The expected effects of increasing vertical-tail size, resulting in increased magnitudes of C_{n_β}, C_{l_β}, and C_{l_p}, were realized. The addition of wing-tip extensions had small effects, except for a fairly large increase in the magnitude of the damping-in-roll derivative C_{l_p}. Theoretically calculated derivatives showed fair to good agreement with flight results in the subsonic range with the exception of high angle-of-attack values of $(C_{n_r} - C_{n_{\dot\beta}})$ derivatives. Wind-tunnel data for the static derivatives for a Mach number of 1.41, when corrected for torsional flexibility and air-intake effects of the jet engine, showed good agreement with flight results. The experimental rate of decrease in the magnitudes of C_{n_β}, C_{l_β}, and C_{l_p} with Mach number at Mach numbers greater than 1.25 was larger than estimated. This increased rate of decrease in magnitudes appears to be the result of possible shock wave and flow interference at the wing tips.

INTRODUCTION

This paper presents an application of the time-vector method of analysis in the determination of static and dynamic lateral derivatives of a 45° swept-wing fighter-type airplane. Details of the application of the time-vector method of analysis employed are also included in this paper as are some considerations of the limitations of the method. All data were obtained as part of a comprehensive investigation, conducted at the NACA High-Speed Flight Station at Edwards, Calif., of the lateral characteristics of this airplane.

The quantity of data obtained from the flight test program provided the first opportunity to perform a fairly detailed investigation of the stability characteristics of an airplane in the transonic and supersonic regions and to provide some comparison with available wind-tunnel data (ref. 1). Previous reports have presented the directional stability as determined by simple relationships (ref. 2) and the results of roll coupling investigations (refs. 3 to 6).

The flight rudder-pulse data for the determination of the lateral stability characteristics were obtained for four configurations. Three configurations employed the original wing and three different vertical-tail areas (original, extended, and large) while the fourth configuration employed an extended wing and the large tail. The data were obtained at altitudes between 30,000 and 43,000 feet over a Mach number range extending to 1.48. Most of the tests were performed at a nominal value of 1 g load factor, but for a few tests at nominal Mach numbers of 0.83 and 1.14 load factors within the range of 0.5g to 1.8g were used to investigate the influence of angle of attack on the lateral stability characteristics.

The results of the analysis of the data are compared with available wind-tunnel data and calculated derivatives.

SYMBOLS AND COEFFICIENTS

The results of this investigation are referred to the stability system of axes, which is defined as an orthogonal system of axes intersecting at the airplane center of gravity in which the Z-axis lies in the plane of symmetry and is perpendicular to the X-axis. The X-axis is in the plane of symmetry and is the projection in the XY-plane of the relative airstream onto the XZ-plane of symmetry. The Y-axis is perpendicular to the plane of symmetry.

[redacted]

The coefficients are referred to the original wing area and wing span.

a_n normal acceleration, g units

a_t corrected transverse acceleration, g units

a_{t_1} indicated transverse acceleration uncorrected for instrument position, g units

b wing span, ft

C_{L_0} trim 1 g lift coefficient, W/qS

C_l rolling-moment coefficient, $\frac{\text{Rolling moment}}{qSb}$

C_{l_p} damping-in-roll derivative, $\frac{\partial C_l}{\partial \frac{pb}{2V}}$, per radian

C_{l_r} rate of change of rolling-moment coefficient with yawing angular velocity factor, $\frac{\partial C_l}{\partial \frac{rb}{2V}}$, per radian

C_{l_β} effective dihedral derivative, $\frac{\partial C_l}{\partial \beta}$, per radian

$C_{l_{\dot{\beta}}}$ rate of change of rolling-moment coefficient with rate of change of angle-of-sideslip factor, $\frac{\partial C_l}{\partial \frac{\dot{\beta} b}{2V}}$, per radian

C_{l_δ} rate of change of rolling-moment coefficient with respect to control-surface displacement, $\frac{\partial C_l}{\partial \delta}$, per deg

C_n yawing-moment coefficient, $\frac{\text{Yawing moment}}{qSb}$

C_{n_p} rate of change of yawing-moment coefficient with rolling angular velocity factor, $\frac{\partial C_n}{\partial \frac{pb}{2V}}$, per radian

[redacted]

C_{n_r} rate of change of yawing-moment coefficient with yawing angular velocity factor, $\frac{\partial C_n}{\partial \frac{rb}{2V}}$, per radian

C_{n_β} directional stability derivative, $\frac{\partial C_n}{\partial \beta}$, per radian

$C_{n_{\dot{\beta}}}$ rate of change of yawing-moment coefficient with rate of change of angle-of-sideslip factor, $\frac{\partial C_n}{\partial \frac{\dot{\beta}b}{2V}}$, per radian

C_{n_δ} rate of change of yawing-moment coefficient with respect to control-surface displacement, $\frac{\partial C_n}{\partial \delta}$, per deg

C_Y lateral-force coefficient, $\frac{\text{Lateral force}}{qS}$

C_{Y_p} rate of change of lateral-force coefficient with rolling angular velocity factor, $\frac{\partial C_n}{\partial \frac{pb}{2V}}$, per radian

C_{Y_r} rate of change of lateral-force coefficient with yawing angular velocity factor, $\frac{\partial C_Y}{\partial \frac{rb}{2V}}$, per radian

C_{Y_β} lateral-force derivative, $\frac{\partial C_Y}{\partial \beta}$, per radian

$C_{Y_{\dot{\beta}}}$ rate of change of lateral-force coefficient with rate of change of angle-of-sideslip factor, $\frac{\partial C_Y}{\partial \frac{\dot{\beta}b}{2V}}$, per radian

C_{Y_δ} rate of change of lateral-force coefficient with respect to control-surface displacement, $\frac{\partial C_Y}{\partial \delta}$, per deg

c chord, ft

$\bar{c}$ mean aerodynamic chord, ft

[redacted]

g	acceleration of gravity, ft/sec^2
h_p	pressure altitude, ft
I_X	moment of inertia of airplane about stability X-axis, $I_{X_0} \cos^2\eta + I_{Z_0} \sin^2\eta$, slug-ft^2
I_{XZ}	product of inertia referred to stability X- and Z-axes, $-1/2\left(I_{Z_0} - I_{X_0}\right)\sin 2\eta$, slug-ft^2
I_Z	moment of inertia of airplane about stability Z-axis, $I_{Z_0} \cos^2\eta + I_{X_0} \sin^2\eta$, slug-ft^2
$I_{X_0}, I_{Y_0}, I_{Z_0}$	moments of inertia of airplane about principal longitudinal, lateral, and vertical axes, respectively, slug-ft^2
i_t	incidence angle of horizontal tail, positive leading edge up, deg
M	Mach number
m	mass of airplane, W/g, slugs
m_a	mass rate of air intake of jet engine, W_a/g, slugs/sec
P	period of damped natural frequency of airplane, sec
p'	rolling angular velocity factor, $pb/2V$, radians
q	dynamic pressure, $\frac{1}{2}\rho V^2$, lb/sq ft
$r, p, \dot{\beta}$	rate of change with time of ψ, φ, and β, respectively, radians/sec
$\dot{r}, \dot{p}$	rate of change with time of r and p, respectively, radians/sec^2
r'	yawing angular velocity factor, $rb/2V$, radians
S	wing area, sq ft
$T_{1/2}$	time required for absolute value of transient oscillation to damp to half amplitude, sec
t	time, sec

[redacted]

V airspeed, ft/sec

$\dot{v}$ transverse acceleration, ft/sec^2

W weight of airplane, lb

W_a weight rate of air intake of jet engine, lb/sec

x_a distance from center of gravity of airplane to air intake of jet engine (measured parallel to body X-axis), 25.1 ft

x_{a_t} distance from center of gravity to transverse accelerometer (measured parallel to body X-axis), positive when forward of center of gravity, 5.37 ft

x_β distance from center of gravity to sideslip vane (measured parallel to body X-axis), positive when forward of center of gravity, 30 ft

z_{a_t} distance from center of gravity to transverse accelerometer (measured perpendicular to body X-axis), positive when below center of gravity, -3.6 ft

z_β distance from center of gravity to sideslip vane (measured perpendicular to body X-axis), positive when below center of gravity, 2.5 ft

α angle of attack of airplane, angle between reference body X-axis and stability X-axis, deg

β corrected angle of sideslip, deg or radians

β_1 indicated angle of sideslip, measured from relative airstream to X-axis, positive when X-axis is left of airstream, deg

$\dot{\beta}'$ rate of change of sideslip factor, $\dot{\beta}b/2V$, radians

$\left(\Delta C_{n_\beta}\right)_a$ contribution of intake air of jet engine to directional stability derivative, $\frac{-m_a V x_a}{qSb}$, per radian

$\left(\Delta C_{Y_\beta}\right)_a$ contribution of intake air of jet engine to lateral-force derivative, $\frac{-m_a V}{qS}$, per radian

δ_{a_t} total aileron deflection, positive when left aileron is down, deg

[redacted]

δ_r rudder deflection, positive when rudder deflected to left, deg

ϵ angle between reference body X-axis and principal X-axis, positive when reference axis is above principal axis at the nose, deg

ζ ratio of actual damping to critical damping

η angle of inclination of principal X-axis of airplane relative to stability X-axis, positive when principal X-axis is above stability axis at the nose, $\alpha - \epsilon$, deg

ρ mass density of air, slugs/cu ft

τ time parameter, $m/\rho VS$, sec

σ angle of sidewash, radians

σ_β rate of change of angle of sidewash with angle of sideslip, $\partial\sigma/\partial\beta$

σ_p rate of change of angle of sidewash with rolling angular velocity factor, $\frac{\partial\sigma}{\partial\frac{pb}{2V}}$

Φ phase angle, deg

Φ_d damping angle, deg

φ angle of roll, positive when right wing moves down, radians

ψ angle of yaw, positive when airplane turns to right, radians

ω_n undamped natural frequency, radians/sec

ω_{n_d} damped natural frequency, $\omega_n\sqrt{1 - \zeta^2}$, radians/sec

$\left(C_{Y_{\beta_V}}\right)_F, \left(C_{n_{\beta_V}}\right)_F$, etc. contribution of flexible, vertical tail to the lateral-force, directional-stability derivatives, etc., respectively

$\left(C_{Y_{\beta_V}}\right)_R, \left(C_{n_{\beta_V}}\right)_R$, etc. contribution of the rigid, vertical tail to the lateral-force, directional-stability derivatives, etc., respectively

[redacted]

$\left(\Delta C_{Y_\beta}\right)_F, \left(\Delta C_{n_\beta}\right)_F$, etc. change in the contribution of vertical tail to lateral-force, directional-stability derivatives caused by flexibility of the vertical tail, etc., respectively

The symbol $|j|$ represents the absolute magnitude of a j quantity and is positive. When employed in an equation, the equation is considered to be a vector equation.

The phase angle of a vector j relative to another vector k is indicated by the subscript Φ_{jk}. The second subscript k is used as the reference. For example, in the expression $\Phi_{\varphi\psi} = -150^\circ$ the roll displacement vector lags the yaw displacement vector by 150°.

AIRPLANE

The airplane is a fighter-type with a single turbojet engine equipped with an afterburner, a moderately low swept wing, and a low horizontal tail. A three-view drawing of the airplane with the original vertical tail, tail A, is shown in figure 1. Figure 1 also indicates the extended wing. A photograph of the airplane is shown in figure 2.

The tests covered the following four configurations:

Configuration	Vertical tail	Wing
A	Small (A)	Original
B	Extended (B)	Original
C	Large (C)	Original
D	Large (C)	Extended

Figure 3 presents a photograph of tails A and C. Drawings of the three vertical tails are shown in figure 4. The same rudder was used on all tails.

The airplane is equipped with automatic leading-edge slats in five interconnected segments. At subsonic speeds the slats generally started to open at 3° to 6°. At supersonic speeds the slats generally remained closed at Mach numbers above 1.25 for the angle-of-attack range of the tests.

The physical characteristics of the various configurations are presented in table I. The estimated variation with airplane weight of the

principal moments of inertia and inclination of the principal axes (fig. 5) is based on the manufacturer's estimate (ref. 7) for design weight and empty weight conditions.

INSTRUMENTATION AND INSTRUMENT ACCURACY

Standard NACA instruments were used to record airspeed, altitude, rolling and yawing velocities and accelerations, normal acceleration, transverse acceleration, angles of attack and sideslip, and rudder, aileron, and stabilizer positions. The airspeed, altitude, and angles of attack and sideslip were sensed on the nose boom. All records were synchronized at 0.1-second intervals by a common timing circuit.

The turnmeters used to measure the angular velocities and accelerations were referenced to the body system of axes of the airplane and are considered accurate to within ±1.0 percent of scale range. Mounting direction errors were 0.5° or less.

The indicated normal and transverse accelerometer readings were corrected to the center of gravity. The accelerometers are considered accurate to within ±1.0 percent of scale range.

Indicated sideslip angles and angles of attack, measured by vane-type pickups, were corrected for roll and yaw rate, and pitch-rate effects, respectively. The pickups were mass damped and had dynamically flat frequency-response characteristics over the frequency range of the airplane. The pickups are statically accurate to ±0.1°.

The ranges, dynamic characteristics, and scale of recorded data for the angle of attack, sideslip, velocity, and acceleration instruments are:

Function	Range	Scale of recorded data (per inch deflection)	Undamped natural frequency, cps	Damping ratio
α, deg	-20 to 40	10.55	8	0.70
β, deg	±32	10.75	8	0.70
r, radians/sec . .	±0.5	0.543	10 to 12	0.65
$\dot{r}$, radians/sec^2 . .	±1	1.01	8	0.65
p, radians/sec . .	±4	4.19	20	0.64
$\dot{p}$, radians/sec^2 . .	±7	6.33	7	0.65
a_n, g units	-1 to 7	4.92	[a]19	[a]0.43
a_t, g units	±1	2.30	[b]13	[b]0.38

[a]30,000 feet.

[b]40,000 feet.

[redacted]

Rudder, aileron, and stabilizer positions were measured by standard control-position transmitters linked directly to the control surfaces. The transmitter-recorder system had a flat dynamic response over the frequency range of the control movements encountered. The transmitters are considered to be accurate to within ±0.1°.

The nose-boom installation for measuring the airspeed was calibrated by the NACA radar phototheodolite method. The Mach numbers presented are considered accurate to ±0.02 at speeds below about $M = 0.90$ and accurate to ±0.01 at speeds above $M = 0.90$.

Instrument phase-lag corrections were applied to all data employed in the analysis. Also, position corrections were applied by time-vector methods of analysis to sideslip and to transverse acceleration data. Details of the application of the time-vector method are considered in a later section of this paper.

TESTS

The test procedure for this investigation consisted of recording the airplane response to abrupt rudder pulses performed with other controls fixed. Attempts were made to maintain constant Mach number and altitude and to prevent inadvertent movement of the control surfaces during the transient portion of the maneuver. Such attempts were not always successful and required careful selection of usable portions of the flight record. Figures 6(a) and 6(b) present typical time histories. Small changes in altitude or Mach number did not appear to influence materially the results except in the region of the critical Mach number; however, moderate control movements in the transient portion of the maneuver influenced the analytical results. The most troublesome data resulted from maneuvers performed at high angles of attack or at other than 1 g.

Maneuvers were performed at 1 g ±0.1g conditions for the four configurations at altitudes ranging from 38,000 to 41,000 feet over a Mach number range of 0.73 to 1.35. To extend the Mach number range of the tests to 1.48, maneuvers were performed following a pullout from a dive. These maneuvers were performed with configurations B, C, and D at 35,000 ±3,000 feet over a load factor range of 1.2g to 1.7g.

To investigate the effects of angle of attack on the lateral stability characteristics maneuvers were performed with configurations C and D during turns and pushovers at Mach numbers of 0.73 to 1.18 at 40,000 ±2,000 feet and for configuration D at 30,000 ±2,000 feet.

[redacted]

Effects of angle of attack were also investigated over a Mach number range of 1.03 to 1.31 for configurations A and B at altitudes from 39,500 to 41,500 feet with a load factor of 1.7g to 2.1g for configuration A, and an altitude range of 37,500 to 39,500 feet with a load factor of 2.1g to 2.4g for configuration B.

ACCURACY OF RESULTS

In considering the probable errors in the analysis of the lateral characteristics of the airplane, attention must be given to instrument accuracy as well as to readability of the records, possible influences of variation in altitude and Mach number, influence of inadvertent movement of the controls, and accuracy of estimated derivatives.

The readability of the records was a strong potential source of error. Since the ranges of the instruments and scale factors employed were governed by the roll-coupling investigations being conducted at the time, the deflections on the roll records were small in general and very small at Mach numbers in excess of about 1.3.

With all factors considered, the probable errors in the flight data employed in the determination of derivatives are estimated to be:

	Probable error, percent
P:	
At M = 0.75	0.5
At M = 1.35	2
$T_{1/2}$	5 to 10
Φ_d	3 to 6
$\frac{\lvert\varphi\rvert}{\lvert\psi\rvert}$:	
Subsonic region $\frac{\lvert\varphi\rvert}{\lvert\psi\rvert} = 3.0$	3
Supersonic region $\frac{\lvert\varphi\rvert}{\lvert\psi\rvert} = 1.6$	6
$\Phi_{\varphi\psi}$	$\pm 3^\circ$

The probable errors in the lateral stability derivatives obtained from flight data are dependent on the degree of error in the estimated values of C_{n_p} and C_{l_r}, in the moments of inertia, and in the direction

of the principal axis, as well as the errors presented in the previous paragraph. The probable errors in the derivatives, exclusive of the influence of errors in the estimation of C_{n_p} and C_{l_r}, which will be discussed later, are believed to be:

Derivatives	Probable error, percent
C_{n_β}	3 to 5
C_{Y_β}	10
C_{l_β}:	
From M = 0.70 to 1.30	10
At M = 1.47	50
C_{l_p}:	
From M = 0.70 to 1.30	10
At M = 1.47	20
$\left(C_{n_r} - C_{n_{\dot\beta}}\right)$	15 to 20

PROCEDURES OF ANALYSIS

The original wing area and wing span were employed for all configurations in analyzing the flight data for the lateral stability derivatives. To convert the derivatives of the extended wing configuration (configuration D) to the actual wing area and wing-span bases, the C_{Y_β} derivative should be multiplied by 0.975, C_{n_β} and C_{l_β} by 0.925, and C_{l_p} and C_{n_r} by 0.876.

Inasmuch as the maximum sideslip and roll angles of the tests were of the order of 2° and 10°, respectively, and since no significant nonlinear or cross-coupling influences were noted, the following linearized, small disturbance forms of the lateral equations of motion of the airplane appeared applicable to the analysis of the data:

$$Wa_t = m(\dot v + rV - g\varphi) \tag{1}$$

$$Wa_t = \left(C_{Y_\beta}\beta + C_{Y_p}p' + C_{Y_r}r' + C_{Y_{\dot\beta}}\dot\beta'\right)qS \tag{2}$$

$$I_X\dot p - I_{XZ}\dot r = \left(C_{l_\beta}\beta + C_{l_p}p' + C_{l_r}r' + C_{l_{\dot\beta}}\dot\beta'\right)qSb \tag{3}$$

$$I_Z\dot r - I_{XZ}\dot p = \left(C_{n_\beta}\beta + C_{n_p}p' + C_{n_r}r' + C_{n_{\dot\beta}}\dot\beta'\right)qSb \tag{4}$$

[redacted]

Three methods were originally considered for the determination of the lateral stability derivatives. The frequency-response method of reference 8 was highly desirable because of the number of derivatives which can be determined from it; however, because of the time factor and some doubt as to the validity of the results which would be obtained using the available flight data, it was decided not to employ this method. The method of reference 9 is a time-vector approach to the solution of the derivatives; however, it is a tabular procedure employing successive approximations and therefore is not as desirable as the relatively rapid graphical time-vector method of analysis explained in references 10 to 12.

The graphical time-vector method of references 10 to 12 was employed for the determination of C_{Y_β}, C_{n_β}, $\left(C_{n_r} - C_{n_{\dot\beta}}\right)$, C_{l_β}, and C_{l_p}. The required precision of phase-angle data precluded the possibility of reliable values of $\left(C_{Y_r} - C_{Y_{\dot\beta}}\right)$ or C_{Y_p}; therefore it was decided, on a selective basis, to employ estimated values of C_{Y_p} and to ignore $\left(C_{Y_r} - C_{Y_{\dot\beta}}\right)$ in the solution. The values of C_{l_r} and C_{n_p} which were required for the time-vector solution of the other derivatives were obtained from theoretical estimates.

Application of the Time-Vector Method of Analysis

No attempt is made in this paper to present the detailed mathematical aspects of the fundamental time-vector properties inasmuch as reference 10 accomplishes this quite thoroughly. Suffice it to say that the time invariance of the phase relationships and amplitudes relative to each other permits the representation of any one of the linearized equations of motion by vectors. In the four lateral-directional equations three degrees of freedom are involved in each equation; namely, sideslip, roll, and yaw, each with the same frequency and damping characteristics. The amplitudes of the various degrees of freedom in each of the lateral-directional equations have the same shrinkage rate and the phase angles remain constant; thus for vector representation, the various amplitudes and phase relations are time invariant.

The vector properties described in the preceding paragraph, plus the requirement that the vector polygon representing any one equation must close, makes possible the determination of two unknowns in any one equation. Inasmuch as it is desired to determine the stability derivatives from flight data, it will be convenient to introduce new notations for the stability equations and to establish the equations in the form of amplitude ratios. All equations in this paper having absolute value notations will be considered to represent vector equations. Hence

$$2\tau \frac{|\dot{\beta}|}{|\beta|} + 2\tau \frac{|r|}{|\beta|} - C_{L_O} \frac{|\varphi|}{|\beta|} - C_{L_O} \frac{|a_t|}{|\beta|} = 0 \tag{5}$$

$$C_{L_O} \frac{|a_t|}{|\beta|} - C_{Y_p} \frac{|p'|}{|\beta|} - \left(C_{Y_r} - C_{Y_{\dot{\beta}}}\right) \frac{|r'|}{|\beta|} - C_{Y_\beta} = 0 \tag{6}$$

$$\frac{I_Z}{qSb} \frac{|\dot{r}|}{|\beta|} - \frac{I_{XZ}}{qSb} \frac{|\dot{p}|}{|\beta|} - C_{n_p} \frac{|p'|}{|\beta|} - \left(C_{n_r} - C_{n_{\dot{\beta}}}\right) \frac{|r'|}{|\beta|} - C_{n_\beta} = 0 \tag{7}$$

$$\frac{I_X}{qSb} \frac{|\dot{p}|}{|\beta|} - \frac{I_{XZ}}{qSb} \frac{|\dot{r}|}{|\beta|} - C_{l_p} \frac{|p'|}{|\beta|} - \left(C_{l_r} - C_{l_{\dot{\beta}}}\right) \frac{|r'|}{|\beta|} - C_{l_\beta} = 0 \tag{8}$$

The derivatives with respect to r and $\dot{\beta}$ have been combined in equations (6), (7), and (8). This was done because $|r|$ is similar to $|\dot{\beta}|$ and is approximately 180° out of phase with $|\dot{\beta}|$.

The amplitude ratio representation is convenient, inasmuch as it simplifies flight-data reduction and enables a more direct determination of some of the derivatives.

The period of oscillation P is determined directly from the transient portion of the flight record. To determine the indicated phase angles, the measured time differences of the different peaks of the various degrees of freedom were averaged and the simple expression

$$\Phi = \pm \frac{\Delta t}{P}(360°) \tag{9}$$

was utilized.

To determine indicated amplitude ratios relative to the body axes, the envelopes of the transient oscillation records are plotted on a semilogarithmic plot, such as figure 7, as a function of time. The linearity of the curves indicates that the linearized differential equation is applicable. The indicated amplitude ratios are then calculated as shown in figure 7.

The values of $T_{1/2}$ are determined as indicated in figure 7. The damping angle Φ_d is related to the damping ratio ζ by one of the relations

[redacted]

$$\Phi_d = \tan^{-1} \frac{\zeta}{\sqrt{1 - \zeta^2}} \qquad \text{damping angle}$$

$$= \sin^{-1}\zeta$$

$$= \cos^{-1}\sqrt{1 - \zeta^2} \tag{10}$$

The determination of Φ_d or ζ requires the use of the logarithmic decrement which may be expressed in various ways such as

$$\delta = \frac{2\pi\zeta}{\sqrt{1 - \zeta^2}} = 2\pi \tan \Phi_d \tag{11}$$

and

$$\delta = \frac{0.693}{T_{1/2}} P \qquad \text{damping factor} = P \tag{12}$$

Equating (11) and (12) and transposing

$$\tan \Phi_d = \frac{0.693}{2\pi} \frac{P}{T_{1/2}} = 0.1102 \frac{P}{T_{1/2}} \qquad \left.\begin{matrix}\\ \\ \end{matrix}\right\} \text{Solve these for } \Phi_d \tag{13}$$

Since $\omega_{n_d} = \omega_n\sqrt{1 - \zeta^2}$, then from (10) damped / natural frequency

$$\omega_n = \frac{\omega_{n_d}}{\cos \Phi_d} = \frac{2\pi}{P \cos \Phi_d} \tag{14}$$

Correction of Indicated Amplitude Ratios and Phase Angles

Amplitude ratios are subject to corrections for dynamic magnification, instrument location, and reorientation when the data are to be considered relative to axes other than the body axes about which the instruments are oriented. Phase angles are subject to corrections for phase lag in the electronic system, phase error caused by instrument location away from the center of gravity of the airplane, and reorientation when the data are to be considered relative to axes other than the body axes. The phase lag of the instruments was based on the relation

$$\Phi = \text{Phase lag} = -\tan^{-1} \frac{2\zeta\omega/\omega_{n_i}}{1 - \left(\frac{\omega}{\omega_{n_i}}\right)^2} = \text{deg} \qquad (15)$$

where

ω frequency of the airplane, radians/sec

ω_{n_i} undamped natural frequency of instrument, radians/sec

The indicated phase angles were corrected for the difference in the phase lag of the instruments involved.

The transverse accelerometer and β-vane records were subject to phase error caused by instrument location. These phase errors were determined in a vector approach to the correction of indicated amplitude ratios to true amplitude ratios.

The amplitude ratios will, in the case of carefully selected instruments, be subject to negligible dynamic amplification error. In the case of properly oriented gyroscopic instruments, the position error will be negligible and location error is not a factor to be considered. In the case of the transverse accelerometer and the β-vane instruments, location error may be important as on the present airplane.

To correct the β record for vane location, the following expression was employed

$$\beta = \beta_1 - \frac{x_\beta r_b}{V} + \frac{z_\beta p_b}{V} \qquad (16)$$

In terms of vector notations

$$\frac{|\beta|}{|\beta_1|} = 1 - \frac{x_\beta}{V}\frac{|r_b|}{|\beta_1|} + \frac{z_\beta}{V}\frac{|p_b|}{|\beta_1|} \qquad (17)$$

The graphical time-vector solution of (17) is shown in figure 8(a). The solution is obtained by first drawing in the direction of the vectors relative to β using the indicated phase angles corrected for instrument phase lag. The numerical values of the terms in (17) are then drawn in as vector quantities. The magnitude of the $\frac{|\beta|}{|\beta_1|}$ vector and its direction represent the magnification factor by which all the amplitude ratios taken

with respect to β should be divided to correct for β position error, and the phase angle error of all of the phase angles taken with respect to β.

To correct the indicated transverse acceleration for position error the following expression was used

$$a_t = a_{t_1} + \frac{z_{a_t}\dot{p}_b}{g} - \frac{x_{a_t}\dot{r}_b}{g} \tag{18}$$

In terms of vector notations

$$\frac{|a_t|}{|\beta|} = \frac{|a_{t_1}|}{|\beta|} + \frac{z_{a_t}}{g}\frac{|\dot{p}_b|}{|\beta|} - \frac{x_{a_t}}{g}\frac{|\dot{r}_b|}{|\beta|} \tag{19}$$

where

$$\frac{|\dot{p}_b|}{|\beta|} = \frac{|p_b|}{|\beta|}\omega_n$$

and

$$\frac{|\dot{r}_b|}{|\beta|} = \frac{|r_b|}{|\beta|}\omega_n$$

The time-vector solution of (19) is shown in figure 8(b). The solution is approached by first drawing in the directions of the p_b and r_b vectors. The directions of the acceleration vectors $\dot{p}_b$ and $\dot{r}_b$ are then located $(90^\circ + \Phi_d)$ ahead of the velocity vectors. The remainder of the solution is as shown in figure 8(a). It can be seen that the position correction is significant in the illustration representing actual test data of an average condition.

Determination of the Lateral Stability Derivatives

The stability derivatives being determined and the equations of motion employed in the present analysis are referenced to the stability axes. Inasmuch as the flight data are referenced to the body axes, it is necessary to transfer the flight data from the body axes to the stability axes. Had the stability derivatives sought been referenced to the body axes, then the stability equations referenced to the body axes would have been employed. In the appendix are presented the equations for the transfer of the amplitude ratio $\frac{|p|}{|r|}$ and the phase angle Φ_{pr} from the body axes to the stability axes. The appendix also outlines the vectorial

procedure employed in obtaining refined magnitudes of $\frac{|\psi|}{|\beta|}$ and $\frac{|\varphi|}{|\beta|}$ as well as phase angles with the aid of the transverse acceleration equation (5). Figure 8(c) illustrates the final vector solution for these magnitudes.

After correcting the data for various sources of error and transferring the data to the stability axes, as shown in the appendix, it is a simple matter to proceed with the determination of the derivatives. Since the positions of the displacement, velocity, and acceleration vectors are known, the three lateral-stability equations ((6) to (8)) may be applied to the solution of the lateral derivatives.

Figure 8(d) shows the vectorial solution for C_{Y_β} and $\left(C_{Y_r} - C_{Y_{\dot{\beta}}}\right)$. Although a solution for $\left(C_{Y_r} - C_{Y_{\dot{\beta}}}\right)$ is shown in the figure, this derivative was not included in the results of the analysis because of the lack of the required precision of the value of $\Phi_{a_t\beta}$ which would be needed to obtain a fairly reliable first approximation of this derivative.

Figure 8(e) shows the vector diagram for the determination of C_{n_β} and $\left(C_{n_r} - C_{n_{\dot{\beta}}}\right)$. No attempt was made to determine C_{n_p} in place of one of the other two derivatives, since some preliminary work appeared to indicate there would be no advantage in doing this. The section entitled "Discussion" in this paper considers sensitivity of some of the derivatives to experimental errors as well as limitations in the application of the time-vector method of analysis. Figure 8(f) shows the vector solution for C_{l_β} and C_{l_p}. In this solution $C_{l_{\dot{\beta}}}$ was neglected since $C_{l_r} \approx \left(C_{l_r} - C_{l_{\dot{\beta}}}\right)$.

Estimated Derivatives

For the static derivatives C_{Y_β}, C_{n_β}, and C_{l_β} available tail-off estimates based on wind-tunnel data were obtained from manufacturer's estimates. Wing contributions to the dynamic stability derivatives were estimated from the methods of references 13 to 18. The vertical-tail contributions to the static and dynamic stability derivatives were calculated, using the method of reference 19 and calculated lift-curve slopes (refs. 14, 17, and 20).

Manufacturer's estimates were utilized (fig. 9) for the effect of torsional flexibility on vertical-tail contributions to C_{Y_β}, C_{n_β}, C_{n_r}, and C_{Y_r} for tail C. The flexibility corrections were also applied to

the calculation of C_{l_β}. Figure 10 shows the estimated change in the derivatives caused by vertical-tail torsional flexibility in configurations C and D.

Two sidewash influences were considered to be acting on the vertical tail. The sidewash factor caused by roll σ_p was, on the basis of reference 19, estimated to be 0.25. The sidewash factor caused by sideslip σ_β has been shown in references 21 and 22 to be a function of wing position and influences the values of C_{Y_β}, C_{n_β}, C_{l_β}, and $\left(C_{n_r} - C_{n_{\dot{\beta}}}\right)$. From reference 22, σ_β was estimated to vary somewhat linearly for the angle-of-attack range of flight tests and was considered to vary from approximately 0.07 at $\alpha = 0^\circ$ to 0.11 at $\alpha = 6^\circ$.

The side force at the engine duct inlet resulting from the momentum change caused by bending of the intake air to flow along the duct axis was also taken into account in calculating C_{Y_β} and C_{n_β} of configurations C and D. No air-intake effects are considered when calculated derivatives on a rigid tail basis are presented. The air-intake effects were approximated by the equations

$$\left(\Delta C_{Y_\beta}\right)_a = \frac{-m_a V}{qS} \tag{20}$$

$$\left(\Delta C_{n_\beta}\right)_a = \frac{-m_a V x_a}{qSb} \tag{21}$$

Figure 11 shows the estimated weight rate of air required by the jet engine to maintain cruising speed. Figure 12 shows the estimated contribution of the intake air of the jet engine to C_{Y_β} and C_{n_β}.

PRESENTATION OF RESULTS

Following is a summary of the figures presenting the results of this investigation:

Limitations of the Time-Vector Method

	Figure
Influence of C_{n_p} and C_{l_r}	13
Influence of ±1-percent change in C_{n_β}	14
Influence of ±5-percent change in Φ_{pr}	15
Influence of ±0.5° change in Φ_d	16

[redacted]

Static and Dynamic Characteristics

Flight data results / Configuration	Figure			
	Trim, α	Period and damping	Amplitude ratios and phase angles	Static and dynamic lateral derivatives
A	17	18	19	20
B	17	21	22	23
C	17	24	25	26
D	17	27	28	29
Comparison of A, B, C, and D	--	30	31	32
Comparison of C and D with theory and wind tunnel	--	--	--	33
Angle-of-attack effects at M = 0.83 and M = 1.12	--	34	34	35

The data for configuration A, shown in figures 18 to 20, are meager in the subsonic region and most are subject to inadvertent control movements which, although not affecting the periods (fig. 18(a)) appreciably, do affect the damping (fig. 18(b)) and the phase angles (fig. 19(b)) so that no attempt was made to analyze these data for the 40,000-foot condition. The three test points at M = 0.71 constitute the only reliable damping characteristic points in the subsonic region and, as a result, the amplitude ratio curves of figure 19 indicate approximate values only. Despite the lack of sufficient subsonic data, the experimental stability derivative characteristics shown in figure 20 are considered to be reliable within the accuracy indicated previously.

Although period and damping curves are shown in figure 18 for a load factor of 1.8 at 40,000 feet, the amplitude ratios and phase angles for this condition were not sufficiently well defined to obtain derivatives.

The results of the analysis for configurations B, C, and D (figs. 21 to 29) are based on the availability of a larger amount of pulse data for each configuration. The data for configuration C were sufficient to define characteristic curves for trim level flight at 31,000 feet from M = 0.77 to M = 1.0 as well as for trim level flight at 40,000 feet (figs. 24 to 26).

DISCUSSION

Limitations in the Application of the Time-Vector Method of Analysis

Although the time-vector method of analysis requires the simplest of equipment in its application and is capable of providing good results, it does have definite limitations. In considering the limitations, it is presumed that flight records have clear, sharply defined traces, and that the ordinates have ample magnification in relation to the period scale to produce well-defined peaks in the oscillations.

One of the limitations in the application of the method is the inability to work with records of heavily damped airplanes without resorting to other methods of analysis, such as frequency-response analysis, to obtain amplitude ratios, phase angles, and angular frequency of the motion; and the use of template aids or analogs to determine the damping ratio. When the damping ratio ζ exceeds 0.2, the accuracy of defining $T_{1/2}$ begins to decrease. When ζ exceeds approximately 0.30, it is somewhat difficult to determine the period accurately and the $T_{1/2}$ values become increasingly doubtful. Also when ζ exceeds 0.4, reliability of P and $T_{1/2}$ becomes poor.

For controls-fixed conditions, the method depends on the analysis of the transient portion of an oscillatory motion. Any inadvertent application of a forcing function during this transient oscillatory motion, even though it may be small, will tend to influence the results. In instances where the forcing function is deliberate and is of a pure sinusoidal nature, the time-vector method is applicable providing the C_{Y_δ}, C_{n_δ}, and C_{l_δ} derivatives are available.

A third limitation of the time-vector method lies in the fact that only two of the three derivatives in each of the lateral equations may be determined by means of the vector diagram.

In the case of transverse equation (6), the secondary terms $C_{Y_p}\frac{|p'|}{|\beta|}$ and $\left(C_{Y_r} - C_{Y_{\dot{\beta}}}\right)\frac{|r'|}{|\beta|}$ are generally neglected and the result is

$$C_{Y_\beta} \approx C_{L_0}\frac{|a_t|}{|\beta|} \simeq \frac{W}{gS}\left|\frac{a_t}{\beta}\right| \qquad (22)$$

This simplified expression for C_{Y_β} provides answers which are high; however, the error probably does not exceed 4 percent. The principal

[redacted]

difficulties in obtaining refined values of C_{Y_β} have been in the readability of the records and the phase lag error of the vane itself. It should be recognized that the unknown phase lag of the vane would enter into the problem and affect the answers for C_{Y_β}, regardless of the method of analysis employed.

In the case of the rolling-moment equation (eq. (8)) it was deemed advisable to estimate the values of C_{l_r} and to obtain C_{l_β} and C_{l_p} from the vector diagram. The $C_{l_r}\frac{|r'|}{|\beta|}$ vector is relatively small, especially at high Mach numbers, and a normal error of $\pm 5^\circ$ in Φ_{pr} would result in no accuracy in attempting to determine C_{l_r}.

A limited investigation was made of the sensitivity of the determined derivatives to variations of the assumed values of C_{n_p} and C_{l_r}, to $\pm 5^\circ$ errors in Φ_{pr}, to $\pm 0.5^\circ$ error in damping angle, and to a ± 1 percent change in C_{n_β}. This investigation was considered for configuration C at $M = 0.80$ and $M = 1.20$ at 40,000 feet.

As shown in figure 13, C_{n_p} has a relatively small effect on C_{n_β} and a fairly large effect on $\left(C_{n_r} - C_{n_{\dot\beta}}\right)$. The effect on $\left(C_{n_r} - C_{n_{\dot\beta}}\right)$ was of the order of 0.029 and 0.017 units per 0.01 unit change in C_{n_p} at $M = 0.80$ and $M = 1.20$, respectively. The results of figure 13 show that C_{l_β} is affected less than 0.0004 units per 0.01 unit change in C_{l_r} and that C_{l_p} is affected 0.0037 and 0.0052 units at $M = 0.80$ and 1.20, respectively, per 0.01 unit change in C_{l_r}.

Normally, in dealing with the yawing-moment equation (eq. (7)), attempts are made to determine the $\left(C_{n_r} - C_{n_{\dot\beta}}\right)$ derivatives from vector diagrams. Thus, either C_{n_p} or C_{n_β} must be obtained by other means to permit completion of the solution. In the present paper a theoretical estimate of C_{n_p} was made and used to obtain both $\left(C_{n_r} - C_{n_{\dot\beta}}\right)$ and C_{n_β}. Inasmuch as there is usually some question of the accuracy of C_{n_p} estimations, some vector solutions of C_{n_p} and $\left(C_{n_r} - C_{n_{\dot\beta}}\right)$ were obtained using C_{n_β} as determined from

$$C_{n_\beta} = \frac{4\pi^2 I_Z}{qSb}\left[\frac{1}{P^2} + \frac{1}{4\pi^2}\left(\frac{0.693}{T_{1/2}}\right)^2\right] - C_{l_\beta}\frac{I_{XZ}}{I_X} \qquad (23)$$

[redacted]

In considering the possibility of employing calculated values of C_{n_β} to determine C_{n_p} and $\left(C_{n_r} - C_{n_{\dot{\beta}}}\right)$, values of C_{n_β} were obtained from equation (23) using faired flight data and vector solutions of C_{l_β}. The influence of a ±1-percent change in C_{n_β} on the lateral stability derivatives C_{n_p} and $\left(C_{n_r} - C_{n_{\dot{\beta}}}\right)$ is shown in figure 14. On the basis of the vector diagrams shown in figure 14, the influence would be appreciable. In view of the influence of small errors in C_{n_β} plus the effects of the possible magnitudes of errors in Φ_{pr} and Φ_d it was decided that, insofar as the present analysis is concerned, it would be better to employ theoretically estimated values of C_{n_p}.

Although the errors in the phase angle Φ_{pr} are believed to be generally within ±3° in the present paper, the error may approach ±5°. Figure 15 shows that a ±5° error had negligible influence on C_{n_β}, had a moderate effect on C_{l_β}, and pronounced effects on C_{l_p} and $\left(C_{n_r} - C_{n_{\dot{\beta}}}\right)$. A study of the vector diagrams in figure 15 will show that a decrease in the magnitude of $\frac{|\dot{p}|}{|\beta|}$ will reduce the influence of phase angle error in C_{n_β} and $\left(C_{n_r} - C_{n_{\dot{\beta}}}\right)$, but will also increase the influence on C_{l_β} and C_{l_p}. When the phase lag of the $\dot{p}$ vector $\Phi_{\dot{p}\beta}$ decreases toward 90°, the influence of the ±5° error on both C_{l_β} and C_{l_p} increases.

A ±0.5° error in the damping angle Φ_d showed small to moderate influence on $\left(C_{n_r} - C_{n_{\dot{\beta}}}\right)$, as shown in figure 16. In instances where $\left(C_{n_r} - C_{n_{\dot{\beta}}}\right)$ would be of the order of -0.10, the error would be pronounced.

Comparison of the Four Configurations

A summary of the results of the analysis of the flight data of the four configurations to show the influences of the various modifications on the stability characteristics is presented in figures 30 to 32.

The period characteristics (fig. 30(a)) show an appreciable decrease in the period when the original tail of configuration A was extended to form configuration B. Replacement of the extended tail by the large tail to form configuration C showed a moderate decrease in the period over the Mach number range. The extension of the wing in configuration C to form configuration D had a small uncertain effect on the period. The effects of the various modifications on the period characteristics are reflected

in the characteristics of the directional stability derivative C_{n_β} as seen in figure 32.

Although the damping characteristics (fig. 30(b)) show that $T_{1/2}$ was decreased in the subsonic range and increased in most of the supersonic range with each increase in tail size, the damping ratio ζ showed a decrease with each increase in tail size throughout the entire Mach number range investigated. The addition of wing-tip extensions, to form configuration D, appears to have negligible effect on both $T_{1/2}$ and ζ from $M = 0.71$ to about $M = 0.9$. Between $M = 0.9$ and $M = 1.37$, the addition of the wing tips appears to increase the damping.

The influence of the increase in vertical-tail sizes and the addition of the wing-tip extensions on the damping parameters $T_{1/2}$ and ζ is perhaps most effectively expressed in terms of derivatives as shown by approximate relationships based on the analytical expressions of reference 23. Although not exact, the following relationships, applicable to low angle-of-attack conditions, appear generally adequate for qualitative purposes:

$$T_{1/2} \approx \frac{1.386}{-\frac{qS}{V}\left[\frac{b^2}{2I_Z}\left(C_{n_r} - C_{n_{\dot{\beta}}}\right) + \frac{1}{m} C_{Y_\beta}\right]} \tag{24}$$

$$\zeta \approx -\sqrt{\frac{qSI_Z}{4b}} \frac{\left(\frac{b^2}{2I_Z}\left(C_{n_r} - C_{n_{\dot{\beta}}}\right) + \frac{1}{m} C_{Y_\beta}\right)}{\sqrt{C_{n_\beta} + \frac{I_{XZ}}{I_X} C_{l_\beta}}} \tag{25}$$

A study of equations (24) and (25) indicates that at any one value of dynamic pressure, $T_{1/2}$ is dominated by $\left(C_{n_r} - C_{n_{\dot{\beta}}}\right)$ and the damping ratio ζ is dominated by both $\left(C_{n_r} - C_{n_{\dot{\beta}}}\right)$ and C_{n_β}. The $\left(C_{n_r} - C_{n_{\dot{\beta}}}\right)$ derivative characteristics (fig. 32(b)) show qualitative trends with configuration which are, in general, compatible with the $T_{1/2}$ trends shown in figure 30.

The pertinent amplitude ratios are shown in figure 31. The characteristics curves of $\frac{|a_t|}{|\beta|}$ for the various configurations are somewhat erratic relative to each other because of the poor readability of the transverse acceleration flight records and the β-vane errors discussed previously.

[redacted]

In the subsonic range the large values of $\frac{|\varphi|}{|\beta|}$ of configuration A were markedly reduced by the various tail and wing modifications. In the supersonic region configuration A showed the lowest $\frac{|\varphi|}{|\beta|}$ magnitudes and an increase in vertical-tail area increased the ratio; however, the addition of extended tips decreased $\frac{|\varphi|}{|\beta|}$ slightly.

The phase angle $\Phi_{\varphi\beta}$ did not appear to be influenced in the subsonic range by the range of vertical-tail sizes covered, but the addition of the wing extensions had a more significant influence on the phase angle (fig. 31). In the supersonic region configuration A showed less lag in phase angle than did configurations B and C, which had practically identical phase-angle characteristics. Extension of the wing tips tended to decrease the lag.

In the Mach number range beyond $M = 1.2$ or 1.25 the amplitude ratio and phase-angle characteristics appear, in general, to be changing at an increasing rate. These changes in characteristic trend are reflected in the derivative characteristics shown in figure 32.

Figure 32 shows that an increase in both vertical-tail size and aspect ratio had desirable influences in the trim level-flight static derivative characteristics. Configuration C had practically double the directional stability of configuration A at $M = 0.7$, and approximately a 70-percent increase throughout the supersonic range. The influence of the different vertical tails on the directional stability has been reported previously in reference 2 relative to the body axis. When the C_{n_β} curve of this paper for configuration C and 40,000-foot altitude was transferred to body axes and compared with reference 2, excellent agreement was evident over the entire Mach number range.

The effective dihedral C_{l_β} was also subject to substantial increases with each increase in vertical-tail size. Wing-tip extensions had negligible effect. The rather sharp reduction in the negative value of C_{l_β} in the vicinity of the critical Mach number of about 0.96 is caused by the tail-off characteristics of the airplane. The deterioration of effective dihedral with increasing Mach number from $M \approx 1.23$, when considered in conjunction with the break in the C_{l_p} curves for configurations C and D, tends to indicate the possibility of shock wave and flow interference near the tips of the wings which influences the lift distribution across the span of the wing. Such an influence would reduce the effective dihedral C_{l_β} which tends to become negative in the region of $M = 1.38$ to $M = 1.47$, depending on the configuration.

[redacted]

The major influence of wing-tip extensions (configuration D) appeared to be on the C_{l_p} derivative. In the supersonic range between $M = 1.05$ and 1.30, there appears to be a fairly large increase in the negative value of the damping-in-roll derivative C_{l_p}. This indicated increase is based on the original wing area and span. When based on the actual wing area and span, the damping in roll for configuration D is larger than for configuration C up to $M \approx 1.31$.

In view of the difficulty in obtaining $\left(C_{n_r} - C_{n_{\dot{\beta}}}\right)$ derivatives and in an effort to check roughly the magnitudes of the $\left(C_{n_r} - C_{n_{\dot{\beta}}}\right)$ derivatives as obtained by the time-vector method, equation (24) was transposed to the following form to solve for $\left(C_{n_r} - C_{n_{\dot{\beta}}}\right)$:

$$\left(C_{n_r} - C_{n_{\dot{\beta}}}\right) \approx - \frac{2I_Z}{b^2}\left(\frac{1.386V}{qST_{1/2}} + \frac{1}{m} C_{Y_\beta}\right) \tag{26}$$

Utilizing the $T_{1/2}$ and C_{Y_β} values for configuration D (figs. 30 and 32), $\left(C_{n_r} - C_{n_{\dot{\beta}}}\right)$ was computed by using equation (26) and compared as shown in the following tabulation, with the values of $\left(C_{n_r} - C_{n_{\dot{\beta}}}\right)$ as determined by the time-vector method.

Mach number	0.90	1.05	1.15	1.25
$\left(C_{n_r} - C_{n_{\dot{\beta}}}\right)$ (eq. (26))	-0.34	-0.257	-0.239	-0.262
$\left(C_{n_r} - C_{n_{\dot{\beta}}}\right)$ by vectors	-0.29	-0.200	-0.205	-0.210

Inasmuch as equation (26) is approximate and tends to provide $\left(C_{n_r} - C_{n_{\dot{\beta}}}\right)$ values which are high (especially at higher angles of attack), it appears that the vector solutions for $\left(C_{n_r} - C_{n_{\dot{\beta}}}\right)$ are within reasonable limits and a rough insight as to the influence of the various configurations may be justified.

The negative magnitude of $\left(C_{n_r} - C_{n_{\dot{\beta}}}\right)$ appears to increase with increase in vertical-tail size in the subsonic range. Supersonically there appears to be a decrease in negative magnitude with increase in vertical-tail size. The addition of wing-tip extensions decreased the negative magnitude of $\left(C_{n_r} - C_{n_{\dot{\beta}}}\right)$ to some extent; supersonically the influence appears to be negligible.

Comparison With Calculated Characteristics and Wind-Tunnel Data

Two sets of calculated characteristics curves are shown in figure 33. The results show that air-intake effects and torsional flexibility of the tail have a pronounced influence on the calculated stability characteristics.

Beyond $M = 1.25$ all the flight-determined derivatives except $\left(C_{n_r} - C_{n_{\dot{\beta}}}\right)$ experience a deteriorating break in magnitude characteristics. The calculated C_{Y_β} and C_{n_β} characteristics indicate this break clearly; calculated C_{l_β} characteristics show only slight but similar trends starting at $M = 1.15$, calculated C_{l_p} characteristics indicate that damping in roll begins to deteriorate in the vicinity of $M = 1.35$.

Inasmuch as C_{l_p} is practically dependent on wing alone, the break in the C_{l_p} curve not accounted for by calculated values of this derivative appears to indicate, as mentioned in the previous section, the possibility of some shock wave and flow interference near the tip of the wings of both configurations which influences the lift distribution across the span of the wing. Such an influence would reduce the effective dihedral C_{l_β} which tends to become negative at a Mach number of approximately 1.47.

A comparison of the calculated derivatives with flight results showed fair to good agreement in the subsonic region for all derivatives except $\left(C_{n_r} - C_{n_{\dot{\beta}}}\right)$. The calculated values of $\left(C_{n_r} - C_{n_{\dot{\beta}}}\right)$, similar to the low-speed wind-tunnel values, were much lower than flight results.

Unpublished wind-tunnel static-stability data for $M = 1.41$ were corrected for vertical-tail flexibility and air-intake effects of the jet engine and are plotted in figure 33. These modified wind-tunnel data show good agreement with the flight-determined trend of C_{n_β} and C_{l_β}.

It is difficult to compare the low-speed wind-tunnel data with the subsonic flight results (fig. 33) because of the large Mach number difference. As will be pointed out in the following section, the variation of C_{Y_β}, C_{n_β}, and C_{l_p} with angle of attack shown by wind-tunnel data is the opposite of trends shown by flight results; however, it appears that the magnitudes of C_{l_β} and C_{l_p} from flight and wind-tunnel data tend to agree.

[redacted]

Variation of Stability Characteristics With Angle of Attack

Although available flight data permitted the presentation of constant load factor curves for several of the lateral characteristics in the supersonic region for configurations A and B (figs. 18 to 21), and data were also available for the presentation of the lateral characteristics in the subsonic region for altitude effects for configuration C (figs. 24 to 26), no attempt is made in this paper to discuss the results inasmuch as other flight data provided a more detailed insight into the variation of the lateral stability characteristics with angle of attack at Mach numbers of 0.81 and 1.14.

The variation of the lateral stability characteristics with angle of attack at $M = 0.83$ at altitudes of 40,000 and 31,000 feet for configurations C and D, and at $M = 1.14$ at an altitude of 40,000 feet for configuration C are shown in figures 34 and 35. Also shown in figure 35 are the variations of C_{n_β}, C_{l_β}, C_{l_p}, and $\left(C_{n_r} - C_{n_{\dot{\beta}}}\right)$ with angle of attack as obtained from reference 1 for a Mach number of 0.13.

As shown in figure 34, flight data indicate a decrease in period with increasing angle of attack regardless of the Mach number or altitude. The damping characteristics improve with both increasing angle of attack and decreasing altitude.

The amplitude ratio $\frac{|\varphi|}{|\beta|}$ and the phase lag of $\Phi_{\varphi\beta}$ increase with angle of attack. Increasing angle of attack tends to place the roll and sideslip displacements in phase. This tendency, plus the increase in roll angle per unit sideslip angle, tends to accentuate Dutch roll tendencies of the airplane.

Figure 35 shows the trends of the variation of the derivatives with angle of attack. The C_{Y_β} derivative is not included because the scatter of the flight results precluded the possibility of presenting a definite trend of C_{Y_β} variation with angle of attack at constant Mach number. Although low-speed wind-tunnel data from reference 1 are shown for comparison with flight results at $M = 0.83$ and $M = 1.14$, a direct comparison for the same Mach number conditions is difficult because of the presence of automatic leading-edge slats on the airplane and the large difference in Mach number which would make extrapolation unreliable.

Flight results indicate an increase in directional stability and effective dihedral with increasing angle of attack.

The damping-in-roll derivative C_{l_p} appears to attain its maximum magnitude at an angle of attack of about 3°.

[redacted]

CONCLUSIONS

From the analysis of flight data obtained for four configurations of a swept-wing fighter-type airplane over the Mach number range from 0.7 to 1.48 the following conclusions have been reached:

1. The time-vector method of analysis is capable of producing good values of the lateral derivatives C_{Y_β}, C_{n_β}, C_{l_β}, and C_{l_p} providing the damping ratio is less than approximately 0.3. Reliable values of lateral derivatives $\left(C_{n_r} - C_{n_{\dot{\beta}}}\right)$ are difficult to determine because of the sensitivity of this quantity to other factors.

2. The expected effects of increasing vertical-tail size, resulting in increased magnitudes of C_{n_β}, C_{l_β}, and C_{l_p}, were realized.

3. The addition of wing-tip extensions had small effects, except for a fairly large increase in the magnitude of the damping-in-roll derivative C_{l_p}.

4. Theoretically calculated derivatives showed fair to good agreement with flight results in the subsonic range with the exception of high angle-of-attack values of $\left(C_{n_r} - C_{n_{\dot{\beta}}}\right)$ derivatives. Wind-tunnel data for the static derivatives for a Mach number of 1.41, when corrected for torsional flexibility and air-intake effects of the jet engine, showed good agreement with flight results.

5. The experimental rate of decrease in the magnitudes of C_{n_β}, C_{l_β}, and C_{l_p} with Mach number at Mach numbers greater than 1.25 was larger than estimated. This increased rate of decrease in magnitudes appears to be the result of possible shock wave and flow interference at the wing tips.

High-Speed Flight Station,
National Advisory Committee for Aeronautics,
Edwards, Calif., March 9, 1956.

APPENDIX

TRANSFER OF AMPLITUDE RATIOS AND PHASE ANGLES FROM BODY AXES TO STABILITY AXES

The transfer of the amplitude ratios and phase angles from body axes to stability axes was accomplished by the use of equations for the transfer of $\frac{|p_b|}{|r_b|}$ and $\Phi_{p_b r_b}$ to the stability axes, and the use of the vector method to obtain $\frac{|\varphi|}{|\beta|}$, $\frac{|\psi|}{|\beta|}$, $\Phi_{\varphi\beta}$, and $\Phi_{\psi\beta}$.

To transfer $\frac{|p_b|}{|r_b|}$ and $\Phi_{p_b r_b}$ to the stability axes, the following equations from reference 9 were employed

$$\frac{|p|}{|r|} = \sqrt{\frac{\left(\frac{|p_b|}{|r_b|}\cos\Phi_{p_b r_b} + \tan\alpha\right)^2 + \left(\frac{|p_b|}{|r_b|}\sin\Phi_{p_b r_b}\right)^2}{\left(1 - \frac{|p_b|}{|r_b|}\cos\Phi_{p_b r_b}\tan\alpha\right)^2 + \left(\frac{|p_b|}{|r_b|}\sin\Phi_{p_b r_b}\tan\alpha\right)^2}} \tag{A1}$$

and

$$\Phi_{pr} = \tan^{-1}\left(\frac{\frac{|p_b|}{|r_b|}\sin\Phi_{p_b r_b}}{\frac{|p_b|}{|r_b|}\cos\Phi_{p_b r_b} + \tan\alpha}\right) - \tan^{-1}\left(\frac{-\frac{|p_b|}{|r_b|}\sin\Phi_{p_b r_b}\tan\alpha}{1 - \frac{|p_b|}{|r_b|}\cos\Phi_{p_b r_b}\tan\alpha}\right) \tag{A2}$$

The amplitude ratios $\frac{|\varphi|}{|\beta|}$ and $\frac{|\psi|}{|\beta|}$ and the phase angles $\Phi_{r\beta}$ and $\Phi_{\psi\beta}$ were obtained vectorially with the aid of the transverse acceleration equation (5) as shown in figure 8(c). In approaching this analysis the directions of the a_t and β vectors are drawn as shown and, since neither $\frac{|\varphi|}{|\beta|}$ nor the direction of the φ vector is known, first approximations are made for these quantities as follows:

[redacted]

$$\frac{|\varphi|}{|\beta|} \approx \frac{|p|}{|r|} \tag{A3}$$

$$\Phi_{\varphi\beta} \approx \Phi_{\varphi\psi} + 180^\circ \tag{A4}$$

and

$$\Phi_{\psi\beta} \approx 180^\circ \tag{A5}$$

where

$$\frac{|p|}{|r|} = \frac{|\varphi|}{|\psi|} \quad \text{and} \quad \beta \approx \psi$$

As a result of these first approximations, the vector diagram is drawn as shown. The closing vector $2\tau \frac{|r|}{|\beta|}$ determines the first approximation of the direction of the r vector from which the second approximation of the ψ vector direction is determined to obtain the second approximation of the φ vector direction using Φ_{pr}.

To obtain the second approximation of $\frac{|\varphi|}{|\beta|}$, divide $2\tau \frac{|r|}{|\beta|}$ by $2\tau \frac{|\beta|}{|\beta|}$ to obtain the first approximation of $\frac{|\psi|}{|\beta|}$ and multiply this value of $\frac{|\psi|}{|\beta|}$ by $\frac{|p|}{|r|}$.

Using the second approximation of $\frac{|\varphi|}{|\beta|}$ and direction of the ψ vector, the second approximation of $C_{I_O} \frac{|\varphi|}{|\beta|}$ is determined and redrawn on the vector diagram to obtain a new value of $2\tau \frac{|r|}{|\beta|}$ and direction of the r vector. This second approximation of $2\tau \frac{|r|}{|\beta|}$ is now used to obtain a second approximation of $\frac{|\psi|}{|\beta|}$ and a third approximation of $\frac{|\varphi|}{|\beta|}$.

It has been found that the direction of the r vector and the magnitudes of $\frac{|\psi|}{|\beta|}$ and $\frac{|\varphi|}{|\beta|}$ determined by carrying the successive approximations thus far are quite close to the values which would be obtained had the successive approximation procedure continued to complete convergence.

Having determined $\frac{|\psi|}{|\beta|}$, $\frac{|\varphi|}{|\beta|}$, and the direction of the r vector, it is a simple matter to obtain the phase angles $\Phi_{\psi\beta}$ and $\Phi_{\varphi\beta}$.

[redacted]

REFERENCES

1. Jaquet, Byron M., and Fletcher, H. S.: Wind-Tunnel Investigation at Low Speed of Sideslipping, Rolling, Yawing, and Pitching Characteristics for a Model of a 45° Swept-Wing Fighter-Type Airplane. NACA RM L55F21, 1955.

2. Drake, Hubert M., Finch, Thomas W., and Peele, James R.: Flight Measurements of Directional Stability to a Mach Number of 1.48 for an Airplane Tested With Three Different Vertical Tail Configurations. NACA RM H55G26, 1955.

3. NACA High-Speed Flight Station: Flight Experience With Two High-Speed Airplanes Having Violent Lateral-Longitudinal Coupling in Aileron Rolls. NACA RM H55A13, 1955.

4. Weil, Joseph, Gates, Ordway B., Jr., Banner, Richard D., and Kuhl, Albert E.: Flight Experience of Inertia Coupling in Rolling Maneuvers. NACA RM H55E17b, 1955.

5. Finch, Thomas W., Peele, James R., and Day, Richard E.: Flight Investigation of the Effect of Vertical-Tail Size on the Rolling Behavior of a Swept-Wing Airplane Having Lateral-Longitudinal Coupling. NACA RM H55L28a, 1956.

6. Weil, Joseph, and Day, Richard E.: An Analog Study of the Relative Importance of Various Factors Affecting Roll Coupling. NACA RM H56A06, 1956.

7. Weight Control Section, N.A.A.: Airplane Inertia Calculations for an Air Superiority Fighter Airplane - Day (Monoplane), AF Model F-100A (NAA Model NA-192). Rep. No. NA-52-185 (Contract No. AF33(600) - 6545), North American Aviation, Inc., Oct. 1953.

8. Donegan, James J., Robinson, Samuel W., Jr., and Gates, Ordway B., Jr.: Determination of Lateral-Stability Derivatives and Transfer-Function Coefficients From Frequency-Response Data for Lateral Motions. NACA TN 3083, 1954.

9. Rosamond, D. L.: Practical Methods for Lateral Stability Analysis. Rep. No. 2126, McDonnell Aircraft Corp., June 12, 1951.

10. Breuhaus, W. O.: Resumé of the Time Vector Method as a Means for Analyzing Aircraft Stability Problems. WADC Tech. Rep. 52-299 (Contract No. AF33(038)-20659 RDO No. 461-1-2), Wright Air Dev. Center, U. S. Air Force, Nov. 1952.

11. Larrabee, E. E.: Application of the Time-Vector Method to the Analysis of Flight Test Lateral Oscillation Data. FRM No. 189, Cornell Aero, Lab. Inc., Sept. 9, 1953.

12. Sternfield, L.: A Vector Method Approach to the Analysis of the Dynamic Lateral Stability of Aircraft. Jour. Aero. Sci., vol. 21, no. 4, Apr. 1954, pp. 251-256.

13. Toll, Thomas A., and Queijo, M. J.: Approximate Relations and Charts for Low-Speed Stability Derivatives of Swept Wings. NACA TN 1581, 1948.

14. Fisher, Lewis R.: Approximate Corrections for the Effects of Compressibility on the Subsonic Stability Derivatives of Swept Wings. NACA TN 1854, 1949.

15. DeYoung, John: Theoretical Antisymmetric Span Loading for Wings of Arbitrary Plan Form at Subsonic Speeds. NACA Rep. 1056, 1951. (Supersedes NACA TN 2140.)

16. Margolis, Kenneth: Theoretical Calculations of the Lateral Force and Yawing Moment Due to Rolling at Supersonic Speeds for Sweptback Tapered Wings With Streamwise Tips. Subsonic Leading Edges. NACA TN 2122, 1950.

17. Malvestuto, Frank S., Jr., Margolis, Kenneth, and Ribner, Herbert S.: Theoretical Lift and Damping in Roll at Supersonic Speeds of Thin Sweptback Tapered Wings With Streamwise Tips, Subsonic Leading Edges, and Supersonic Trailing Edges. NACA Rep. 970, 1950. (Supersedes NACA TN 1860.)

18. Jones, Arthur L., and Alksne, Alberta: A Summary of Lateral-Stability Derivatives Calculated for Wing Plan Forms in Supersonic Flow. NACA Rep. 1052, 1951.

19. Letko, William, and Riley, Donald R.: Effect of an Unswept Wing on the Contribution of Unswept-Tail Configurations to the Low-Speed Static- and Rolling-Stability Derivatives of a Midwing Airplane Model. NACA TN 2175, 1950.

20. DeYoung, John, and Harper, Charles W.: Theoretical Symmetric Span Loading at Subsonic Speeds for Wings Having Arbitrary Plan Form. NACA Rep. 921, 1948.

21. Goodman, Alex: Effects of Wing Position and Horizontal-Tail Position on the Static Stability Characteristics of Models With Unswept and 45° Sweptback Surfaces With Some Reference to Mutual Interference. NACA TN 2504, 1951.

[redacted]

22. Fisher, Lewis R., and Fletcher, Herman S.: Effect of Lag of Sidewash on the Vertical-Tail Contribution to Oscillatory Damping in Yaw of Airplane Models. NACA TN 3356, 1955.

23. Triplett, William C., and Brown, Stuart C.: Lateral and Directional Dynamic-Response Characteristics of a 35° Swept-Wing Airplane as Determined From Flight Measurements. NACA RM A52I17, 1952.

TABLE I.- PHYSICAL CHARACTERISTICS OF AIRPLANE

	Basic wing	Basic wing plus wing-tip extensions
Wing:		
Airfoil section	NACA 64A007	NACA 64A007
Total area (including aileron and 83.84 sq ft covered by fuselage), sq ft	376.02	385.21
Span, ft	36.58	38.58
Mean aerodynamic chord, ft	11.33	11.16
Root chord, ft	15.86	15.86
Tip chord, ft	4.76	4.15
Taper ratio	0.30	0.262
Aspect ratio	3.56	3.86
Sweep at 0.25 chord line, deg	45	45
Incidence, deg	0	0
Dihedral, deg	0	0
Geometric twist, deg	0	0
Aileron:		
Area rearward of hinge line (each), sq ft	19.32	19.32
Span at hinge line (each), ft	7.81	7.81
Chord rearward of hinge line, percent wing chord	25	25
Travel (each), deg	±15	±15
Leading-edge slat:		
Span, equivalent, ft	12.71	12.71
Segments	5	5
Spanwise location, inboard end, percent wing semispan	24.6	23.3
Spanwise location, outboard end, percent wing semispan	94.1	89.2
Ratio of slat chord to wing chord (parallel to fuselage reference line), percent	20	20
Rotation, maximum, deg	15	15
Horizontal tail:		
Airfoil section		NACA 65A003.5
Total area (including 31.65 sq ft covered by fuselage), sq ft		98.86
Span, ft		18.72
Mean aerodynamic chord, ft		5.83
Root chord, ft		8.14
Tip chord, ft		2.46
Taper ratio		0.30
Aspect ratio		3.54
Sweep at 0.25 chord line, deg		45
Dihedral, deg		0
Travel, leading edge up, deg		5
Travel, leading edge down, deg		25
Irreversible hydraulic boost and artificial feel		

TABLE I.- PHYSICAL CHARACTERISTICS OF AIRPLANE - Concluded

	A	B	C
Vertical tail:			
Airfoil section	NACA 65A003.5	NACA 65A003.5	NACA 65A003.5
Area (excluding dorsal fin and area blanketed by fuselage), sq ft	33.5	37.3	42.7
Area blanketed by fuselage (area between fuselage contour line and line parallel to fuselage reference line through intersections of leading edge of vertical tail and fuselage contour line)	2.11	2.11	2.45
Span (unblanketed), ft	6.14	7.45	7.93
Mean aerodynamic chord, ft	5.85	5.51	5.90
Root chord, ft	7.75	7.75	8.28
Tip chord, ft	3.32	2.32	2.49
Taper ratio	0.428	0.301	0.301
Aspect ratio	1.13	1.49	1.49
Sweep at 0.25 chord line, deg	45	45	45
Rudder:			
Area, rearward of hinge line, sq ft	6.3	6.3	6.3
Span at hinge line, ft	3.33	3.33	3.33
Root chord, ft	2.27	2.27	2.27
Tip chord, ft	1.50	1.50	1.50
Travel, deg	±20	±20	±20
Spanwise location, inboard end, percent vertical tail span	4.5	3.7	3.1
Spanwise location, outboard end, percent vertical tail span	58.2	48.0	44.8
Chord, percent vertical tail chord	30.0	30.0	28.4
Aerodynamic balance	Overhanging; unsealed	Overhanging, unsealed	Overhanging, unsealed

Fuselage:	
Length (afterburner nozzle closed), ft	45.64
Maximum width, ft	5.58
Maximum depth over canopy, ft	6.37
Side area (total), sq ft	230.92
Fineness ratio (afterburner nozzle closed)	7.86
Speed brake:	
Surface area, sq ft	14.14
Maximum deflection, deg	50
Power plant:	
Turbojet engine	One Pratt & Whitney J57-P7 with afterburner
Thrust (guarantee sea level), afterburner, lb	15,000
Military, lb	9,220
Normal, lb	8,000
Airplane weight, lb:	
Basic (without fuel, oil, water, pilot)	19,662
Total (full fuel, oil, water, pilot)	24,800
Center-of-gravity location, percent $\bar{c}$:	
Total weight - gear down	29.5
Total weight - gear up	29.5

For moments of inertia and inclination of principal axis, refer to figure 5.

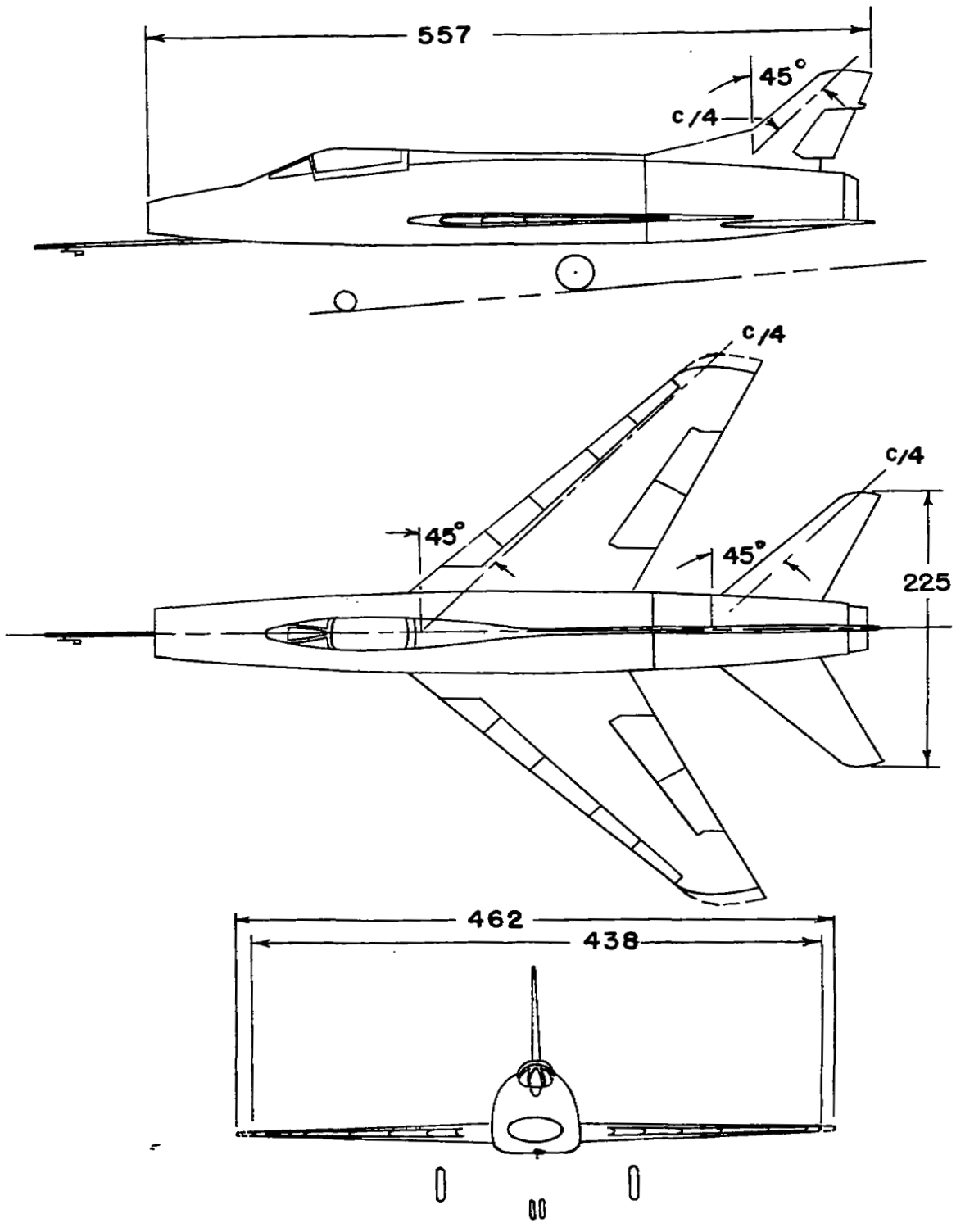

Figure 1.- Three-view drawing of airplane with original vertical tail and the extended as well as the original wing. All dimensions in inches.

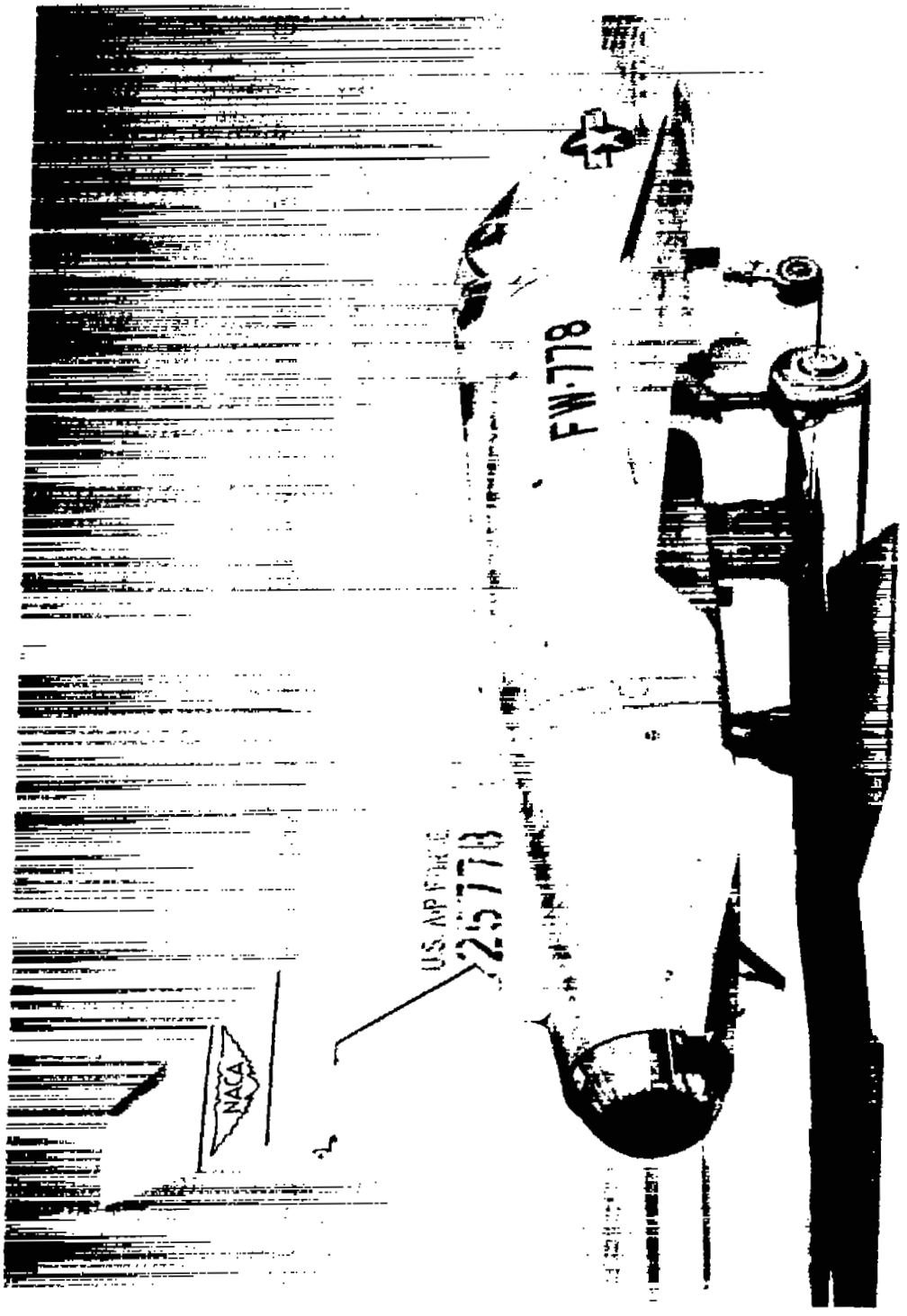

E-2089

Figure 2.- Photograph of the airplane.

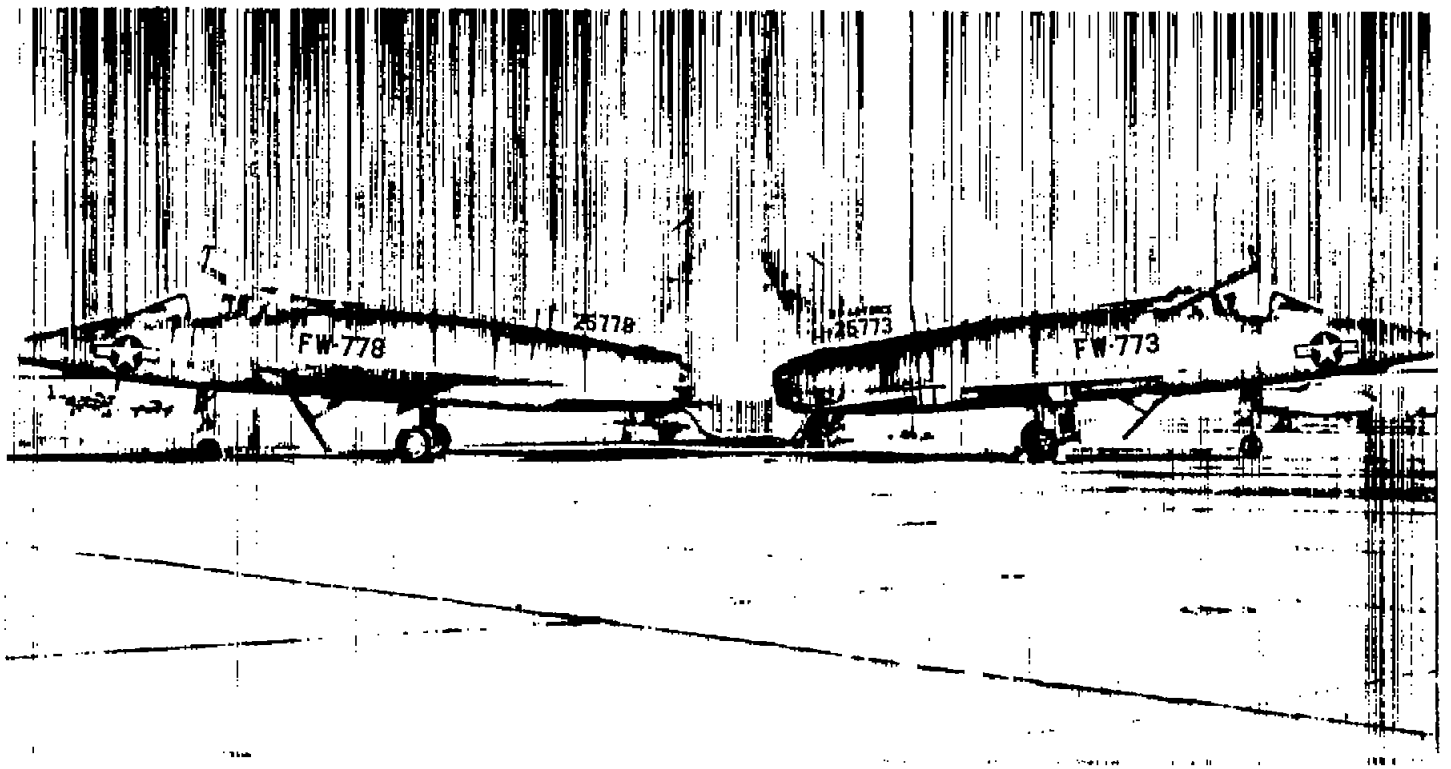

E-1622

Figure 3.- Photograph of two airplanes showing tails A and C.

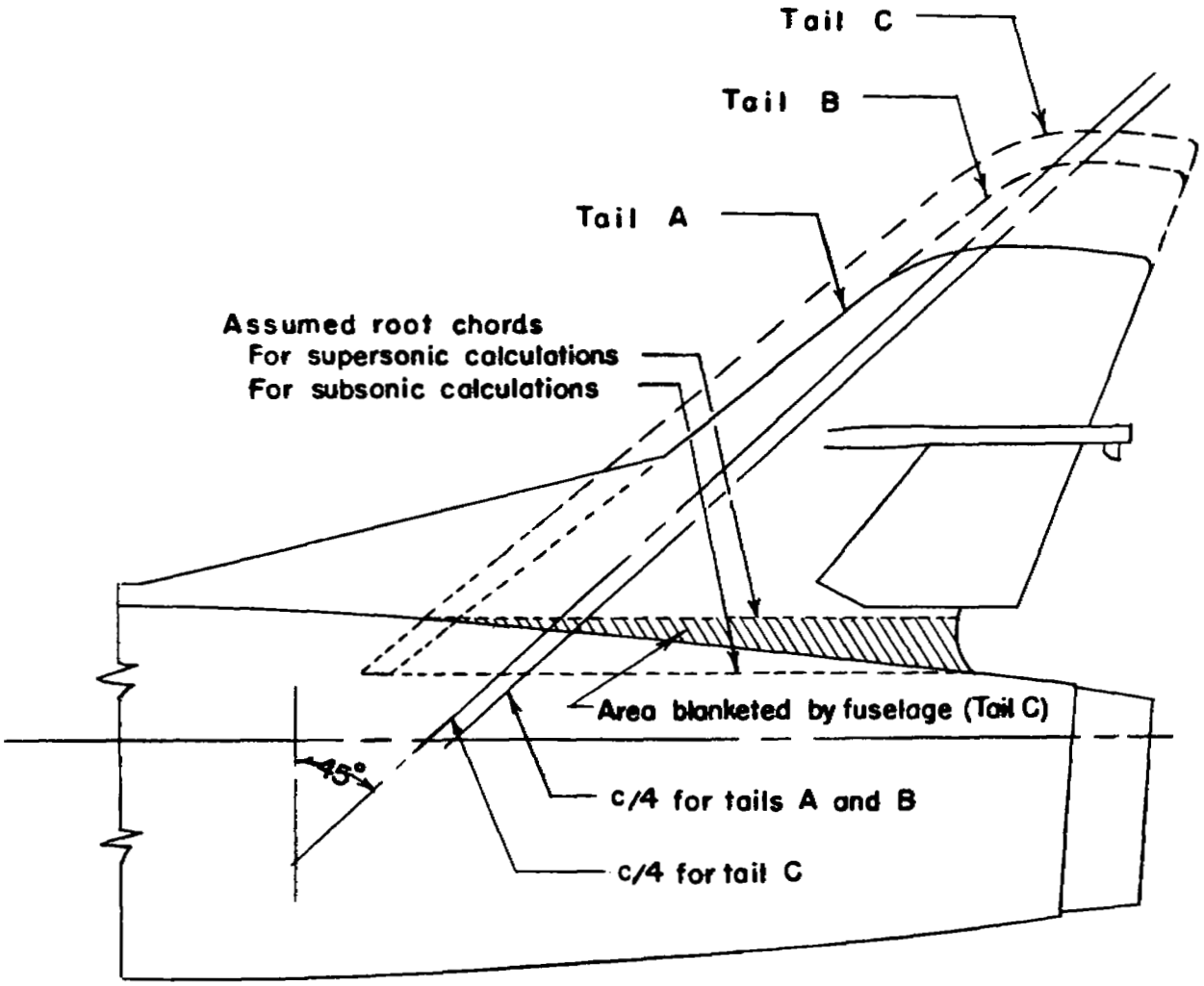

Figure 4.- Sketch of vertical tails A, B, and C. Refer to table I for physical characteristics of the vertical tail.

[redacted]

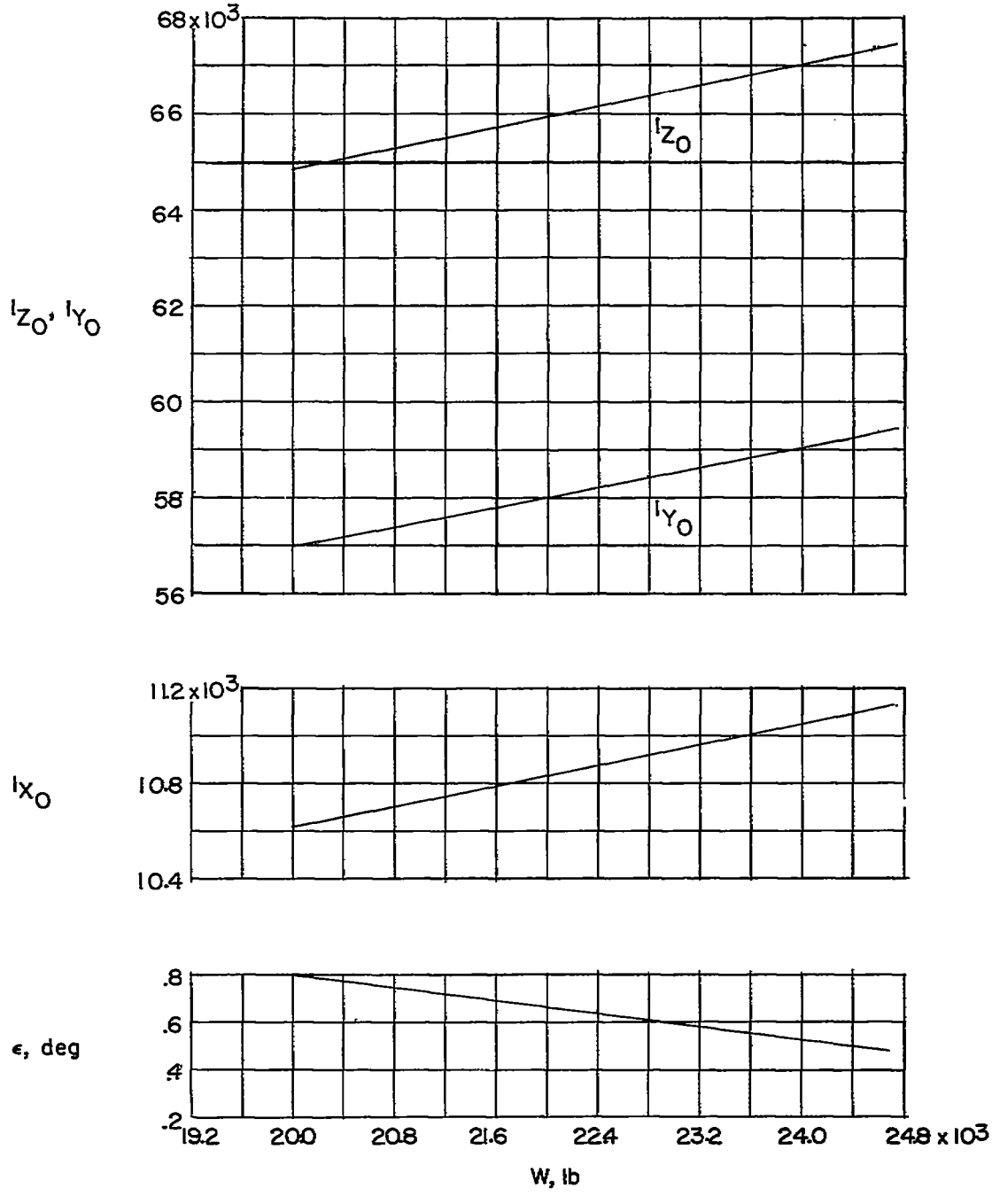

Figure 5.- Approximated variation of principal moments of inertia and inclination of principal axis relative to the body axis. Clean configuration.

[redacted]

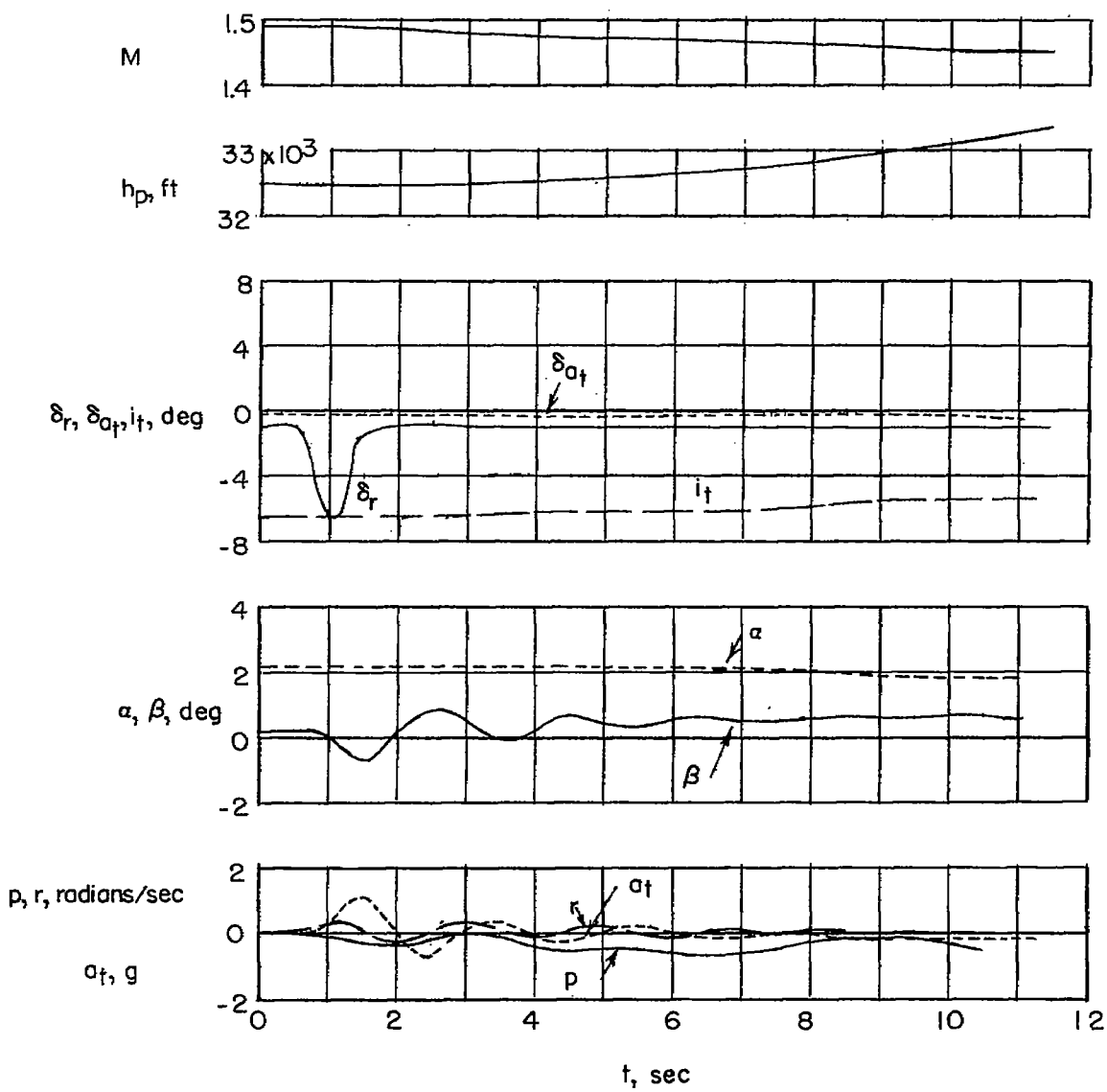

(a) Configuration C. $M \approx 1.45$; $h_p \approx 32{,}500$ feet.

Figure 6.- Time histories of lateral oscillations induced by a rudder pulse.

[redacted]

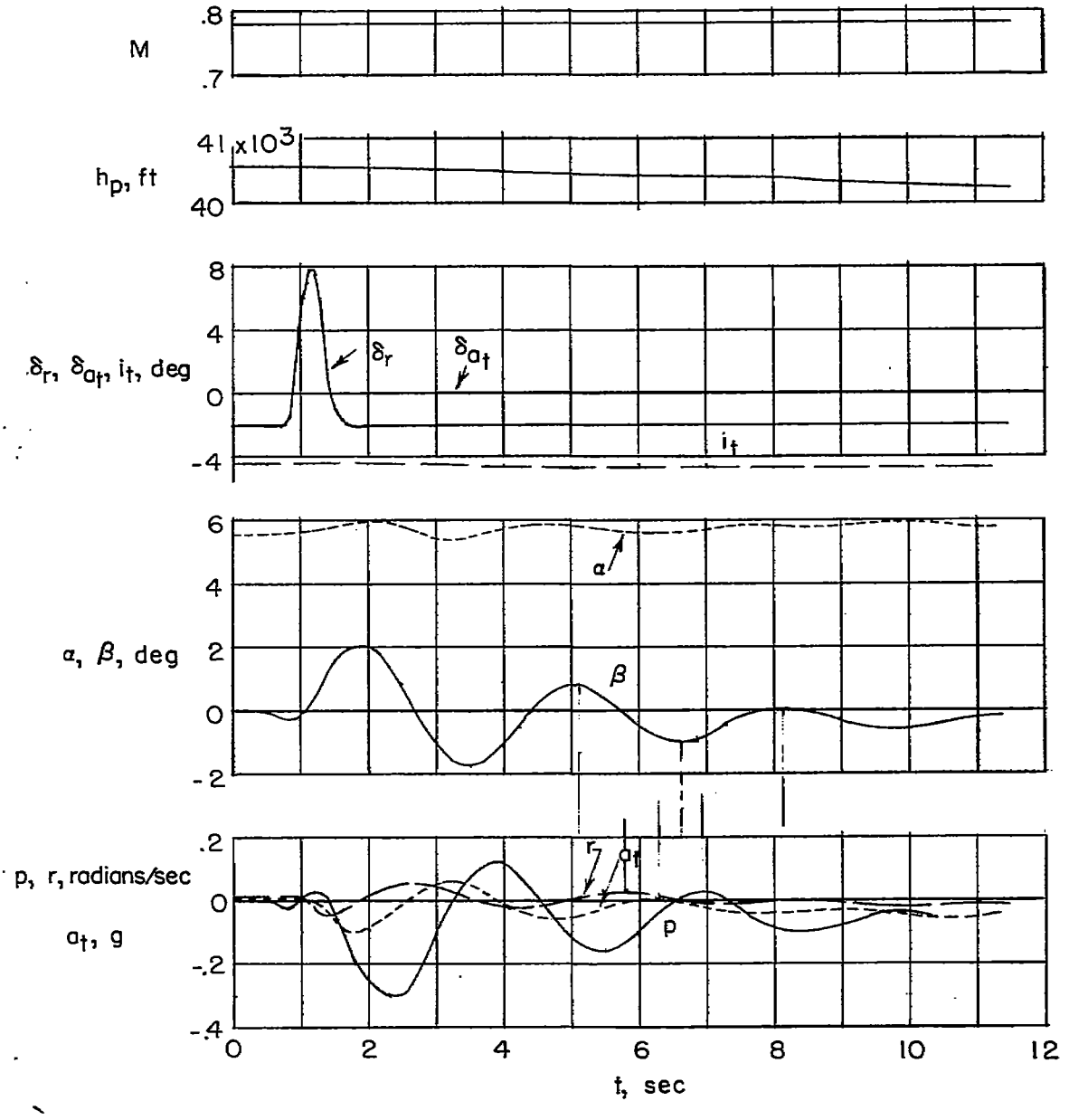

(b) Configuration D. $M \approx 0.78$; $h_p \approx 40{,}400$ feet.

Figure 6.- Concluded.

Film scale factors per inch

$p \approx 4.19$ radians/sec
$r \approx 0.543$ radians/sec
$\beta \approx 10.75$ deg
$a_t \approx 2.30$ g

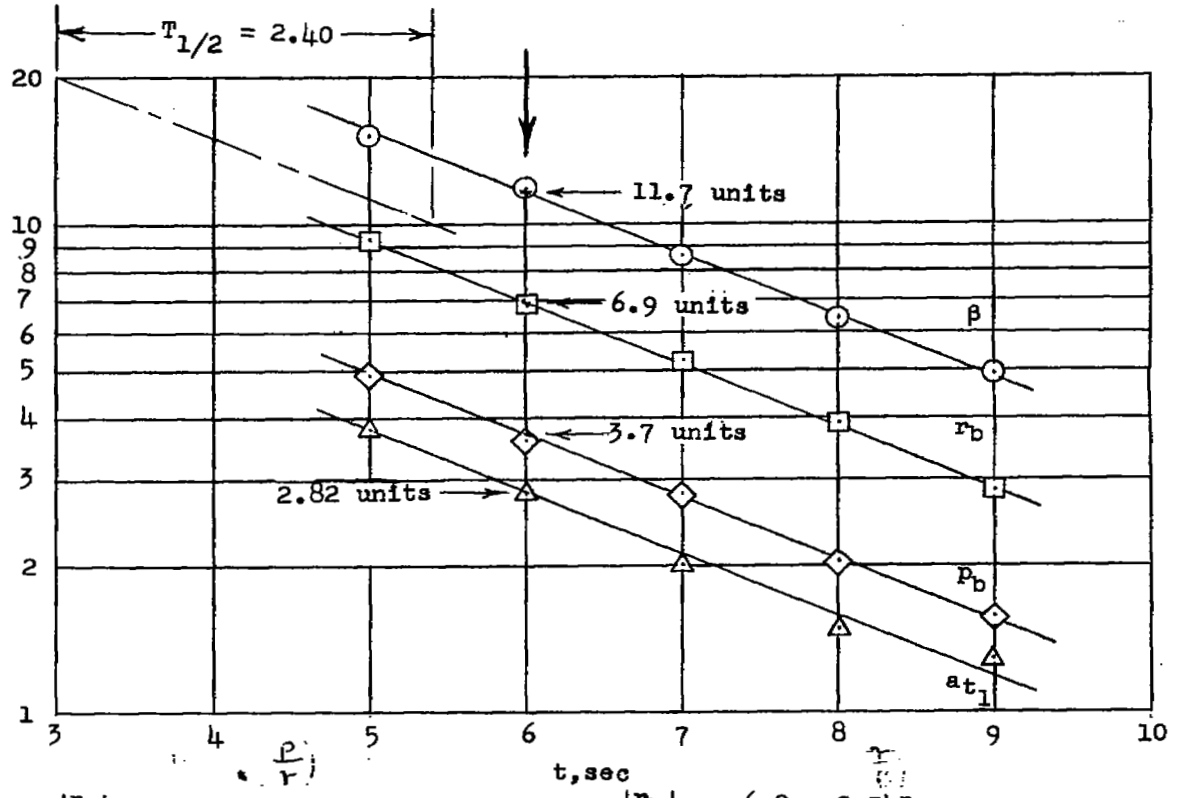

$$\frac{|p_b|}{|r_b|} = \frac{3.7}{6.9} \times \frac{4.19}{0.543} = 4.14 \qquad \frac{|r_b|}{|\beta_1|} = \frac{6.9}{11.7} \times \frac{0.543}{10.75} \times 57.3 = 1.71$$

$$\frac{|p_b|}{|r_b|} = \frac{3.7}{11.7} \times \frac{4.19}{10.75} \times 57.3 = 7.08 \qquad \frac{|a_{t_1}|}{|\beta_1|} = \frac{2.82}{11.7} \times \frac{2.30}{10.75} \times 57.3 = 2.95$$

Figure 7.- Typical use of the semilogarithmic sheets for determining $T_{1/2}$ and amplitude ratios. h_p = 30,280 feet; M = 0.775; P = 2.98 sec; $T_{1/2}$ = 2.40 sec.

[redacted]

$$\frac{|\beta|}{|\beta_1|} = 1 - \frac{X_\beta}{V} \times \frac{|r_b|}{|\beta_1|} + \frac{Z_\beta}{V} \frac{|p_b|}{|\beta_1|}$$

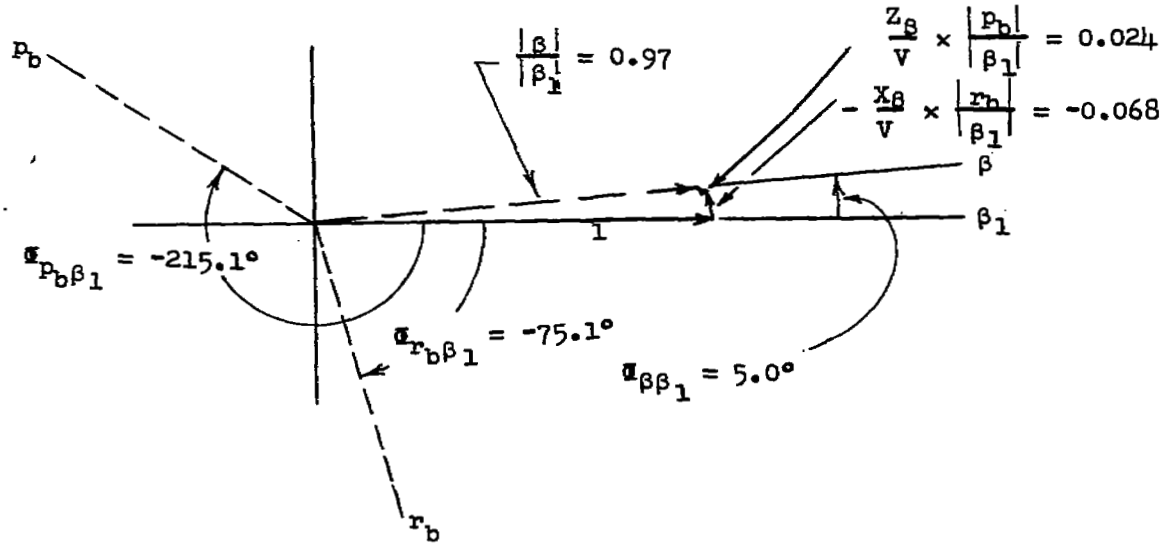

Corrected phase angles

$$\Phi_{p_b\beta} = \Phi_{p_b\beta_1} - \Phi_{\beta\beta_1} = -215.1 - 5.0 = -220.1°$$

$$\Phi_{r_b\beta} = \Phi_{r_b\beta_1} - \Phi_{\beta\beta_1} = -75.1 - 5.0 = -80.1°$$

$$\Phi_{a_{t_1}\beta} = \Phi_{a_{t_1}\beta_1} - \Phi_{\beta\beta_1} = 203.9 - 5.0 = 198.9°$$

(a) Determination of phase lag and magnification factor of β-vane due to vane location.

Figure 8.- Typical sequence employed in the determination of lateral derivatives using flight data and the time-vector method.

[redacted]

$$\frac{|a_t|}{|\beta|} = \frac{|a_{t_1}|}{|\beta|} + \frac{Z_{a_t}}{g} \times \frac{|\dot{p}_b|}{|\beta|} - \frac{X_{a_t}}{g} \times \frac{|\dot{r}_b|}{|\beta|}$$

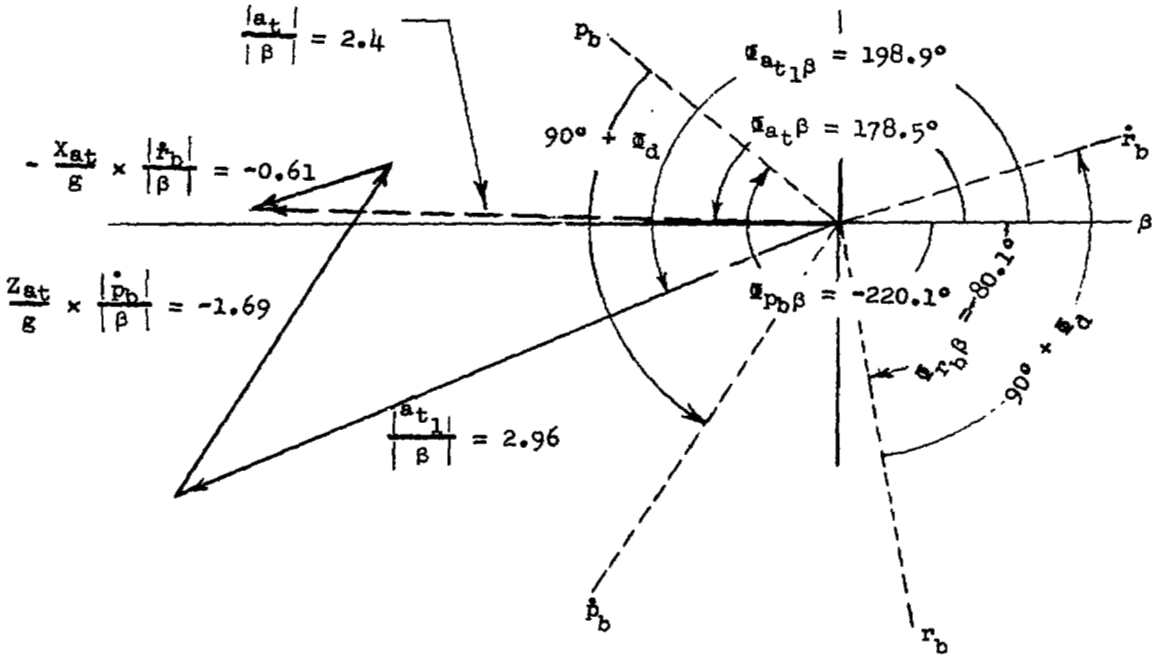

(b) Determination of correct value of $\frac{|a_t|}{|\beta|}$. Correction necessitated by lateral accelerometer location.

Figure 8.- Continued.

$C_{L_o} = \frac{W}{qS}$

$$-2\tau\frac{|\dot{\beta}|}{|\beta|} - 2\tau\frac{|r|}{|\beta|} + C_{L_o}\frac{|\varphi|}{|\beta|} + C_{L_o}\frac{|a_{t_2}|}{|\beta|} = 0$$

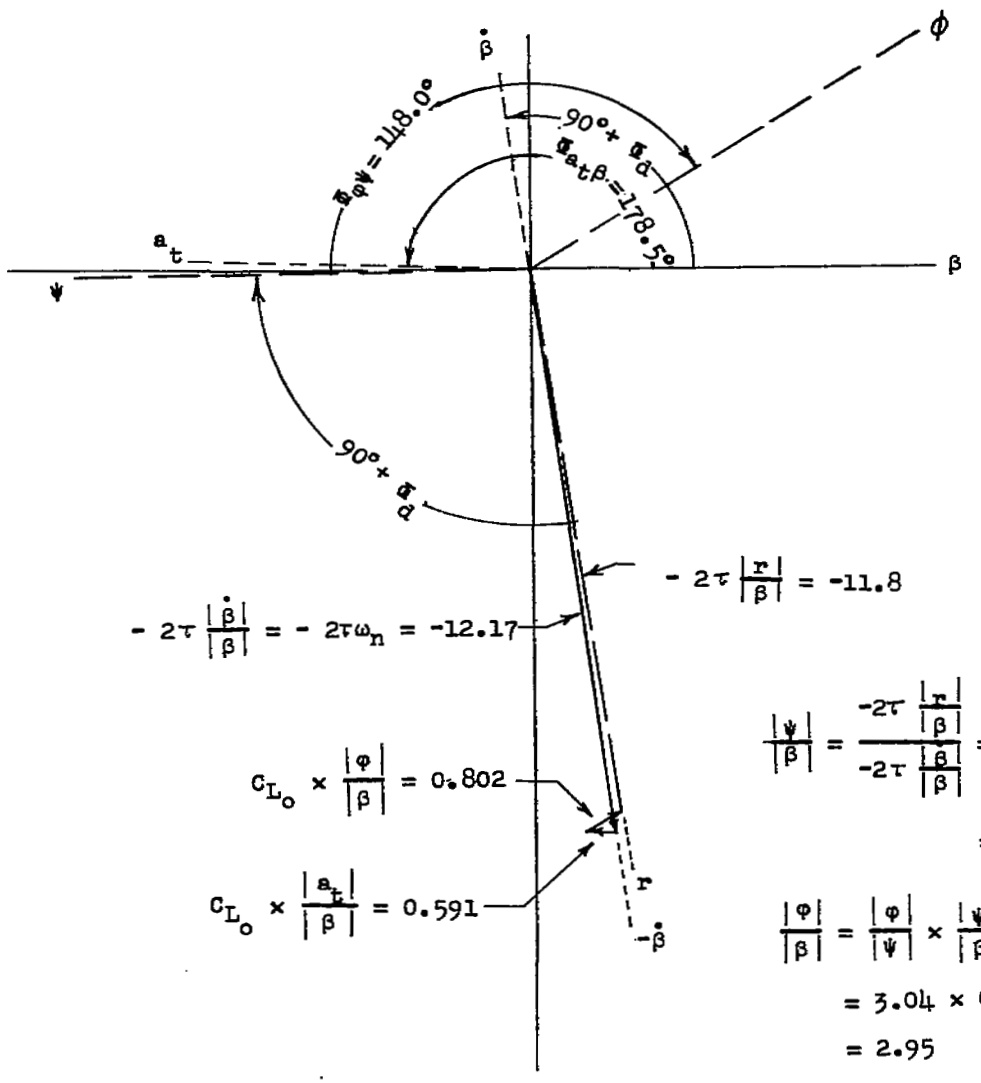

$$\frac{|\psi|}{|\beta|} = \frac{-2\tau\frac{|r|}{|\beta|}}{-2\tau\frac{|\dot{\beta}|}{|\beta|}} = \frac{-11.8}{-12.17}$$

$$= 0.97$$

$$\frac{|\varphi|}{|\beta|} = \frac{|\varphi|}{|\psi|} \times \frac{|\psi|}{|\beta|}$$

$$= 3.04 \times 0.97$$

$$= 2.95$$

$\Phi_{p\beta} = -322.5°$; $\Phi_{r\beta} = -81.5°$; $\Phi_{\psi\beta} = -179.0°$

(c) Determination of $\frac{|\psi|}{|\beta|}$, $\frac{|\varphi|}{|\beta|}$, and positions of the r, ψ, and φ vectors relative to β.

Figure 8.- Continued.

$$C_{L_o} \frac{\left|a_t\right|}{\left|\beta\right|} - C_{Y_p} \frac{\left|p'\right|}{\left|\beta\right|} - \left(C_{Y_r} - C_{Y_{\dot{\beta}}}\right) \frac{\left|r'\right|}{\left|\beta\right|} - C_{Y_\beta} = 0$$

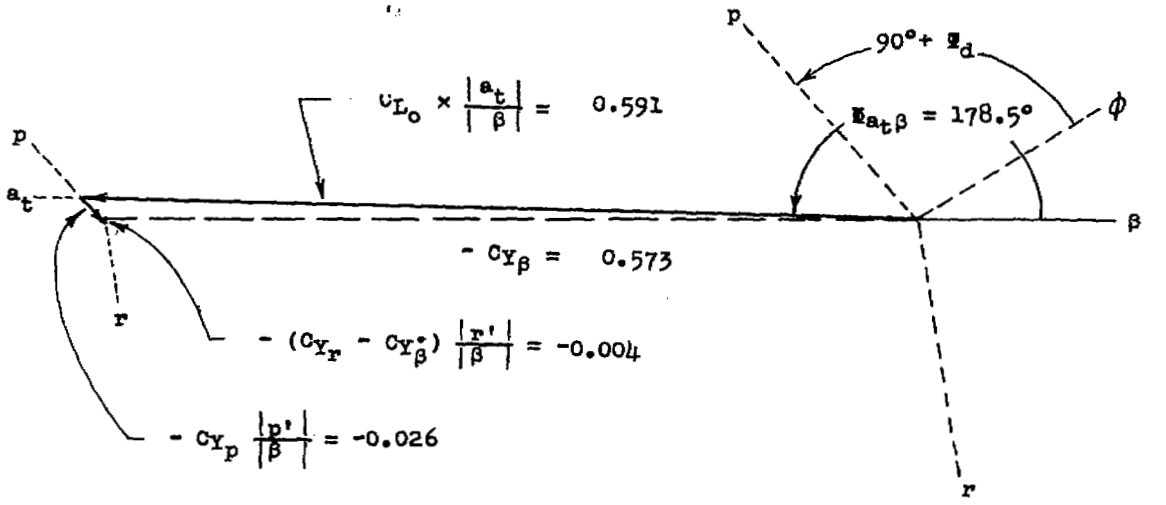

$$C_{Y_\beta} = -0.573$$

$$C_{Y_r} - C_{Y_{\dot{\beta}}} = \frac{\left(C_{Y_r} - C_{Y_{\dot{\beta}}}\right) \frac{\left|r'\right|}{\left|\beta\right|}}{\frac{\left|r'\right|}{\left|\beta\right|}} = \frac{0.004}{0.0498} = 0.080$$

(d) Determination of C_{Y_β} and $\left(C_{Y_r} - C_{Y_{\dot{\beta}}}\right)$.

Figure 8.- Continued.

$$\frac{I_Z}{qSb} \times \frac{|\dot{r}|}{|\beta|} - \frac{I_{XZ}}{qSb} \times \frac{|\dot{p}|}{|\beta|} - C_{n_p} \frac{|p'|}{|\beta|} - (C_{n_r} - C_{n_{\dot{\beta}}}) \frac{|r'|}{|\beta|} - C_{n_\beta} = 0$$

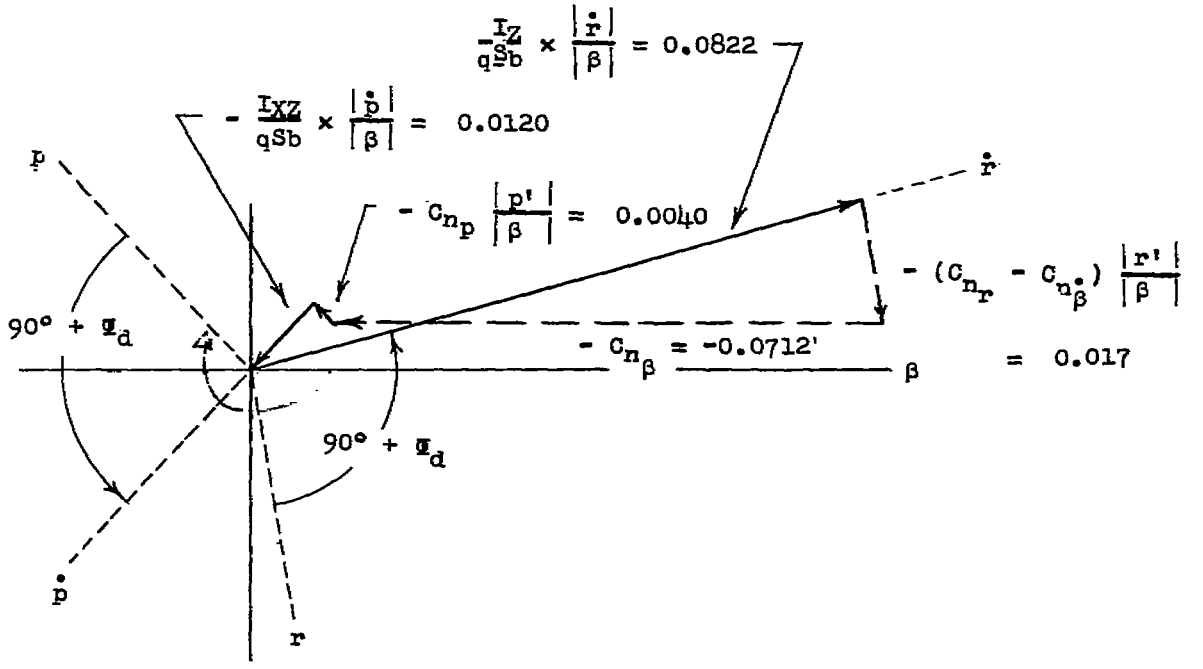

$$C_{n_\beta} = 0.0712$$

$$C_{n_r} - C_{n_{\dot{\beta}}} = \frac{(C_{n_r} - C_{n_{\dot{\beta}}}) \frac{|r'|}{|\beta|}}{\frac{|r'|}{|\beta|}} = \frac{-0.017}{0.0498} = -0.341$$

(e) Determination of C_{n_β} and $\left(C_{n_r} - C_{n_{\dot{\beta}}}\right)$.

Figure 8.- Continued.

$$\frac{I_X}{qSb} \times \frac{|\dot{p}|}{|\beta|} - \frac{I_{XZ}}{qSb} \times \frac{|\dot{r}|}{|\beta|} - C_{l_r} \times \frac{|r'|}{|\beta|} - C_{l_\beta} - C_{l_p} \times \frac{|p'|}{|\beta|} = 0$$

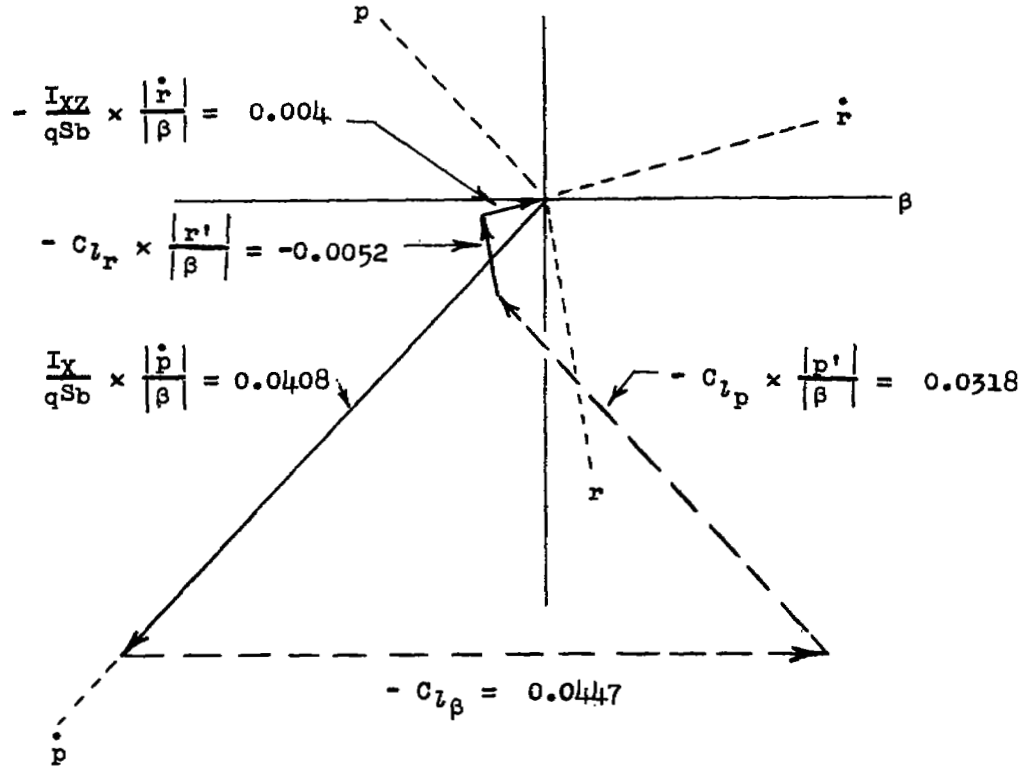

$$C_{l_\beta} = -0.0447$$

$$C_{l_p} = \frac{C_{l_p} \times \frac{|p'|}{|\beta|}}{\frac{|p'|}{|\beta|}} = \frac{-0.0318}{0.151} = -0.211$$

(f) Determination of C_{l_β} and C_{l_p}.

Figure 8.- Concluded.

[redacted]

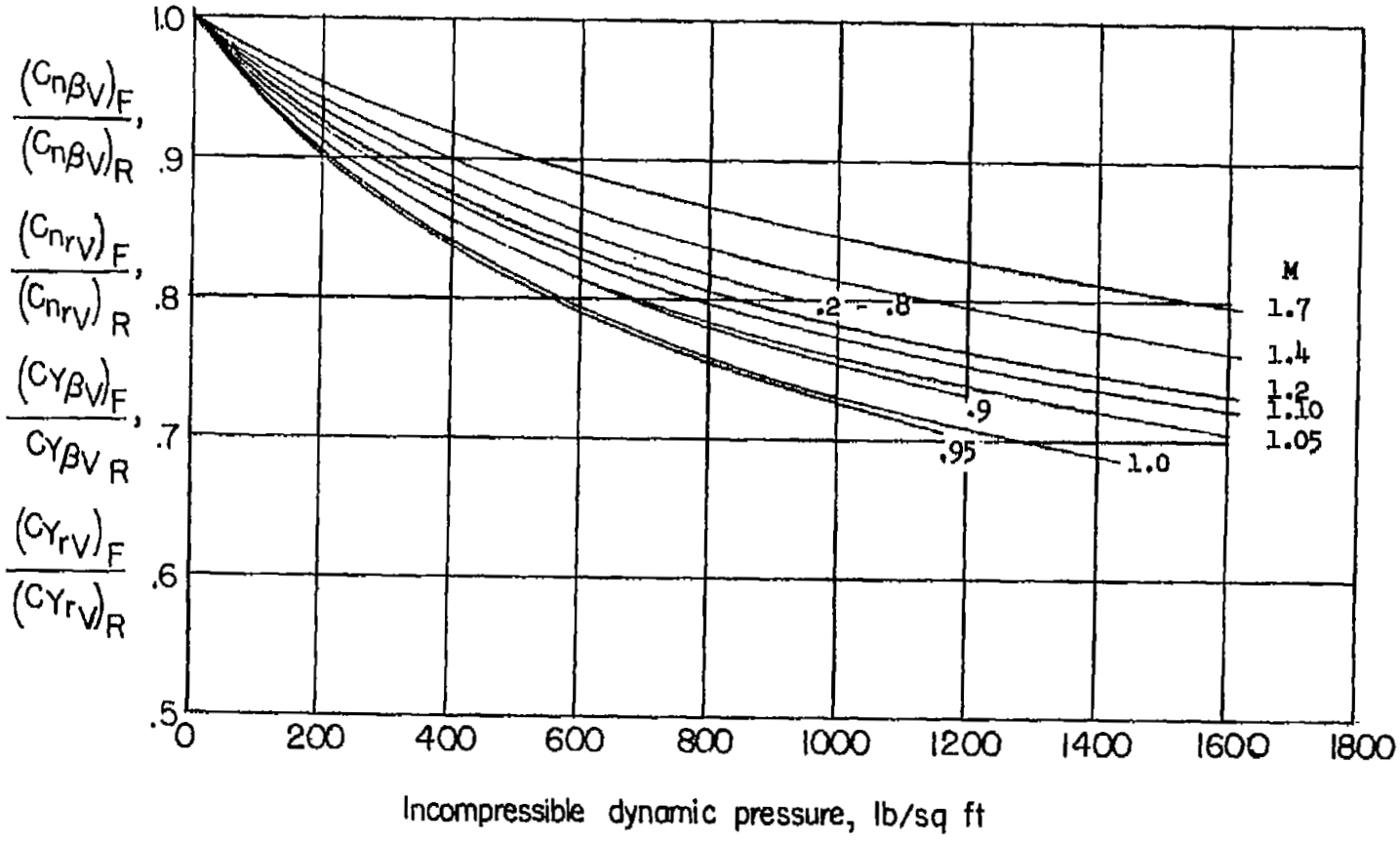

Figure 9.- Effect of flexibility of vertical tail C on vertical tail contributions to C_{n_β}, C_{n_r}, C_{Y_β}, and C_{Y_r}. $\delta_r = 0^\circ$; $\alpha = 0^\circ$; $\beta = -\psi$. (Manufacturer's estimate.)

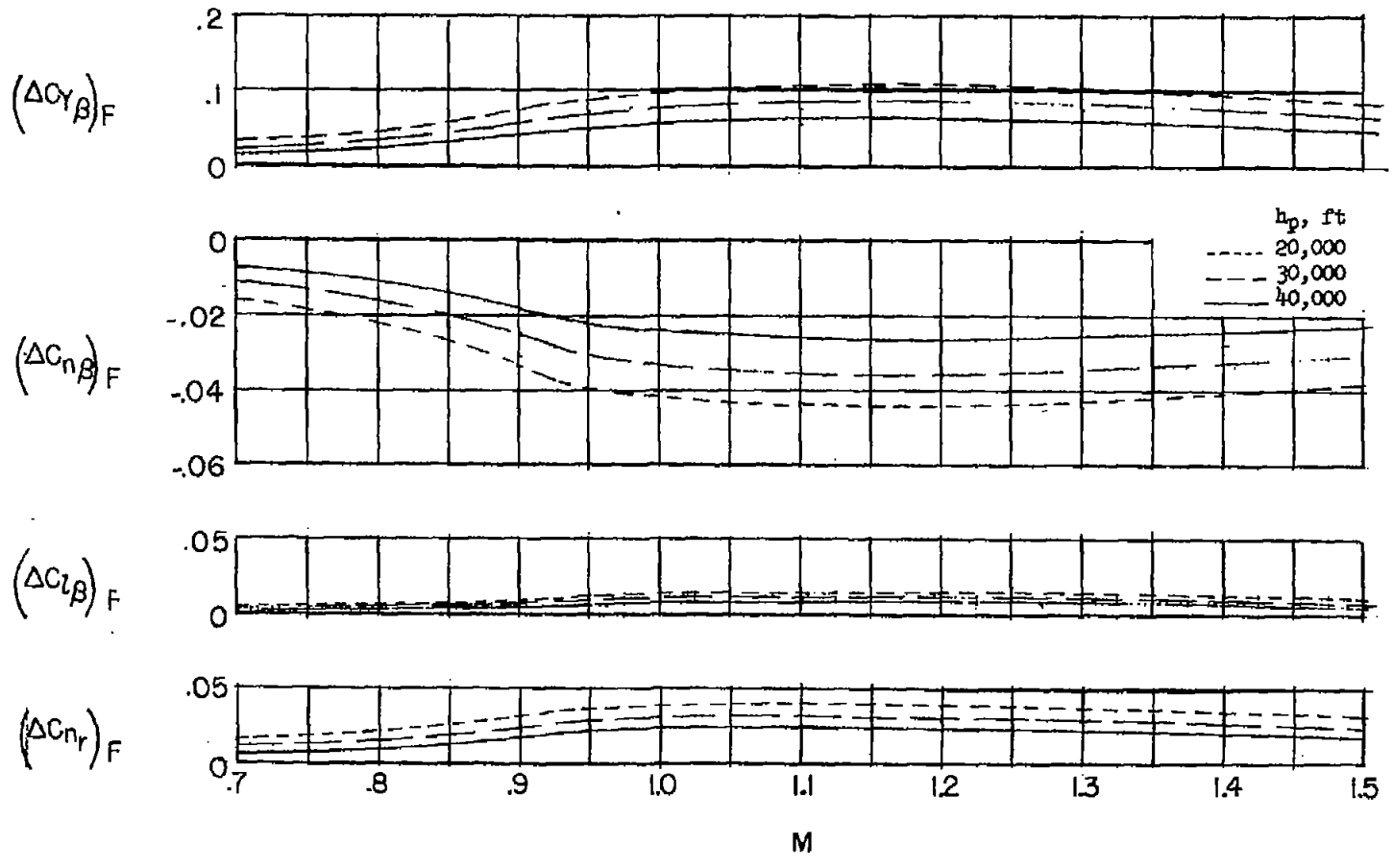

Figure 10.- Change in lateral stability derivatives due to torsional flexibility of the vertical stabilizer in configurations C and D. Estimates based on calculated derivatives.

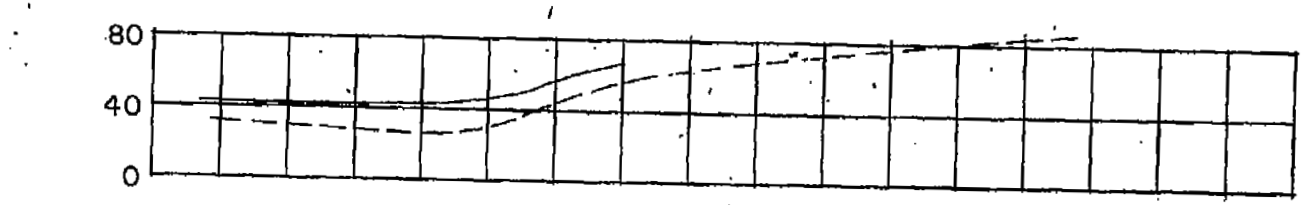

(a) h_p = 40,000 feet.

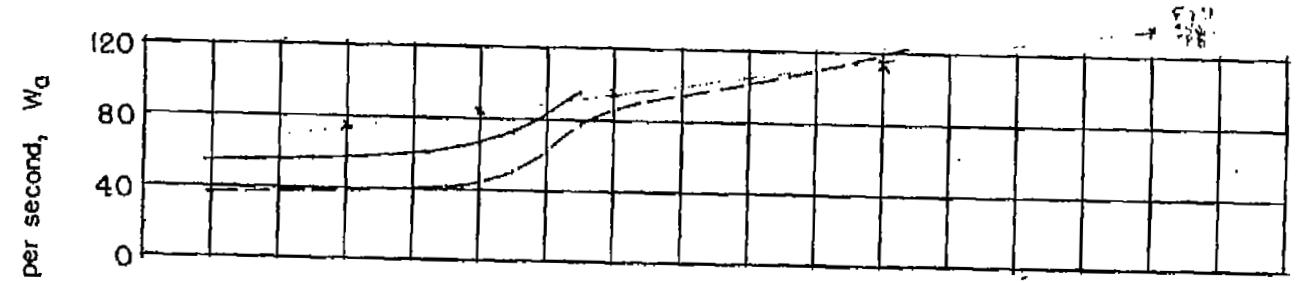

(b) h_p = 30,000 feet.

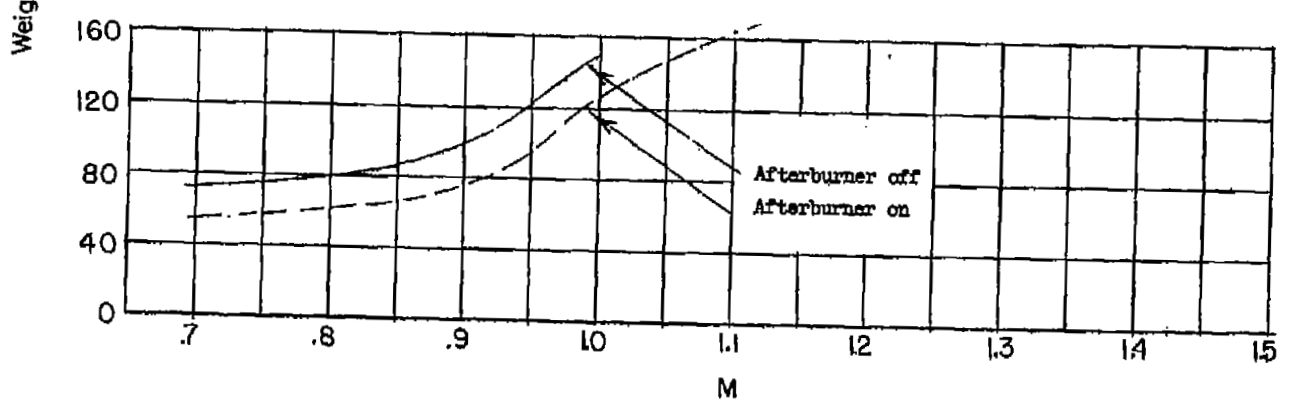

(c) h_p = 20,000 feet.

Figure 11.- Estimated weight rate of air to jet engine to maintain cruising speed.

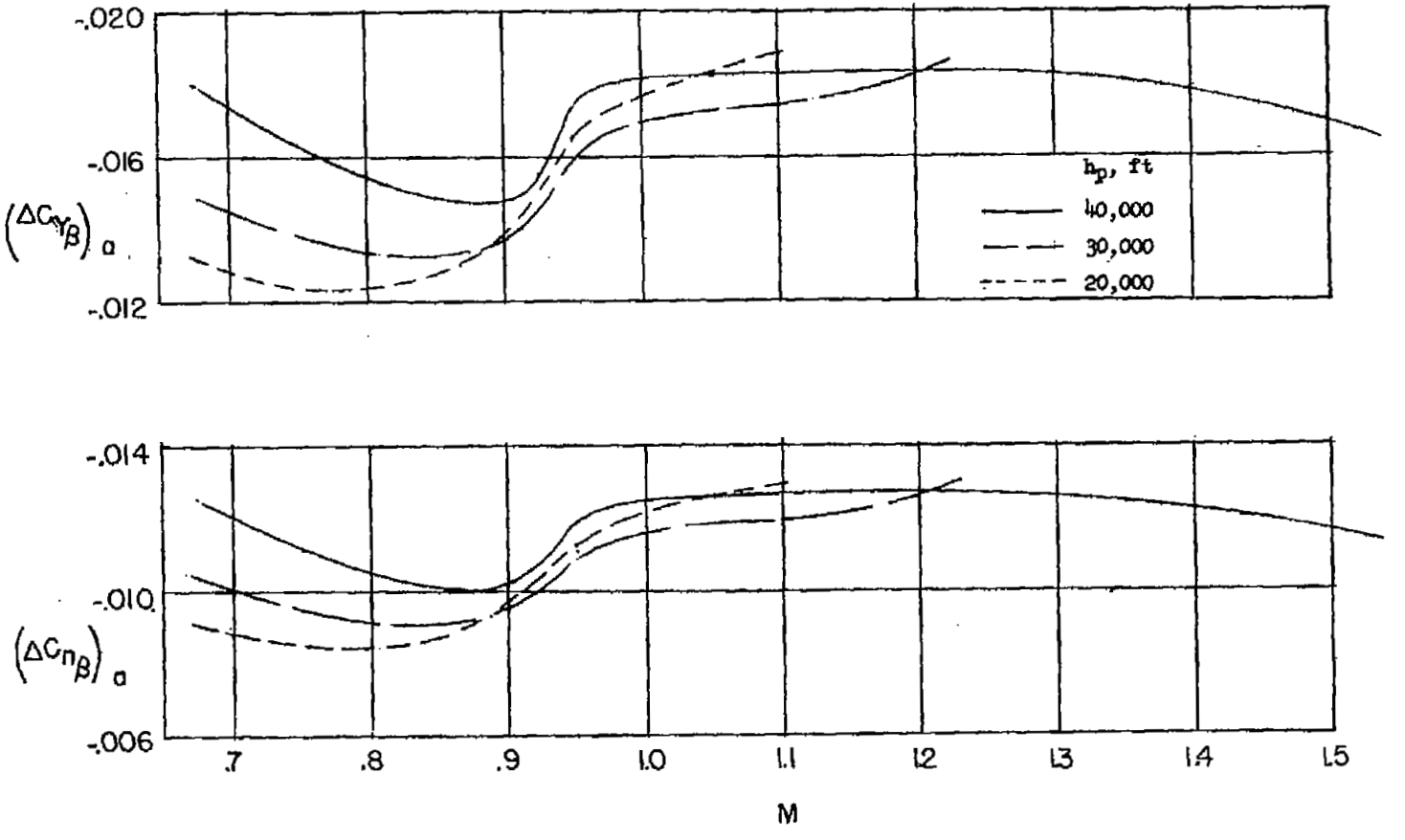

Figure 12.- Estimated contribution of the intake air of the jet engine to C_{Y_β} and C_{n_β}.

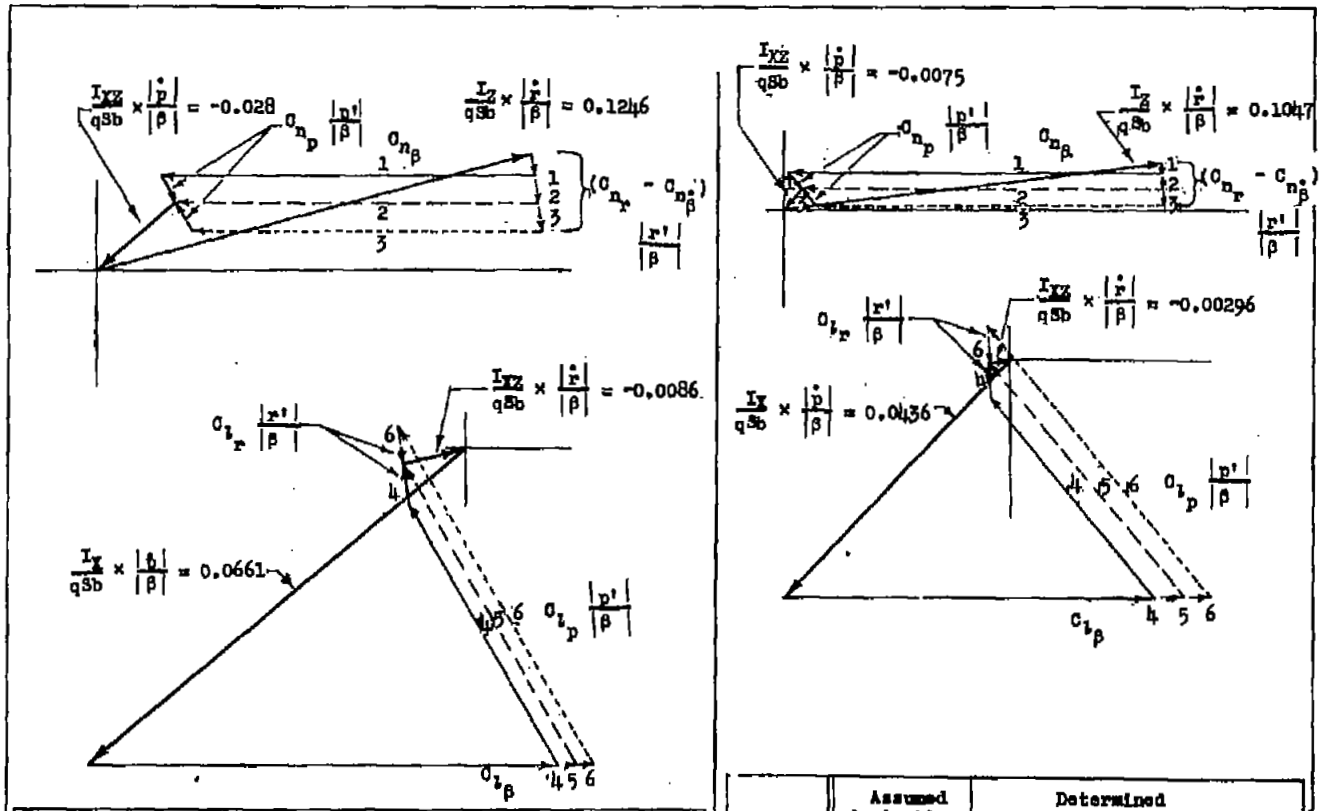

Condition	Assumed derivatives		Determined derivatives			
	C_{n_p}	C_{l_r}	C_{n_β}	$(C_{n_r}-C_{n_{\dot{\beta}}})$	C_{l_β}	C_{l_p}
1	0.05		0.1030	-0.109		
2	0.00		0.1002	-0.255		
3	-0.05		0.0970	-0.399		
4		0.10			-0.065	-0.240
5		0.00			-0.068	-0.277
6		-0.10			-0.070	-0.315

(a) M = 0.80.

Condition	Assumed derivatives		Determined derivatives			
	C_{n_p}	C_{l_r}	C_{n_β}	$(C_{n_r}-C_{n_{\dot{\beta}}})$	C_{l_β}	C_{l_p}
1	0.05		0.1025	-0.059		
2	0.00		0.0996	-0.146		
3	-0.05		0.0954	-0.235		
4		0.10			-0.051	-0.293
5		0.00			-0.055	-0.345
6		-0.10			-0.058	-0.400

(b) M = 1.20.

Figure 13.- Influence of C_{n_p} and C_{l_r} on the lateral stability derivatives for configuration C at M = 0.80 and M = 1.20 at h_p = 40,000 feet. Solution based on data obtained from faired curves.

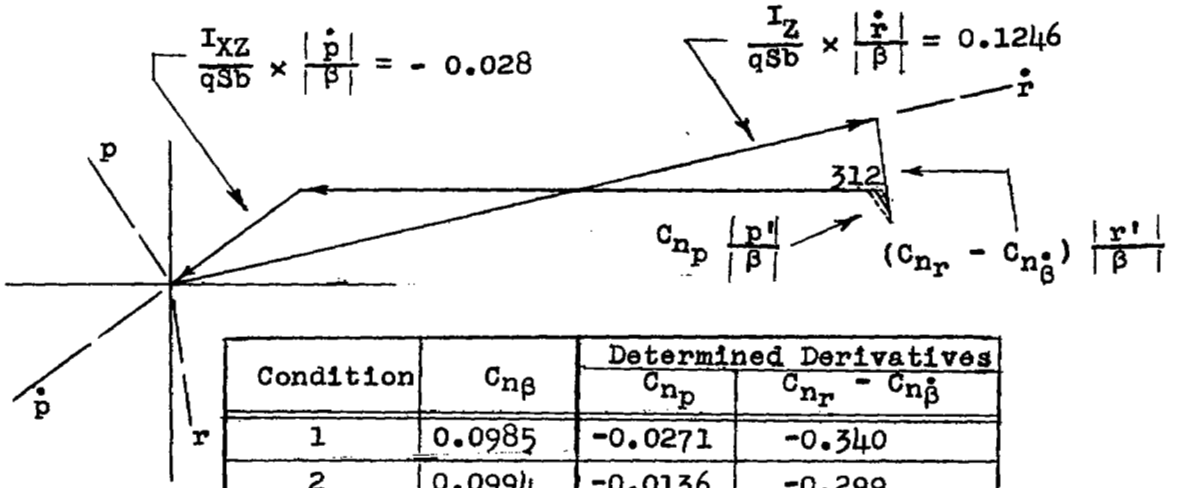

Condition	C_{n_β}	Determined Derivatives	
		C_{n_p}	$C_{n_r} - C_{n_{\dot{\beta}}}$
1	0.0985	-0.0271	-0.340
2	0.0994	-0.0136	-0.299
3	0.0974	-0.0432	-0.378

(a) M = 0.80.

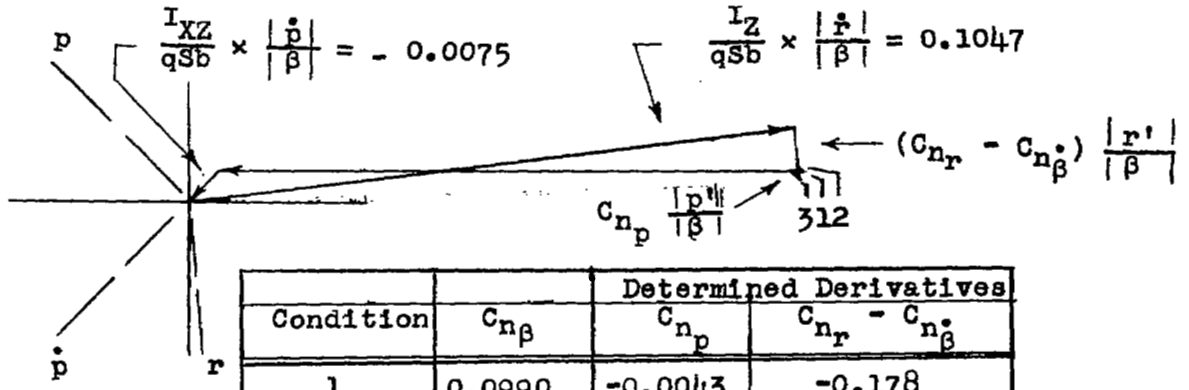

Condition	C_{n_β}	Determined Derivatives	
		C_{n_p}	$C_{n_r} - C_{n_{\dot{\beta}}}$
1	0.0990	-0.0043	-0.178
2	0.1001	0.0103	-0.148
3	0.0980	-0.0155	-0.196

(b) M = 1.20.

Figure 14.- Influence of ±1 percent change in C_{n_β} on the lateral stability derivatives C_{n_p} and $\left(C_{n_r} - C_{n_{\dot{\beta}}}\right)$ for configuration C at M = 0.80 and M = 1.20 at h_p = 40,000 feet. Basic values of C_{n_β} used were obtained from faired flight data, vector solutions of C_{l_β}, and equation (23).

[redacted]

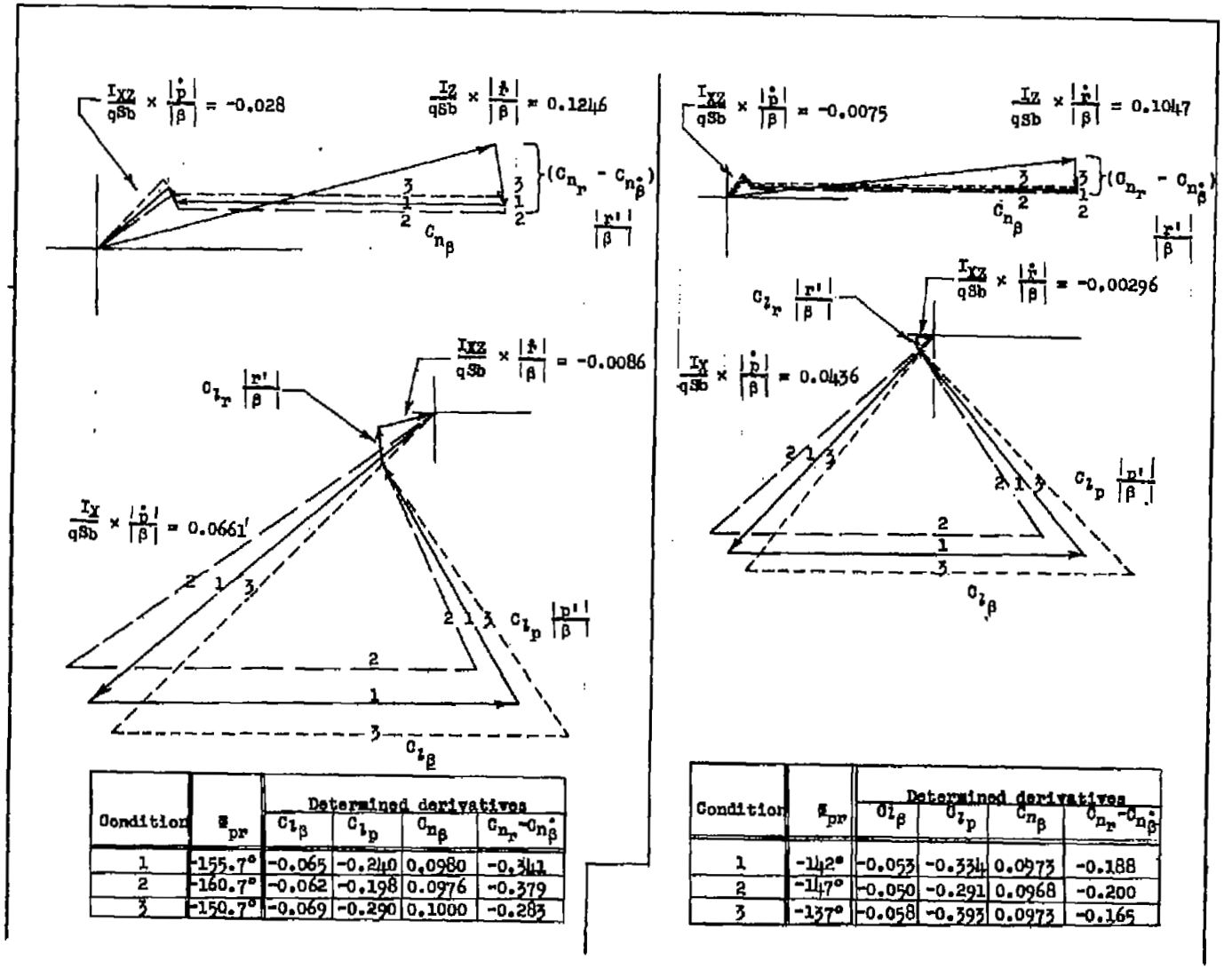

Condition	Φ_{pr}	Determined derivatives			
		C_{l_β}	C_{l_p}	C_{n_β}	$C_{n_r} - C_{n_{\dot{\beta}}}$
1	-155.7°	-0.065	-0.240	0.0980	-0.341
2	-160.7°	-0.062	-0.198	0.0976	-0.379
3	-150.7°	-0.069	-0.290	0.1000	-0.283

(a) M = 0.80.

Condition	Φ_{pr}	Determined derivatives			
		C_{l_β}	C_{l_p}	C_{n_β}	$C_{n_r} - C_{n_{\dot{\beta}}}$
1	-142°	-0.053	-0.334	0.0973	-0.188
2	-147°	-0.050	-0.291	0.0968	-0.200
3	-137°	-0.058	-0.393	0.0973	-0.165

(b) M = 1.20.

Figure 15.- Influence of ±5° change in Φ_{pr} on the lateral stability derivatives for configuration C at M = 0.80 and M = 1.20 at h_p = 40,000 feet.

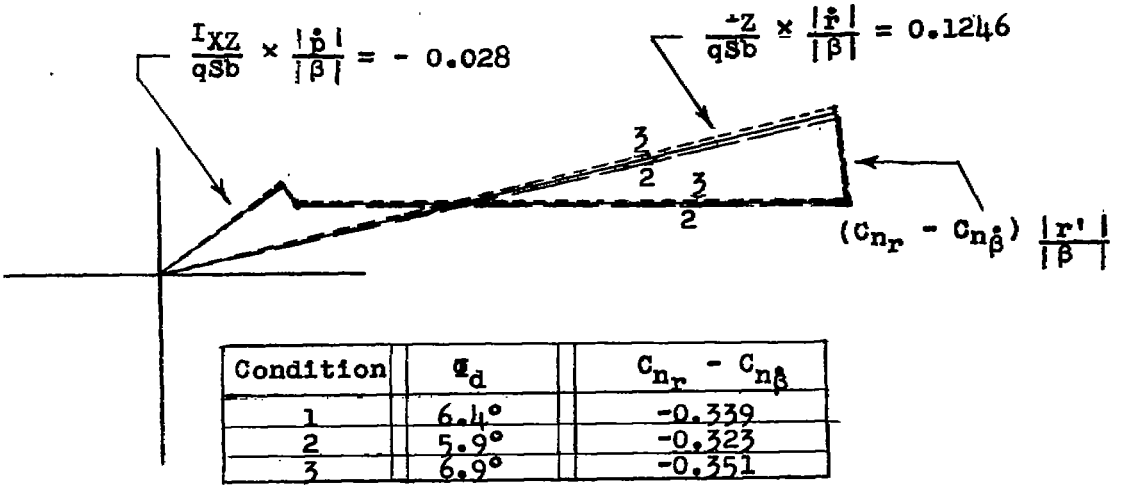

Condition	Φ_d	$C_{n_r} - C_{n_{\dot{\beta}}}$
1	6.4°	-0.339
2	5.9°	-0.323
3	6.9°	-0.351

(a) M = 0.80.

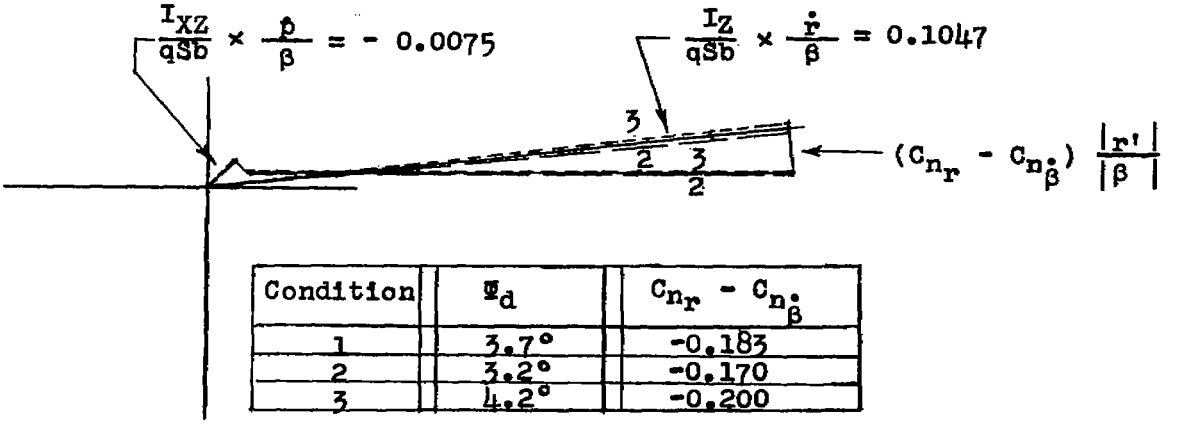

Condition	Φ_d	$C_{n_r} - C_{n_{\dot{\beta}}}$
1	3.7°	-0.183
2	3.2°	-0.170
3	4.2°	-0.200

(b) M = 1.20.

Figure 16.- Influence of $\pm 0.5°$ change in Φ_d on the lateral stability derivative $\left(C_{n_r} - C_{n_{\dot{\beta}}}\right)$ for configuration C at M = 0.80 and M = 1.20 at h_p = 40,000 feet.

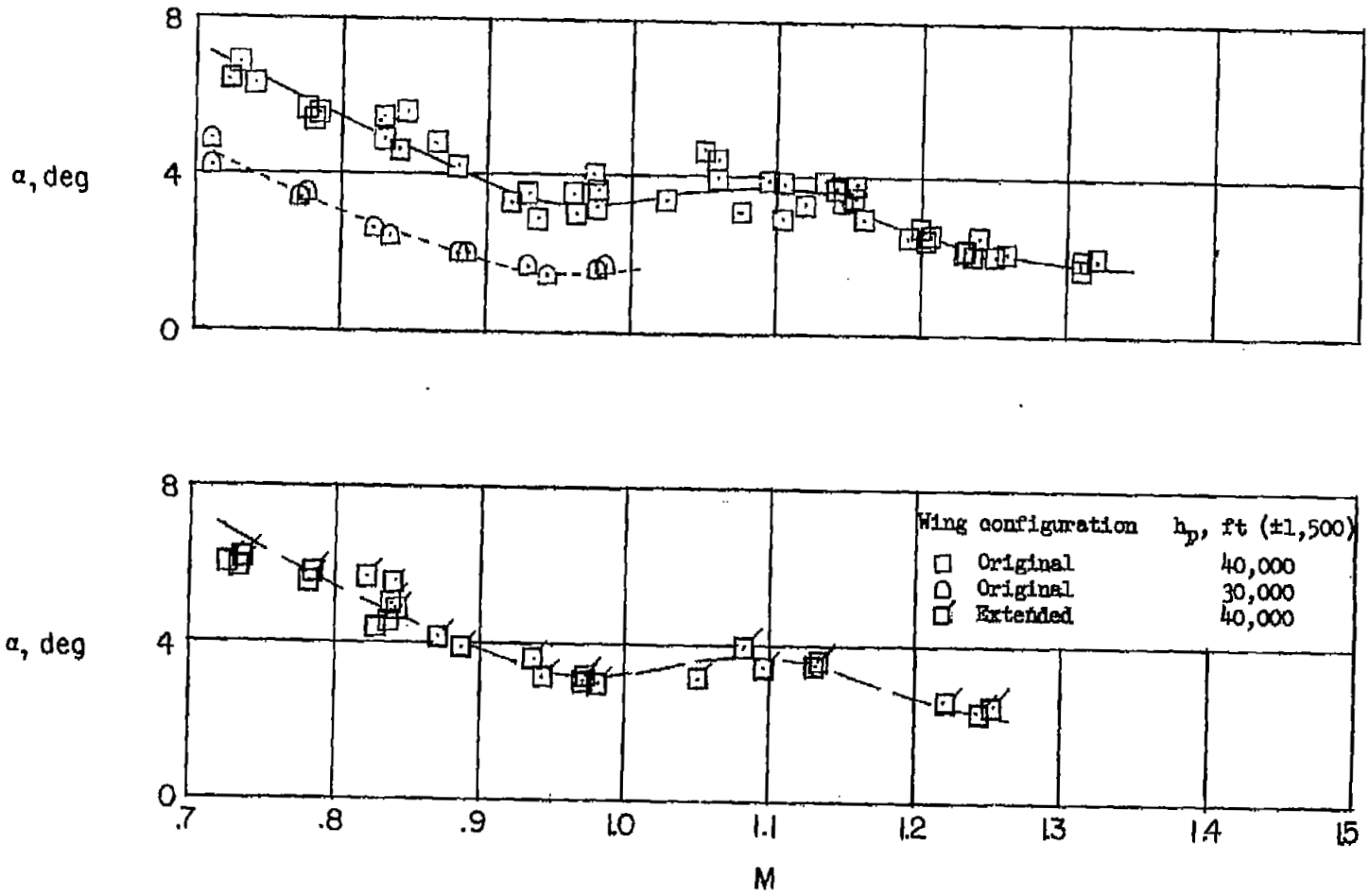

Figure 17.- Variation of trim angle of attack with Mach number.

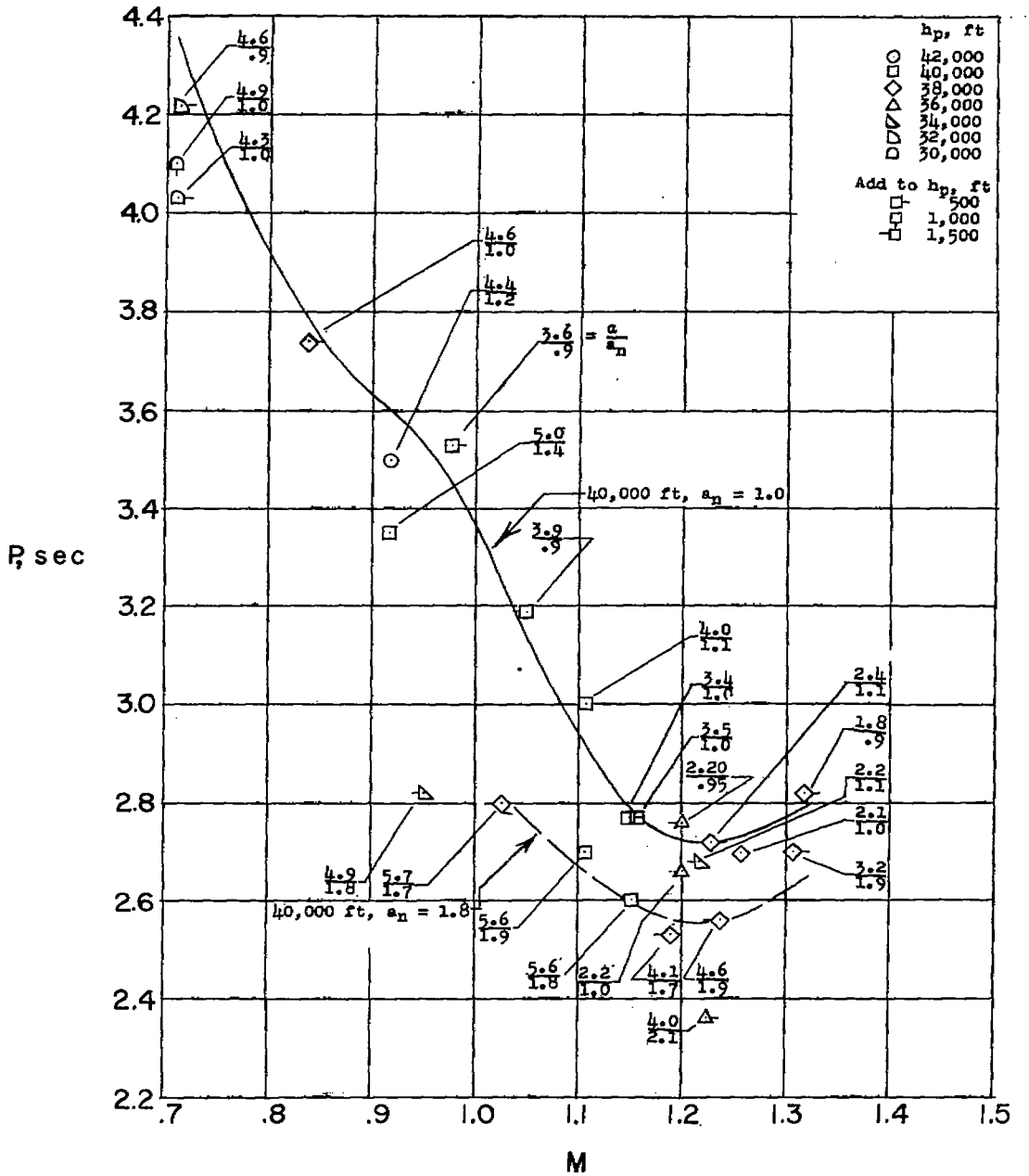

(a) Period characteristics.

Figure 18.- Period and damping characteristics of the airplane as functions of Mach number, altitude, and angle of attack per load factor. Configuration A.

[redacted]

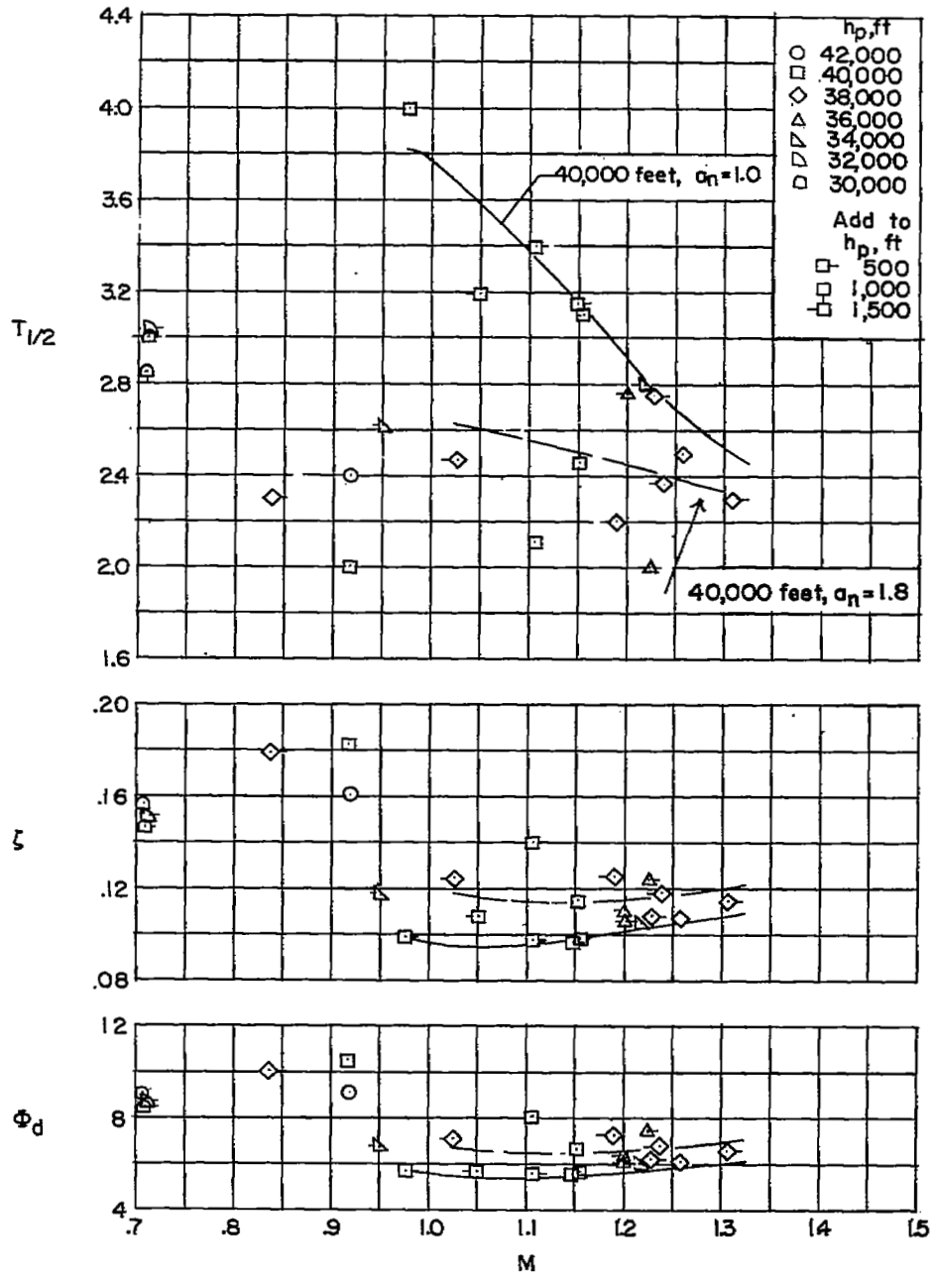

(b) Damping characteristics.

Figure 18.- Concluded.

[redacted]

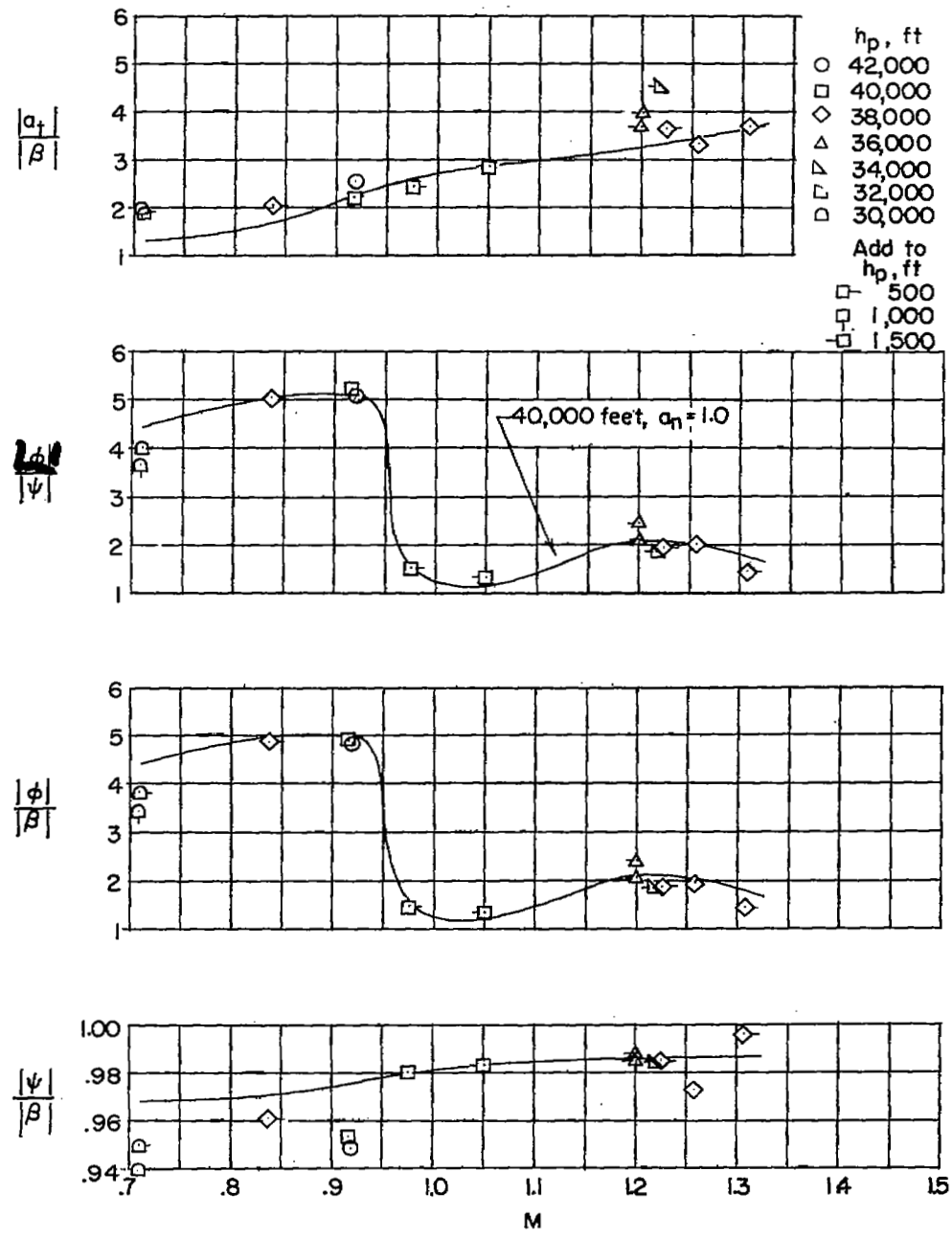

(a) Amplitude ratio characteristics.

Figure 19.- Amplitude ratio and phase angle characteristics of the airplane at its natural frequency as functions of Mach number and altitude. Configuration A.

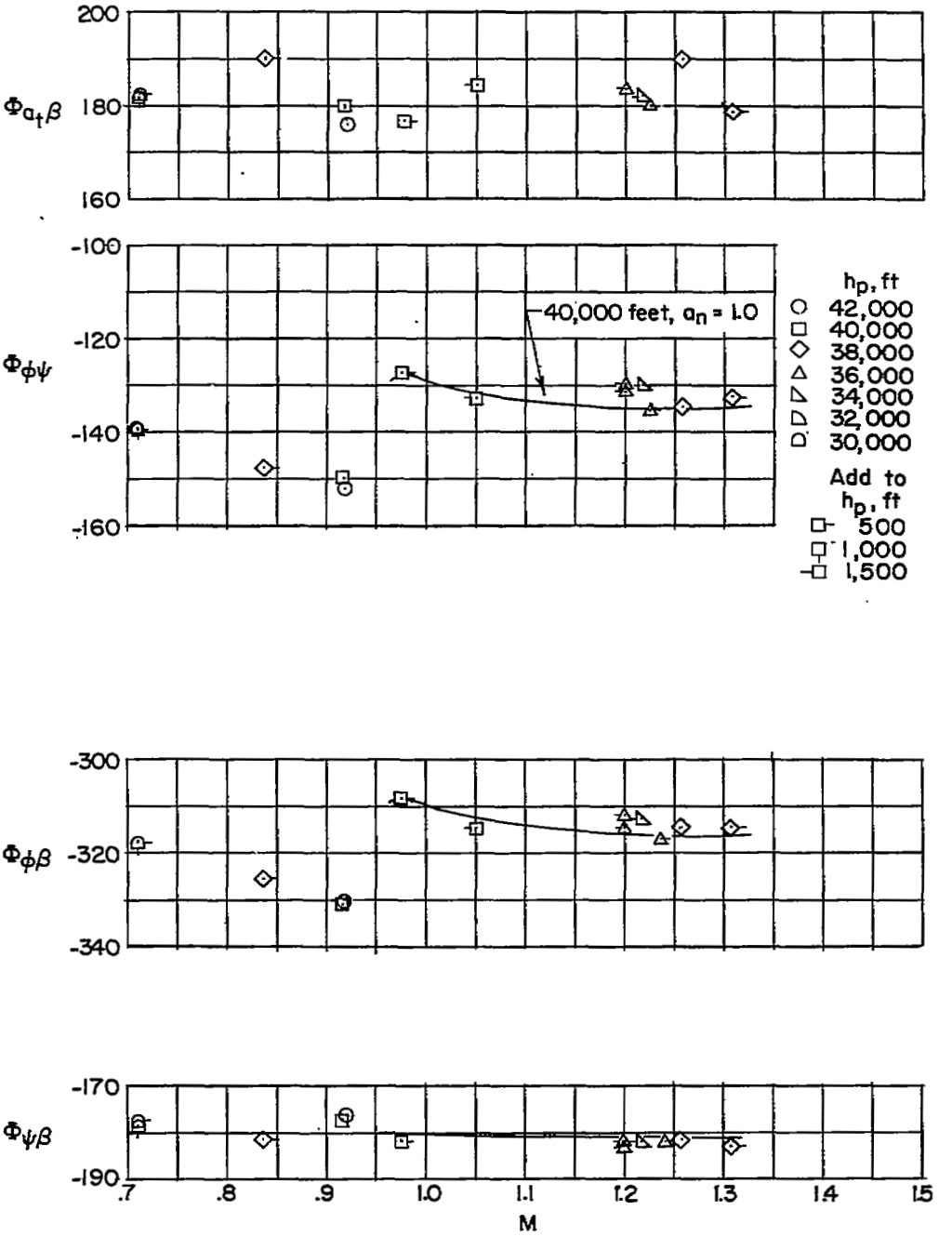

(b) Phase angle characteristics.

Figure 19.- Concluded.

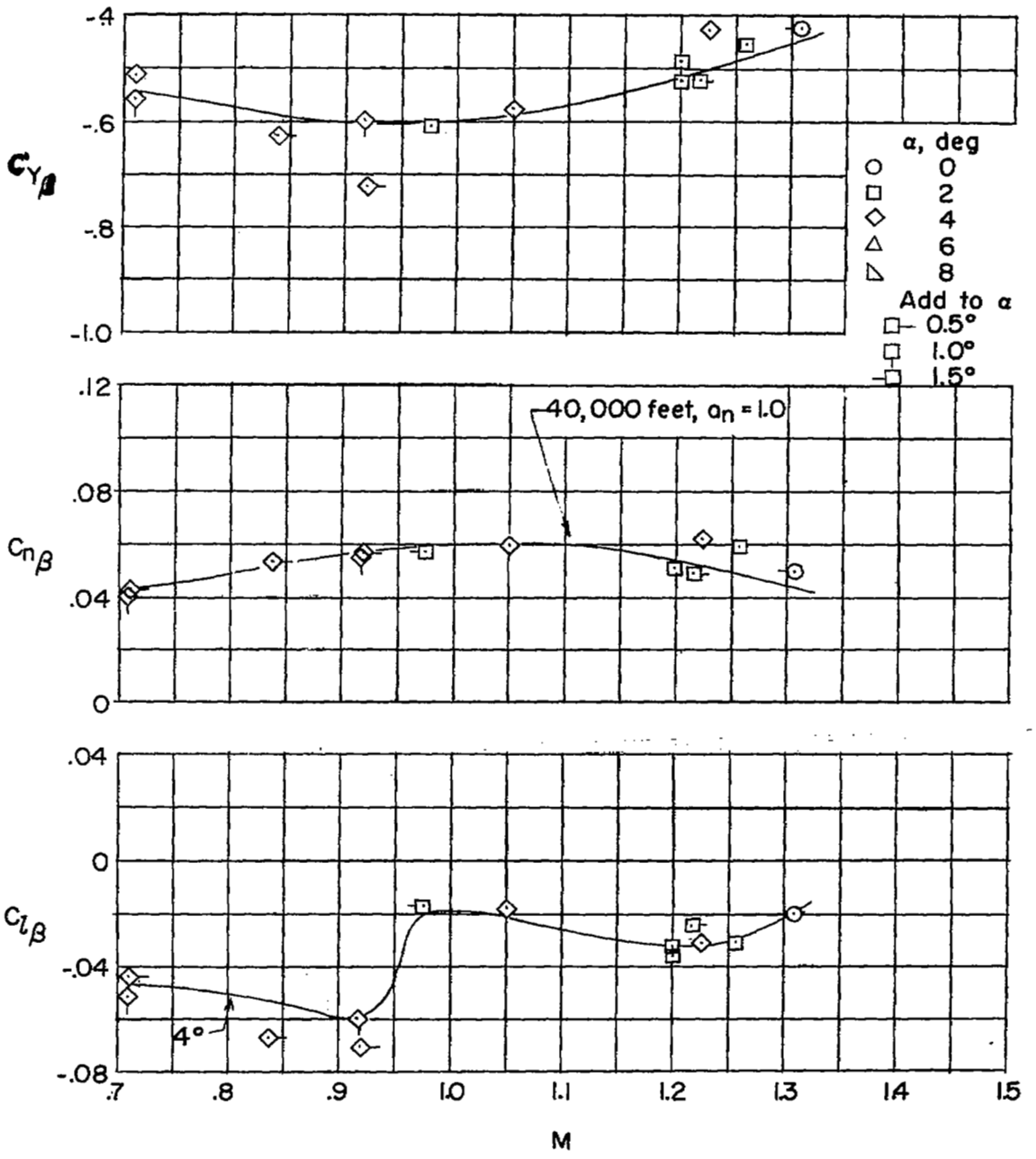

(a) Static derivatives.

Figure 20.- Variation of static and dynamic lateral stability derivatives with Mach number. Configuration A.

[redacted]

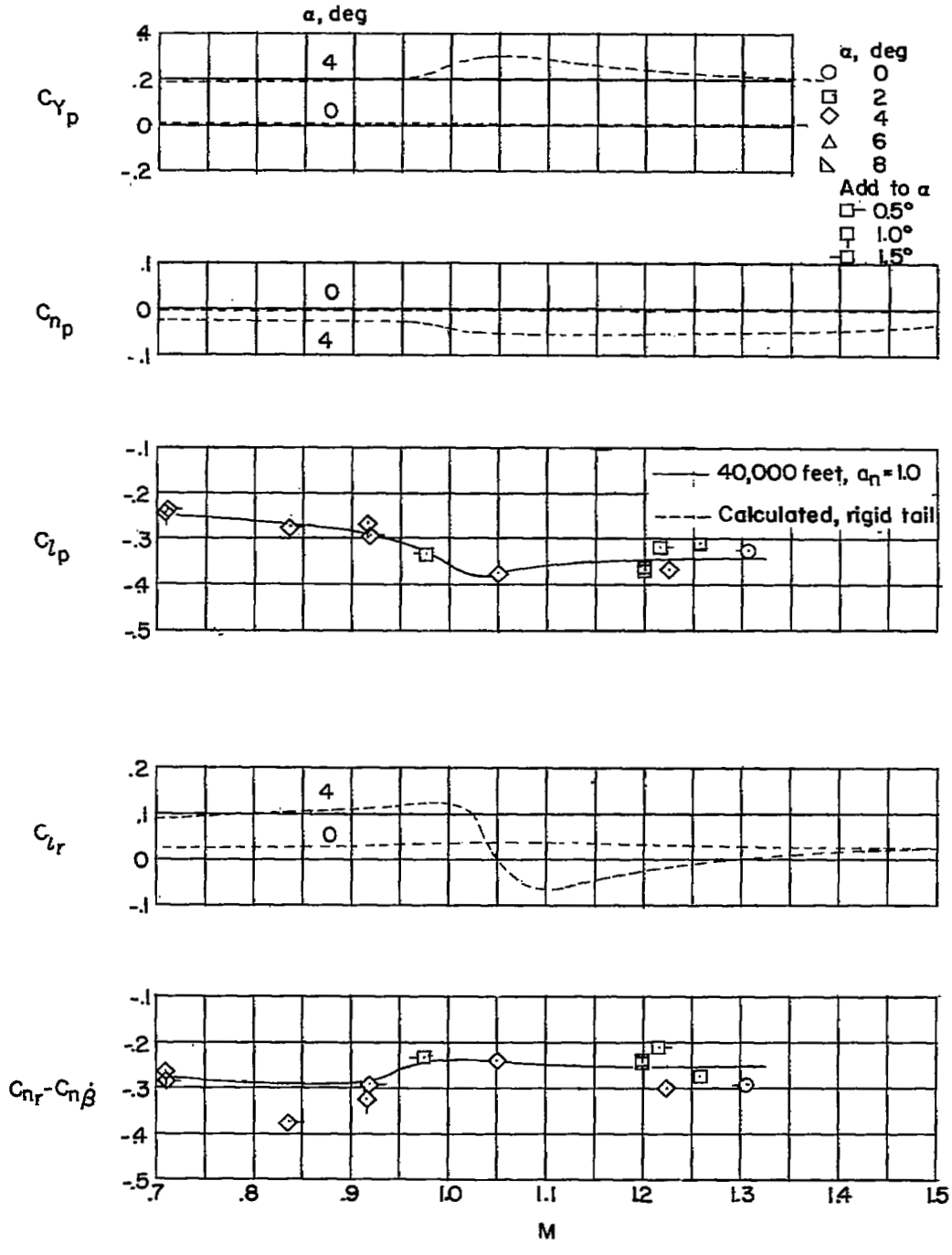

(b) Dynamic derivatives.

Figure 20.- Concluded.

[redacted]

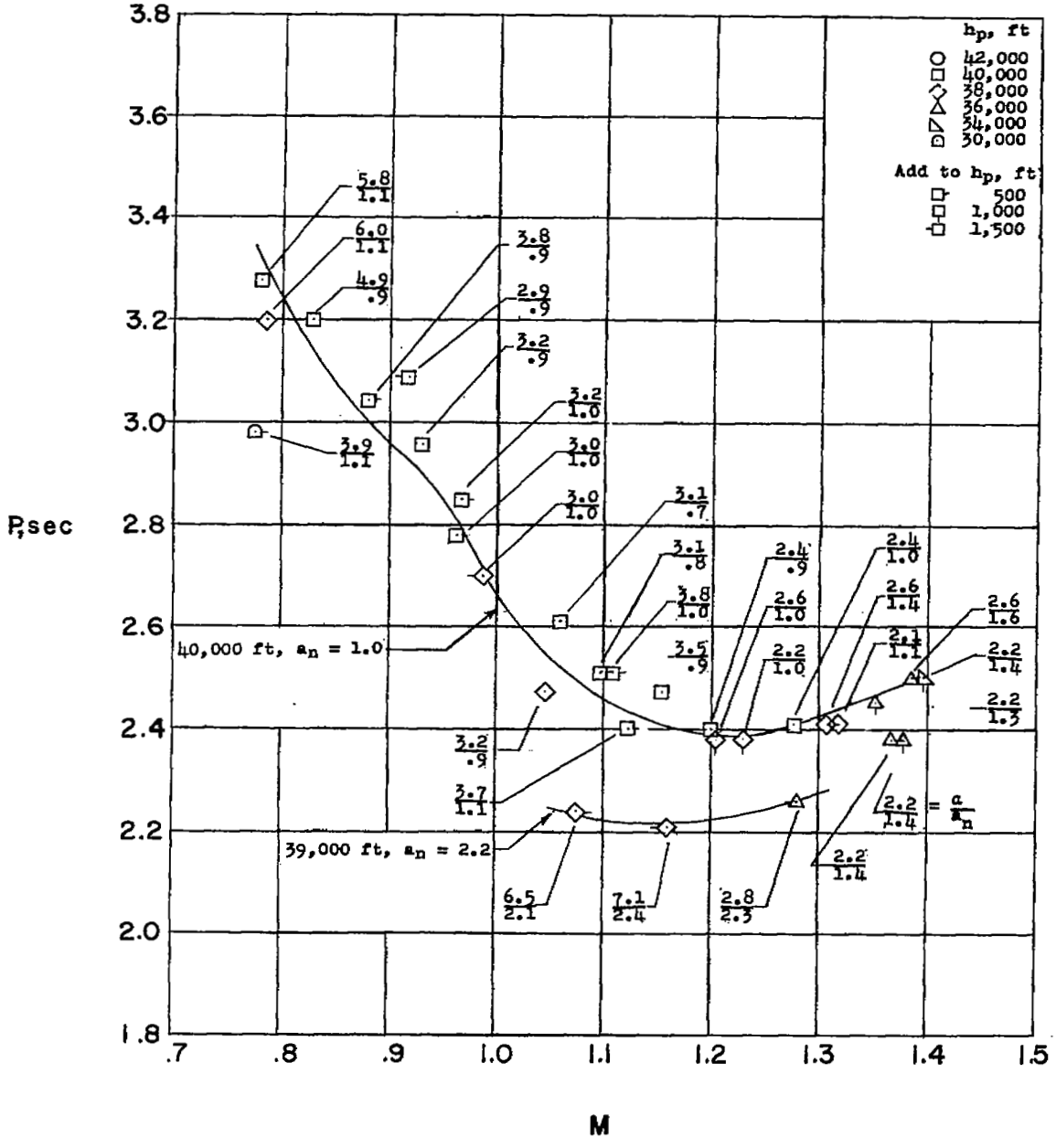

(a) Period characteristics.

Figure 21.- Period and damping characteristics of the airplane as functions of Mach number, altitude, and angle of attack per load factor. Configuration B.

[redacted]

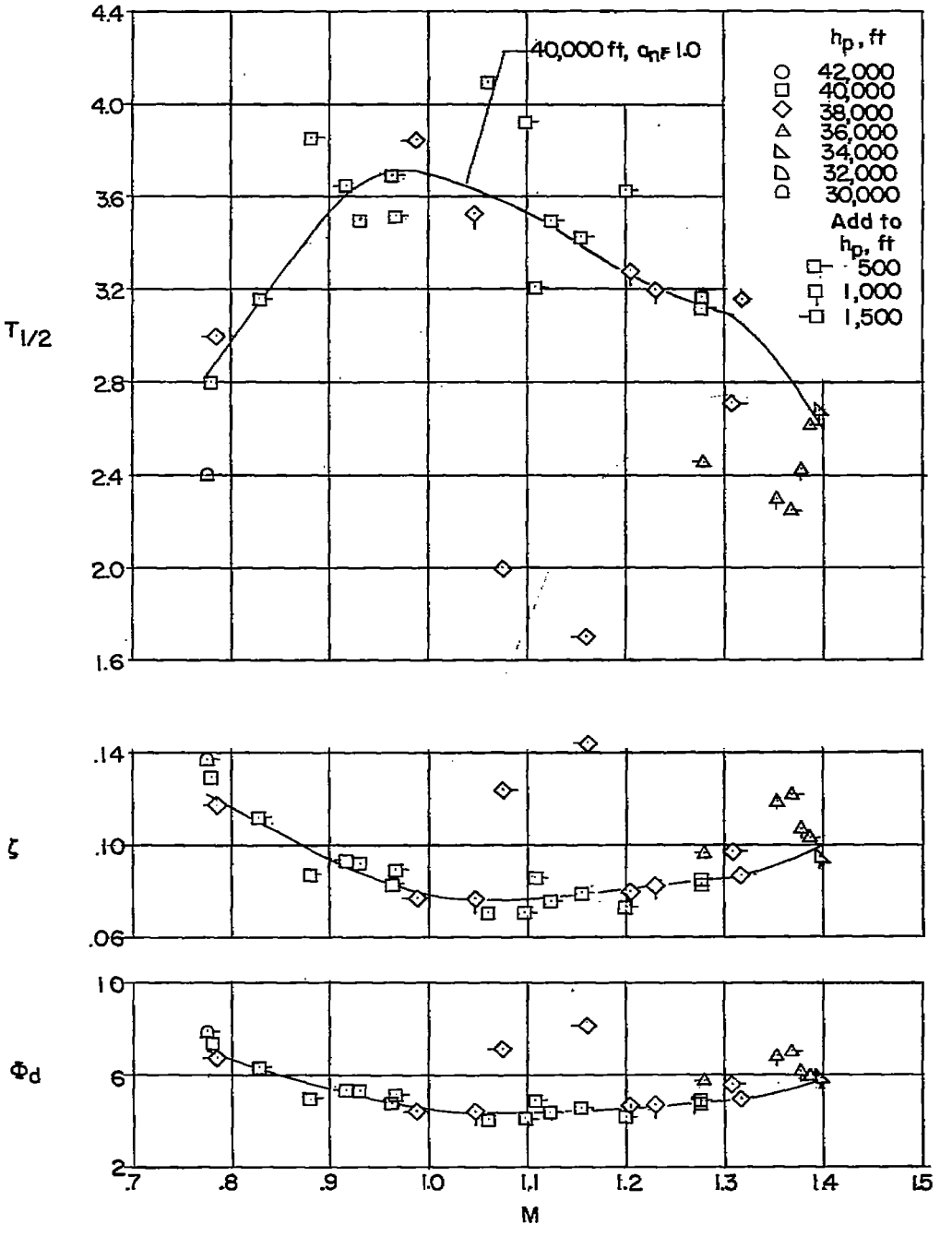

(b) Damping characteristics.

Figure 21.- Concluded.

[redacted]

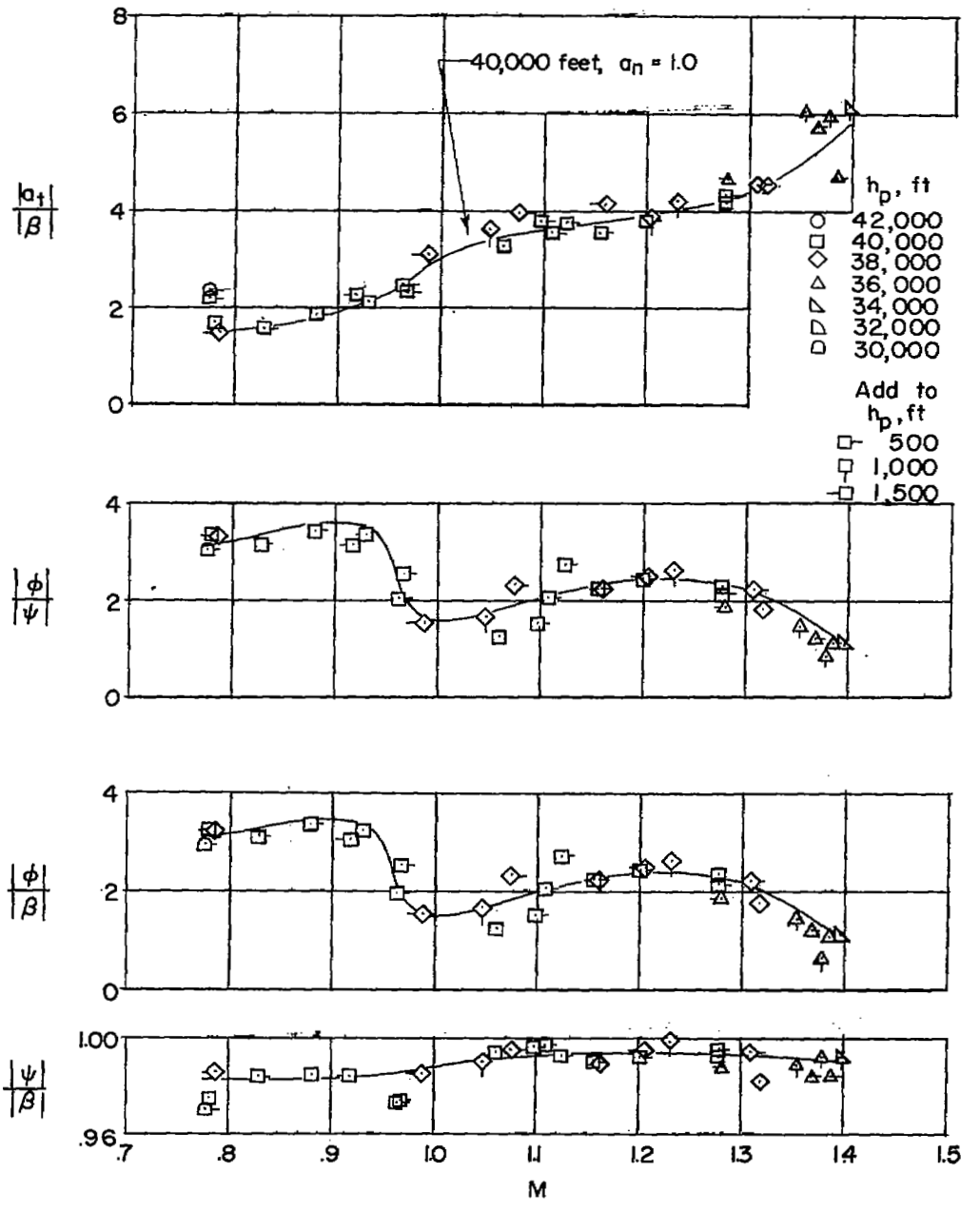

(a) Amplitude ratio characteristics.

Figure 22.- Amplitude ratio and phase angle characteristics of the airplane at its natural frequency as functions of Mach number and altitude. Configuration B.

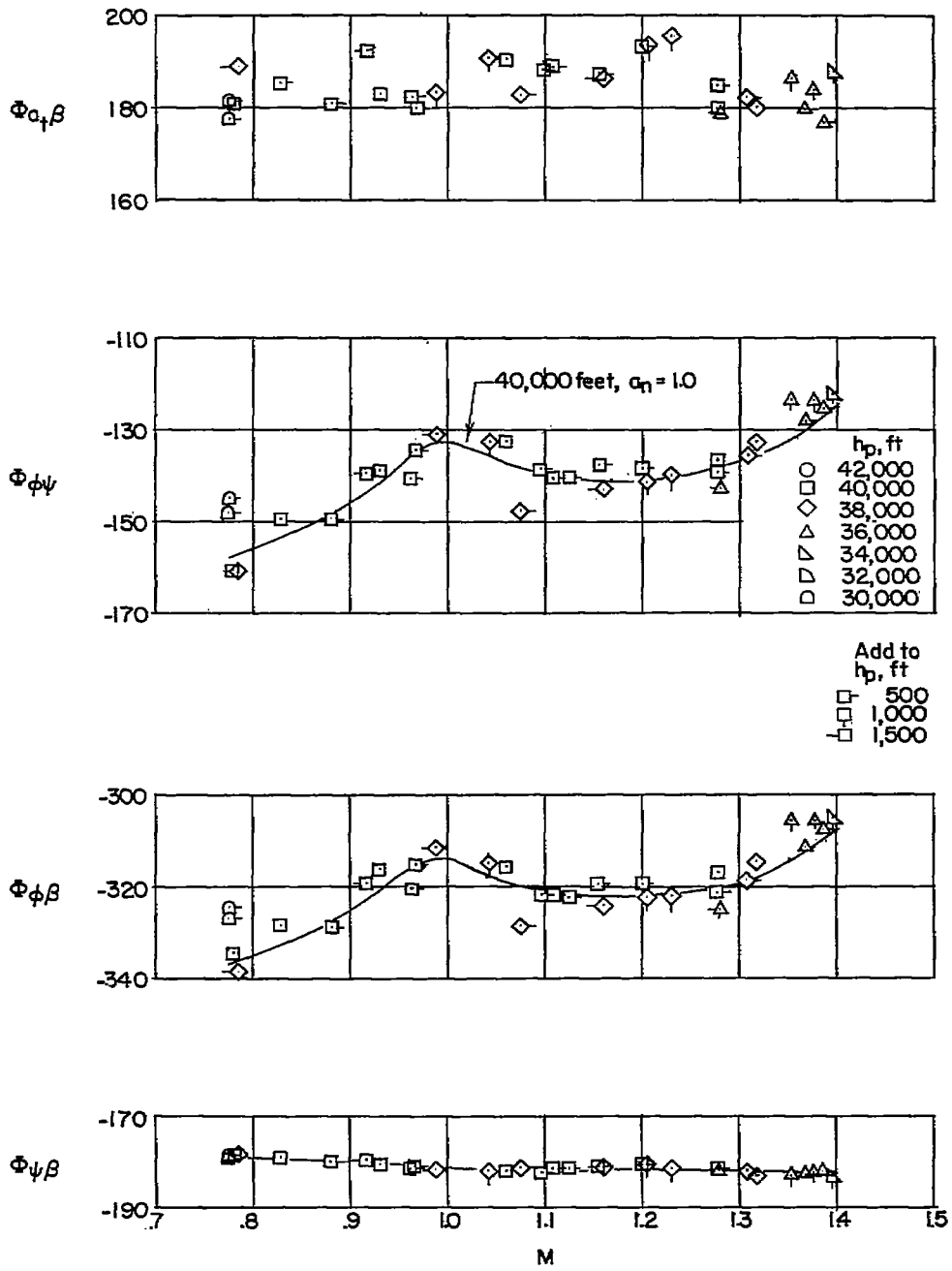

(b) Phase angle characteristics.

Figure 22.- Concluded.

[redacted]

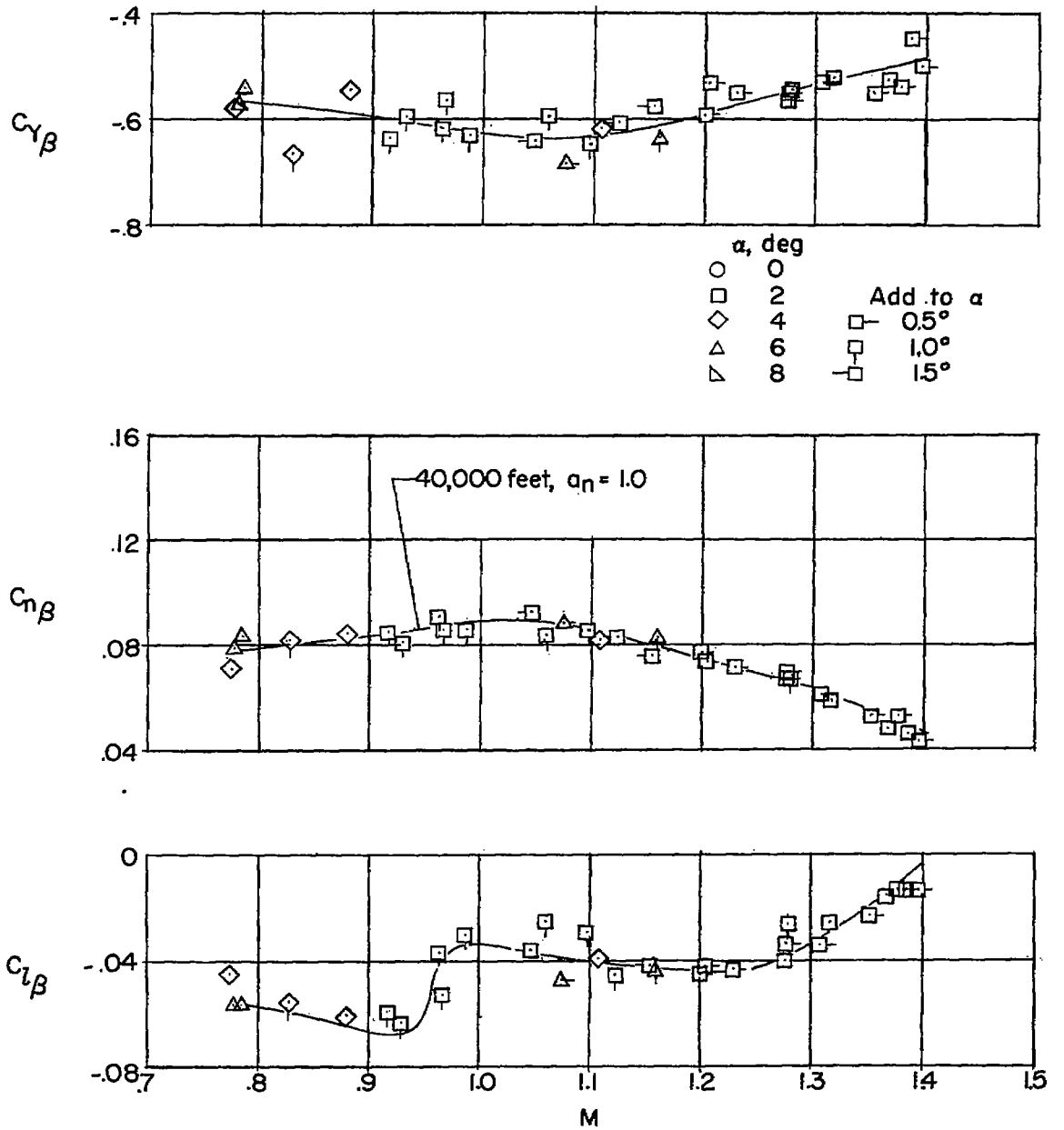

(a) Static derivatives.

Figure 23.- Variation of static and dynamic lateral stability derivatives with Mach number. Configuration B.

[redacted]

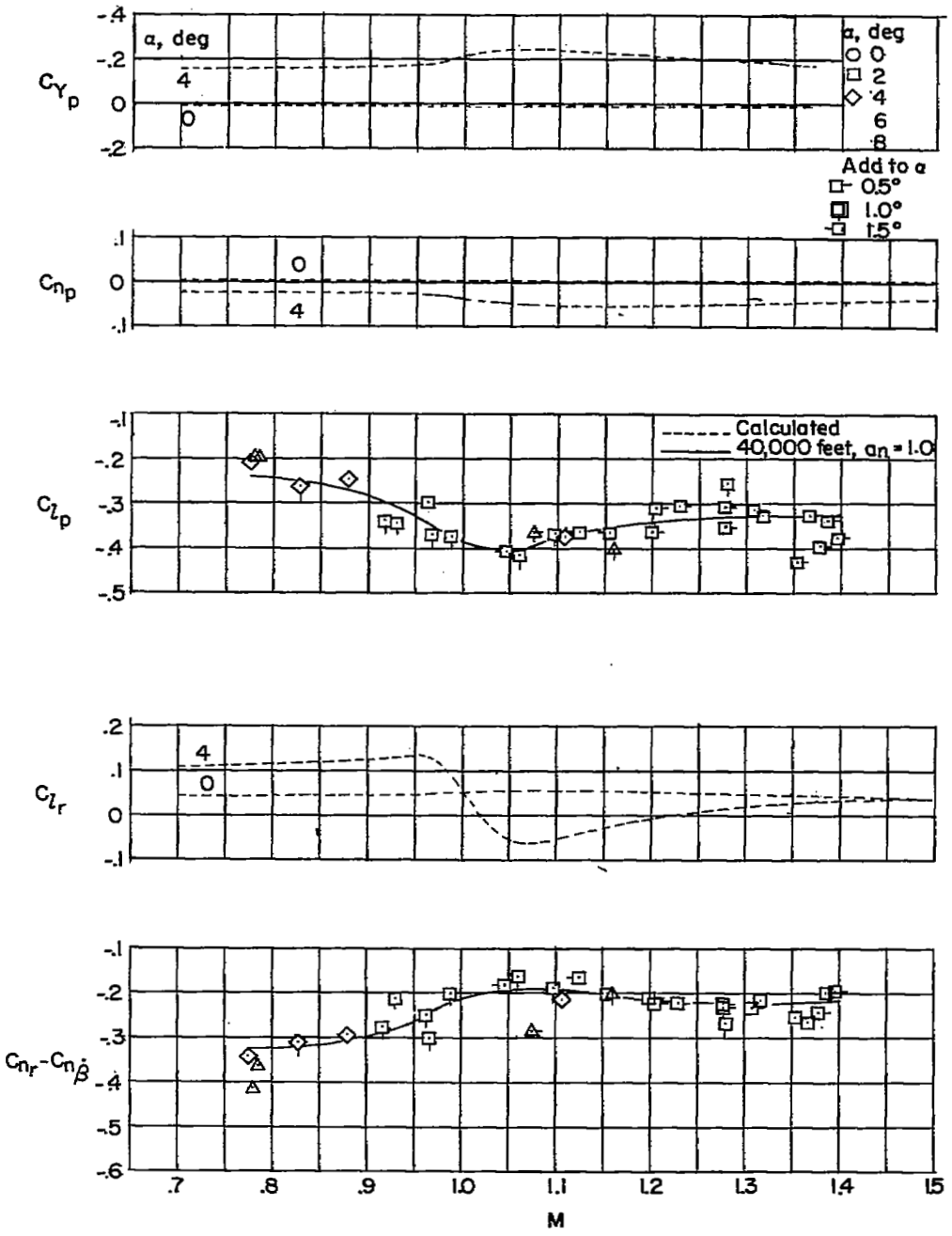

(b) Dynamic derivatives.

Figure 23.- Concluded.

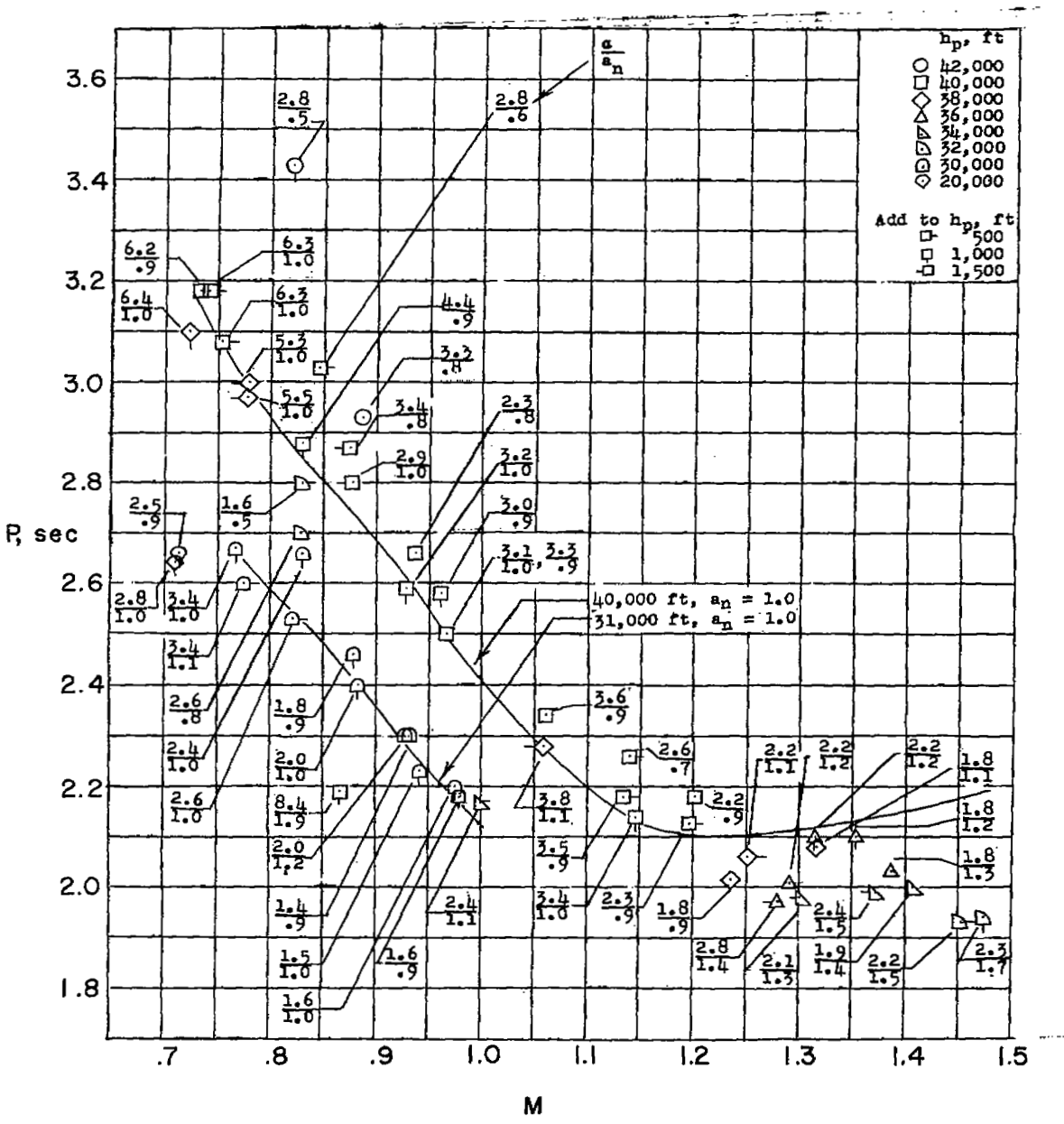

(a) Period characteristics.

Figure 24.- Period and damping characteristics of the airplane as functions of Mach number, altitude, and angle of attack per load factor. Configuration C.

[redacted]

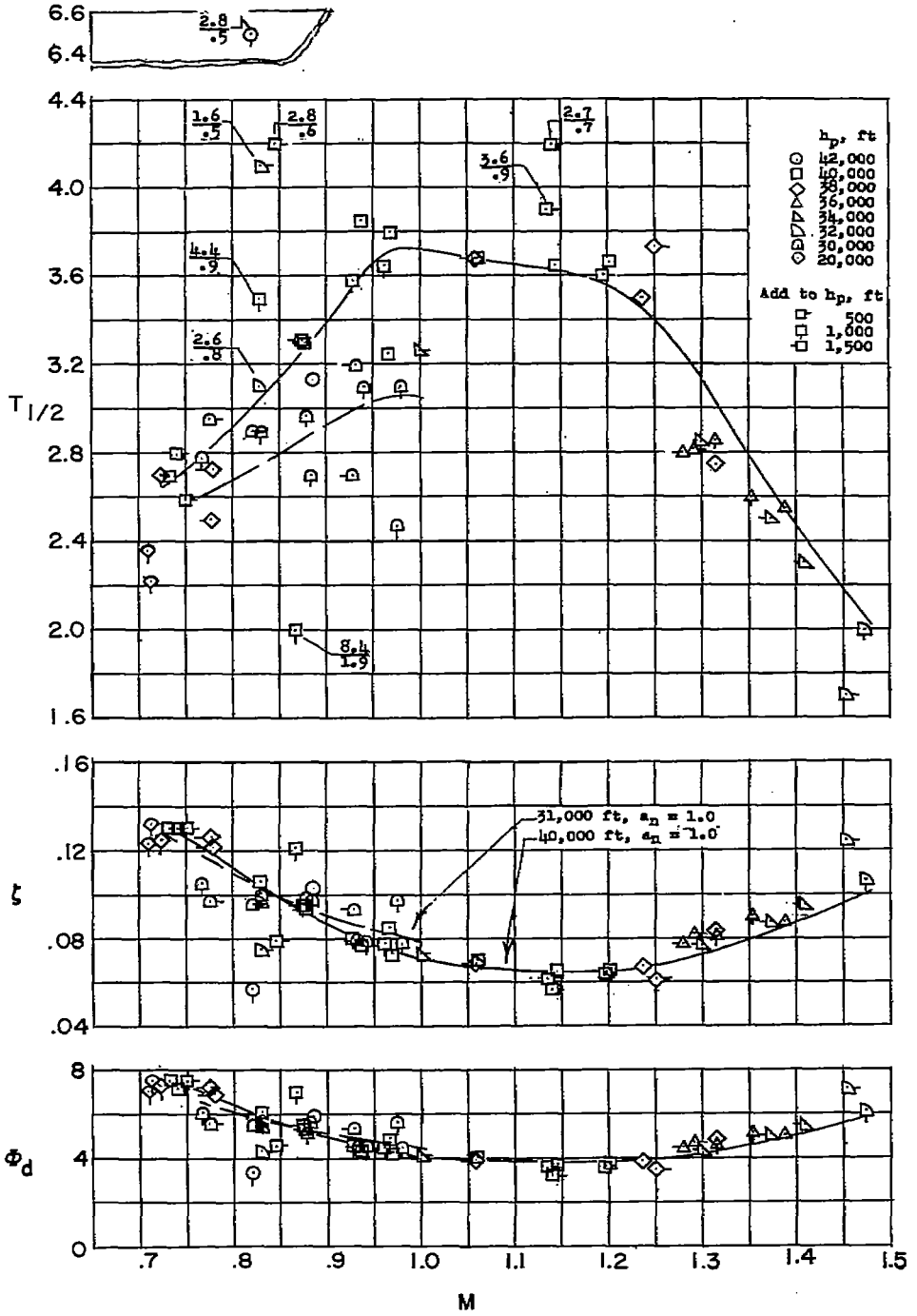

(b) Damping characteristics.

Figure 24.- Concluded.

[redacted]

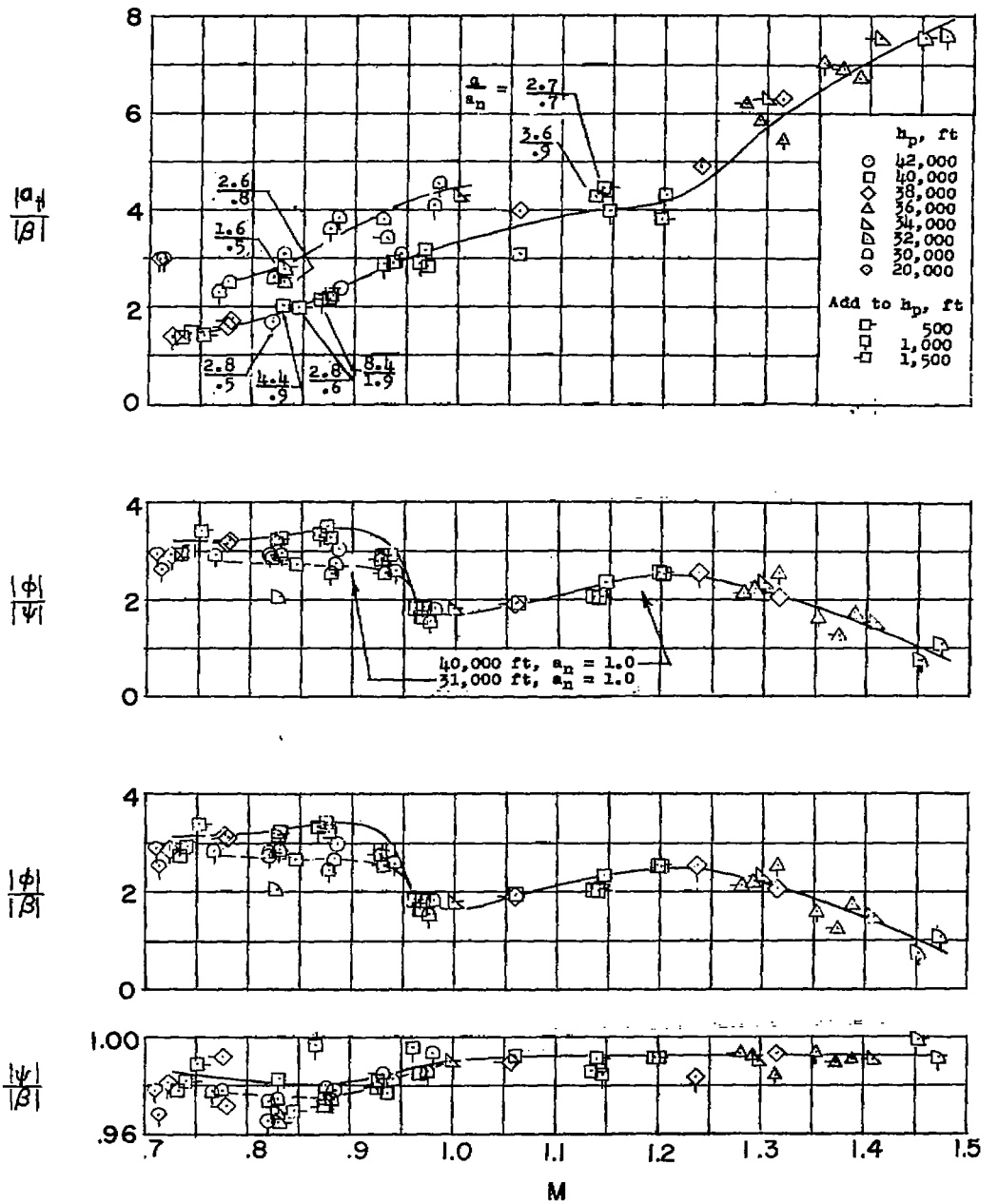

(a) Amplitude ratio characteristics.

Figure 25.- Amplitude ratio and phase angle characteristics of the airplane at its natural frequency as functions of Mach number, altitude, and angle of attack per load factor. Configuration C.

[redacted]

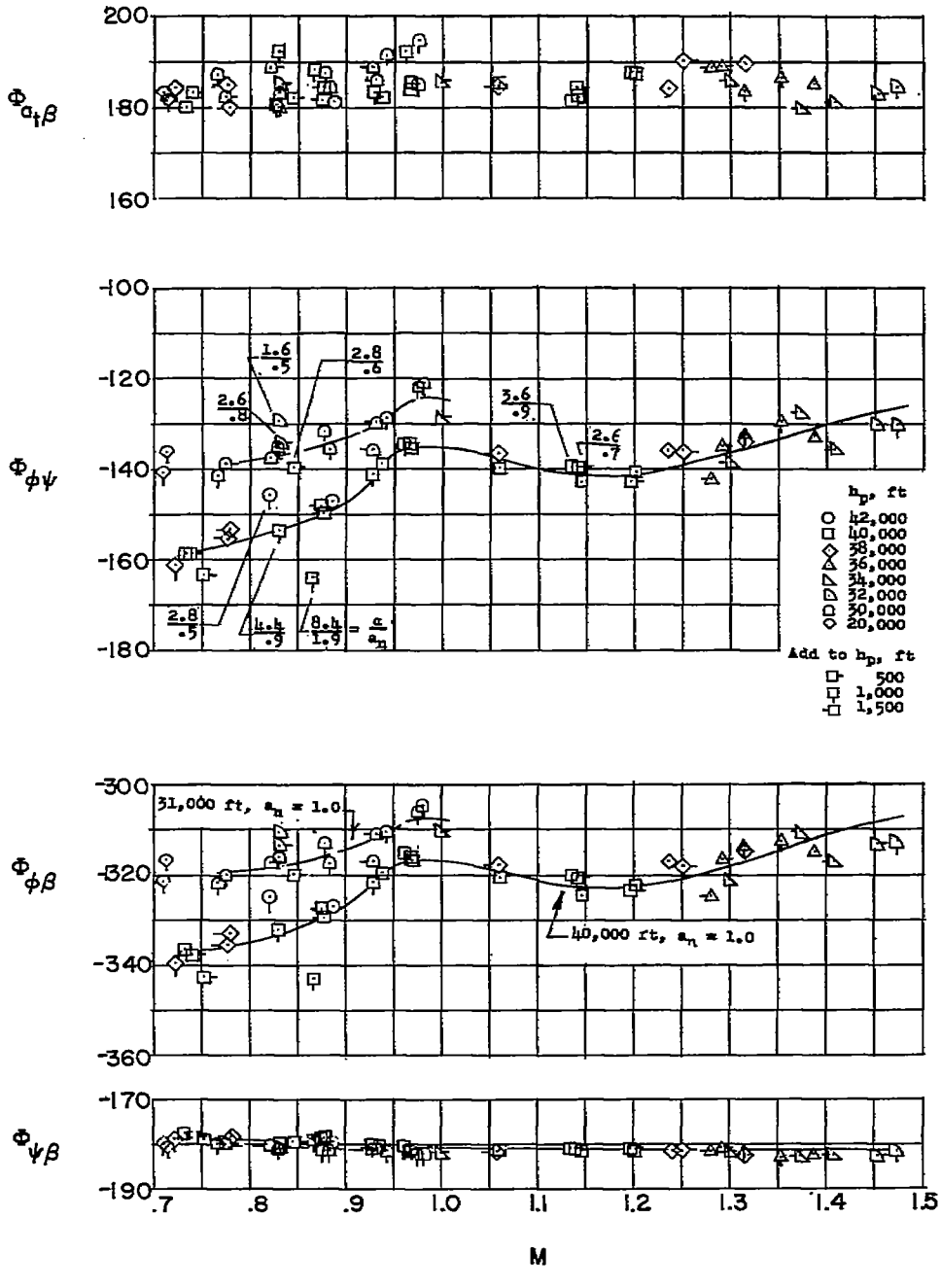

(b) Phase angle characteristics.

Figure 25.- Concluded.

[redacted]

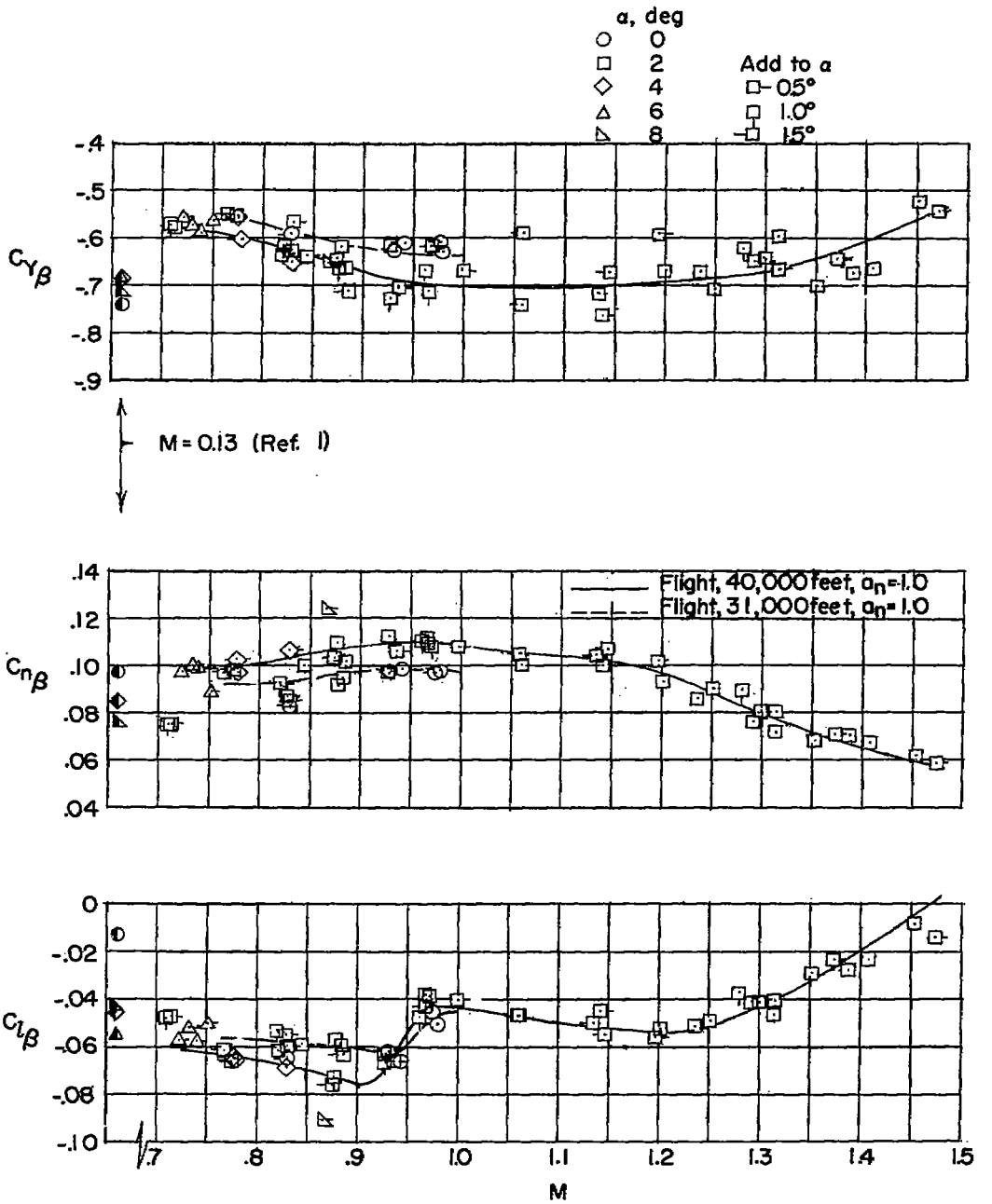

(a) Static derivatives.

Figure 26.- Variation of static and dynamic lateral stability derivatives with Mach number. Configuration C.

[redacted]

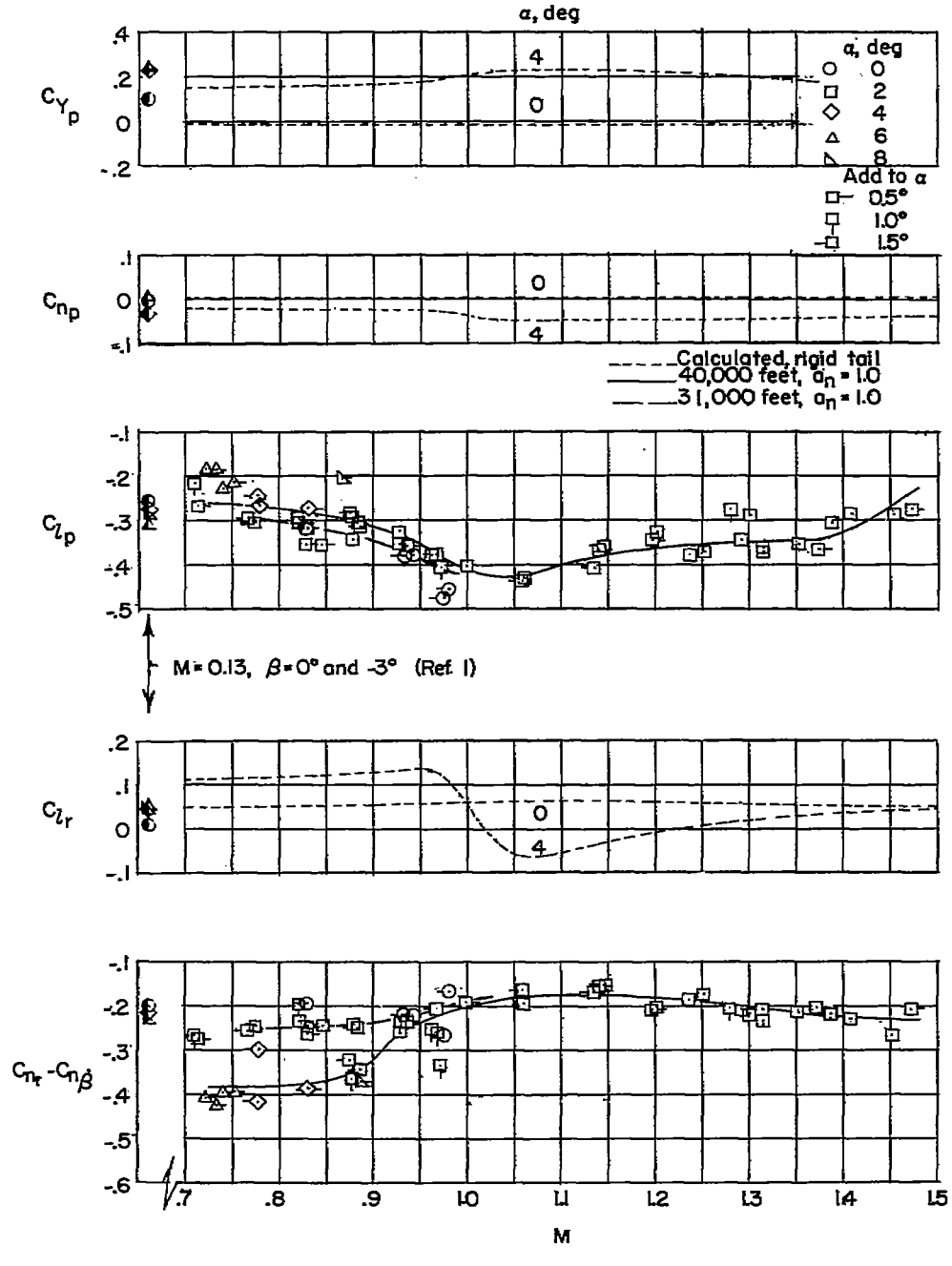

(b) Dynamic derivatives.

Figure 26.- Concluded.

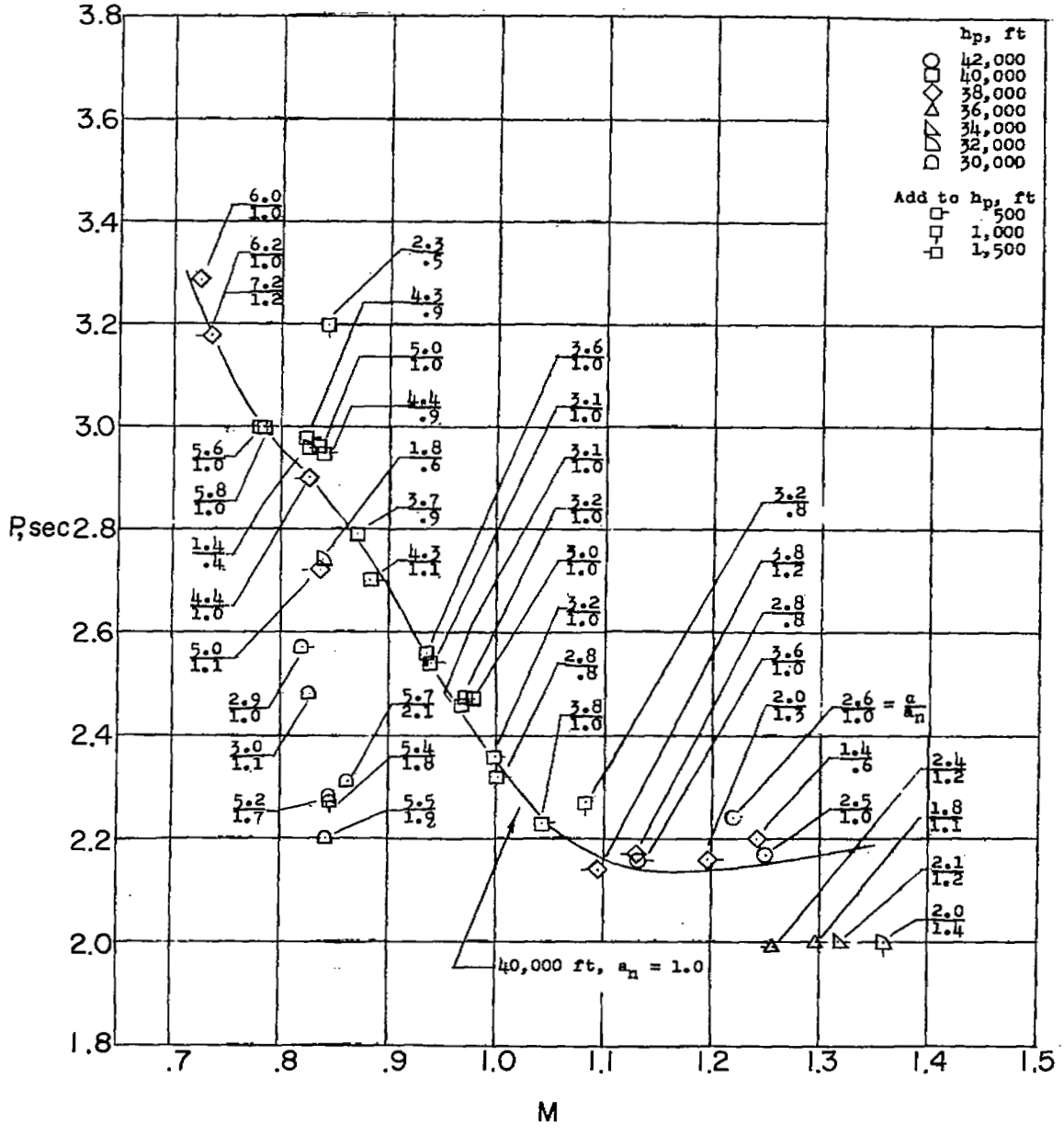

(a) Period characteristics.

Figure 27.- Period and damping characteristics of the airplane as functions of Mach number, altitude, and angle of attack per load factor. Configuration D.

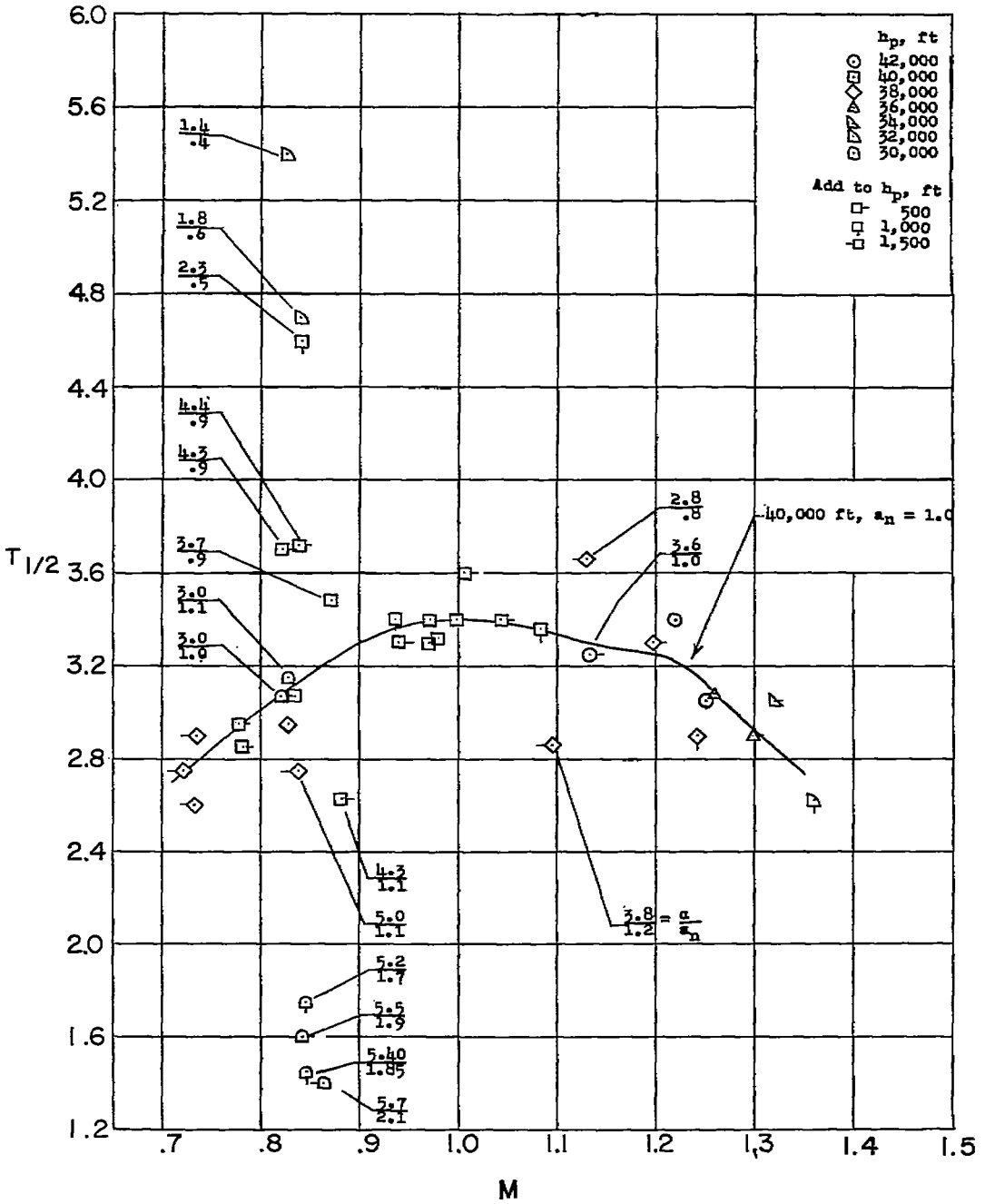

(b) Damping characteristics.

Figure 27.- Continued.

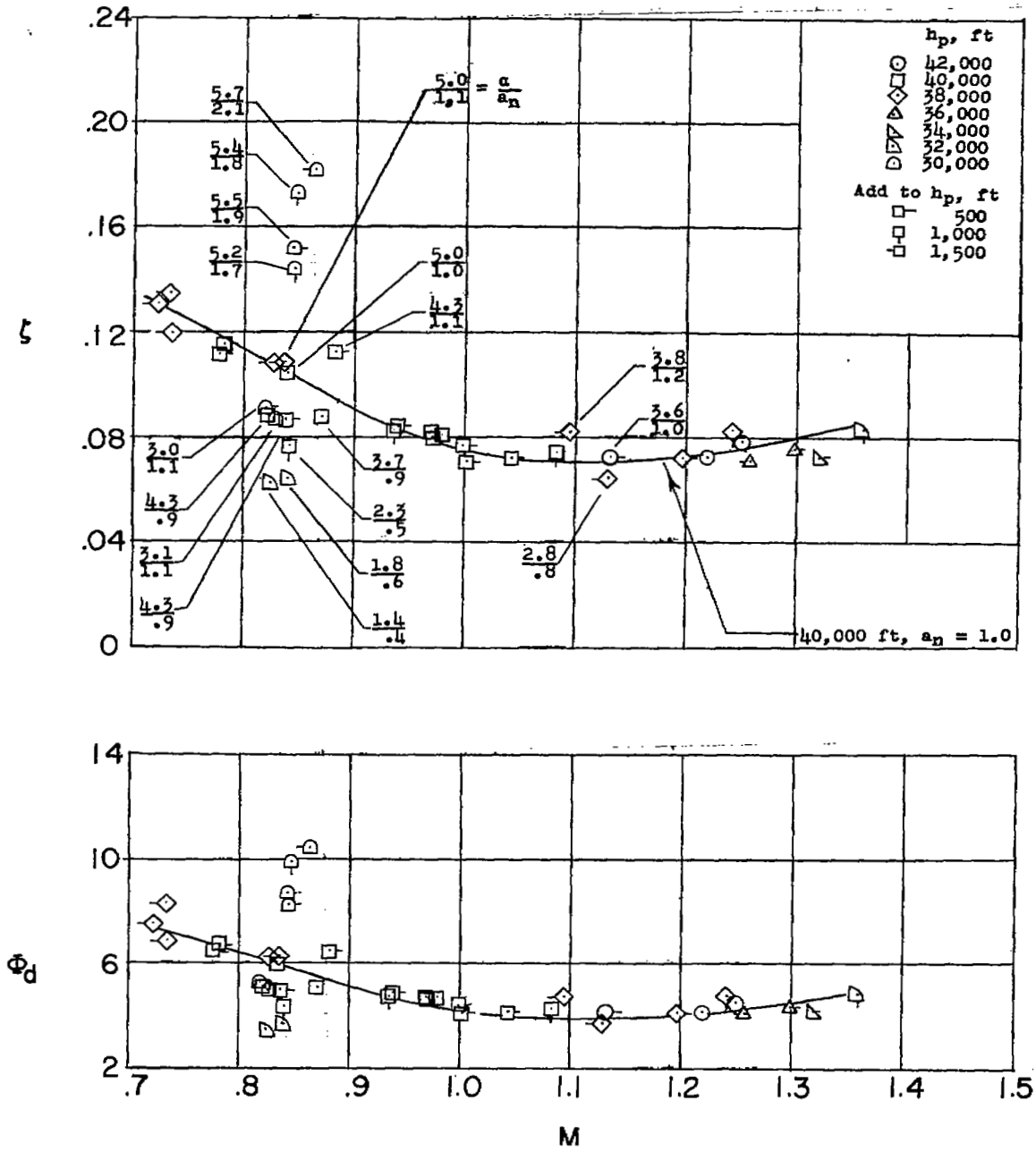

(c) Damping characteristics.

Figure 27.- Concluded.

[redacted]

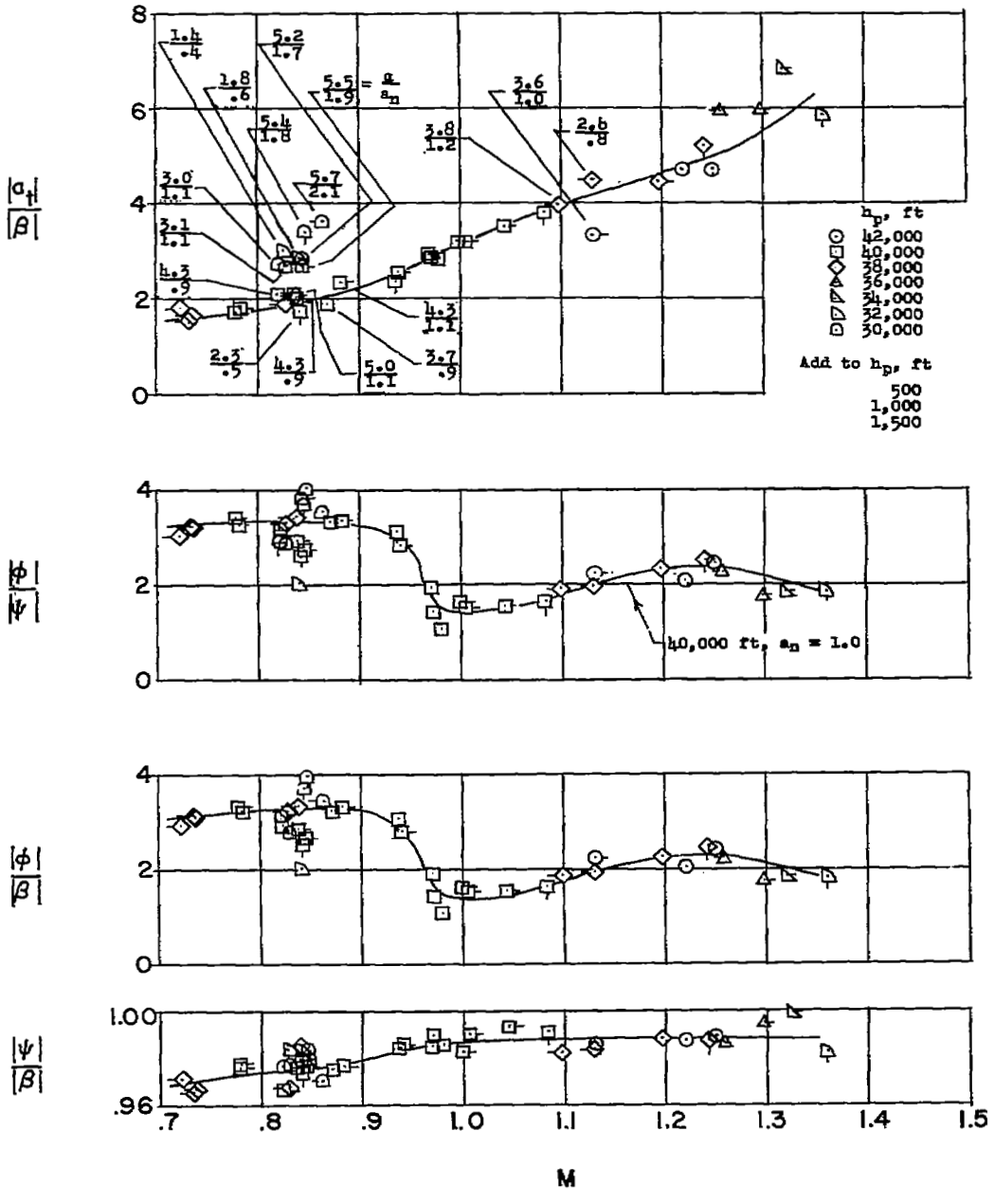

(a) Amplitude ratio characteristics.

Figure 28.- Amplitude ratio and phase angle characteristics of the airplane at its natural frequency as functions of Mach number, altitude, and angle of attack per load factor. Configuration D.

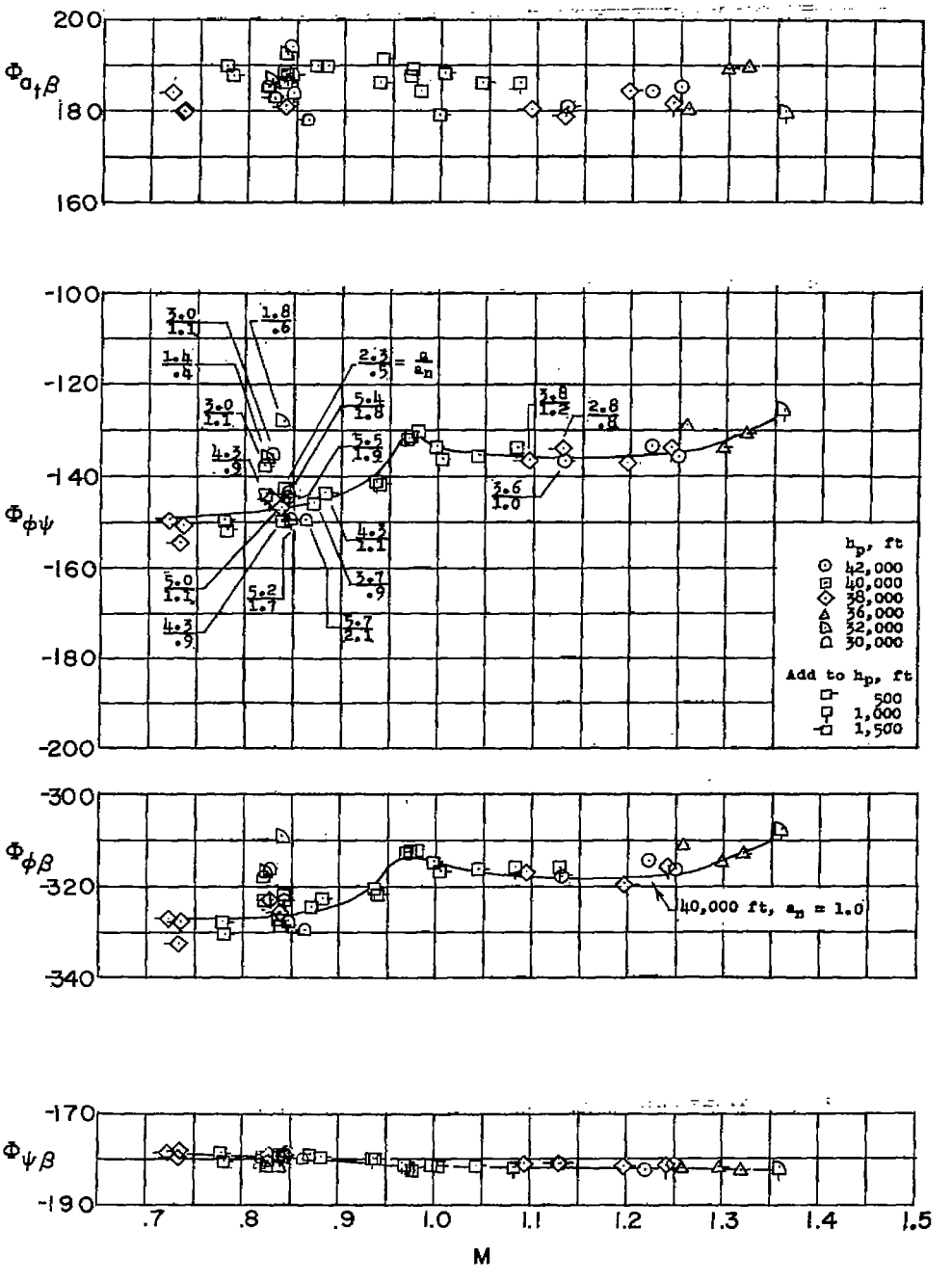

(b) Phase angle characteristics.

Figure 28.- Concluded.

[redacted]

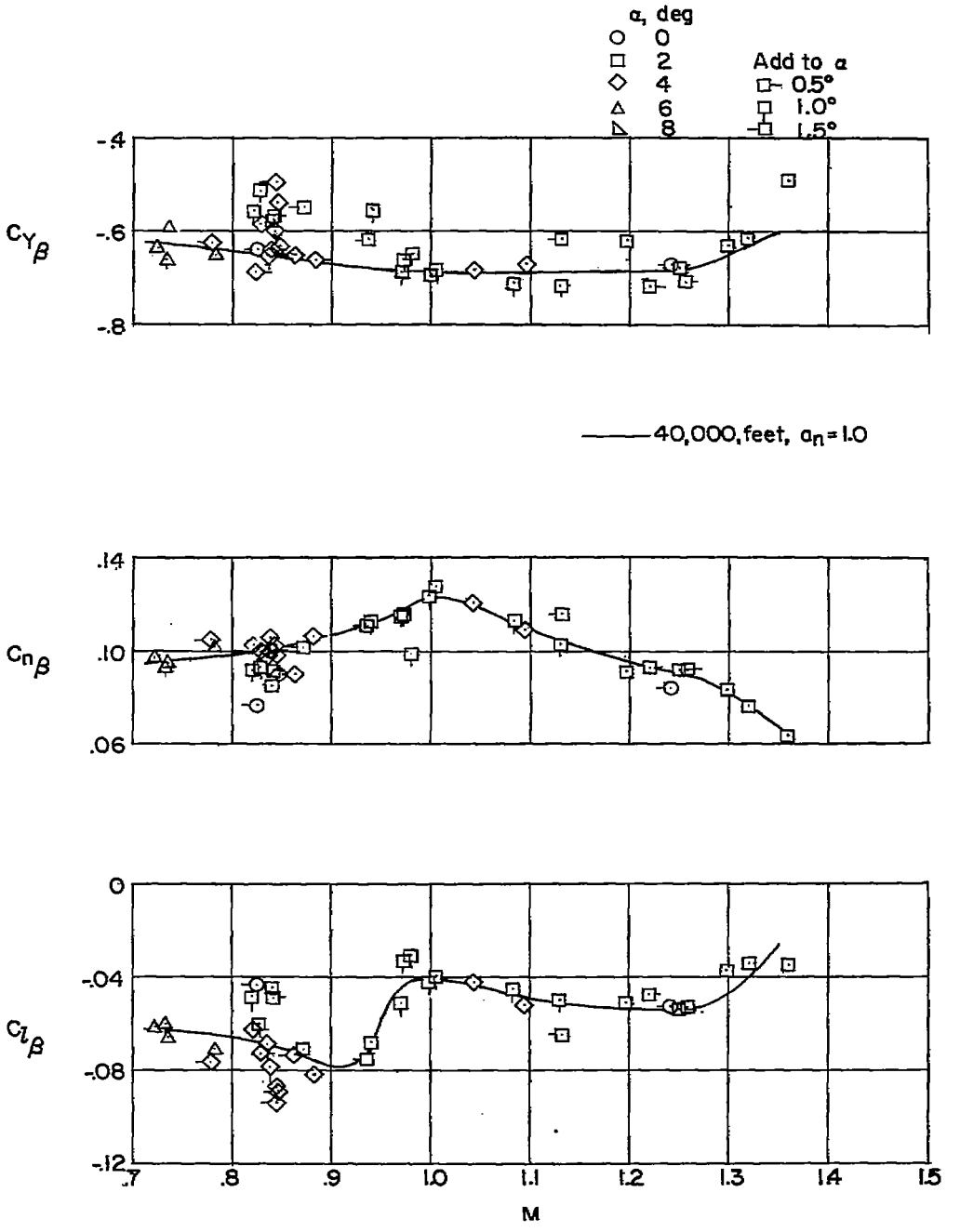

(a) Static derivatives.

Figure 29.- Variation of static and dynamic lateral stability derivatives with Mach number. Configuration D.

[redacted]

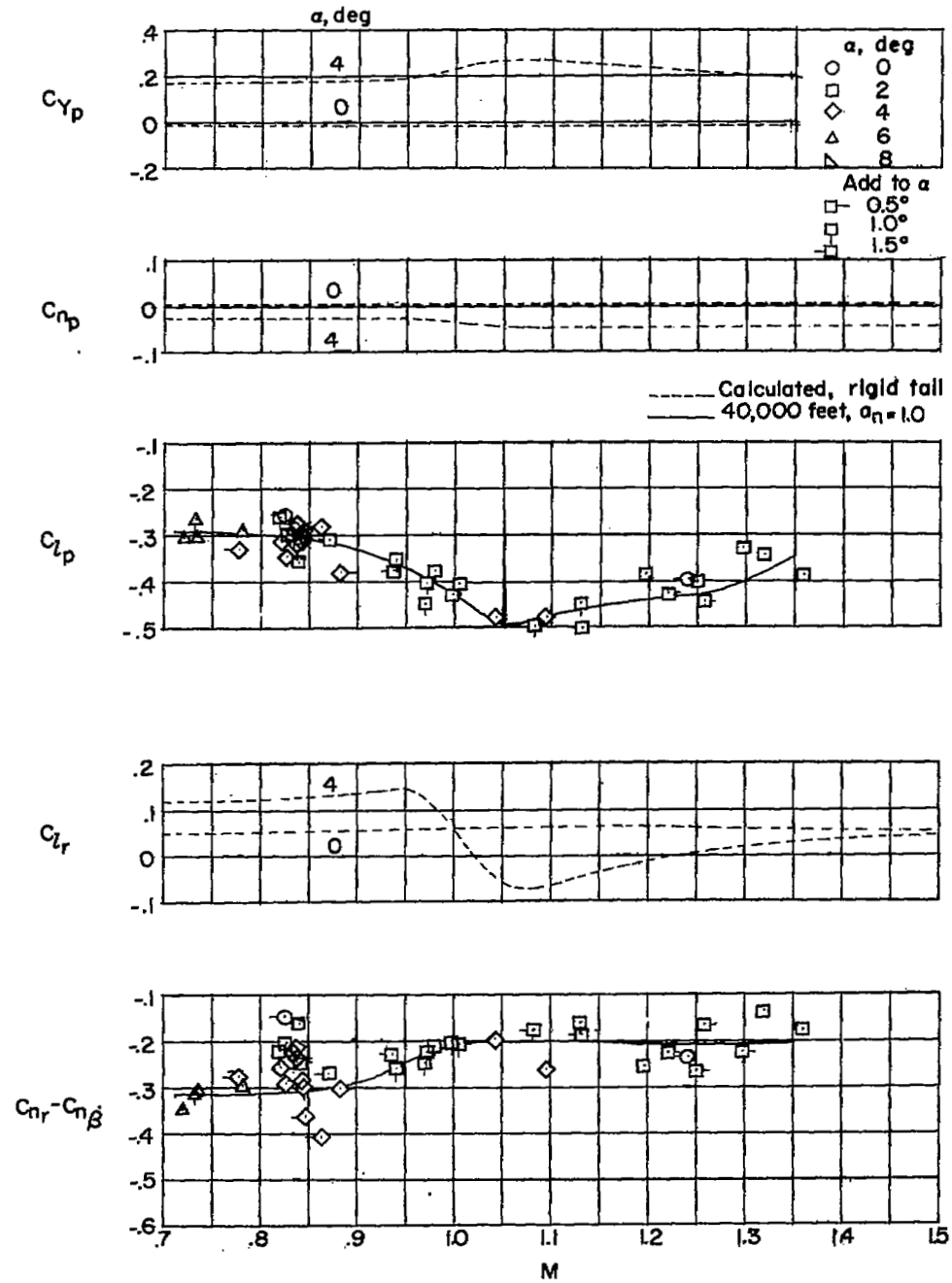

(b) Dynamic derivatives.

Figure 29.- Concluded.

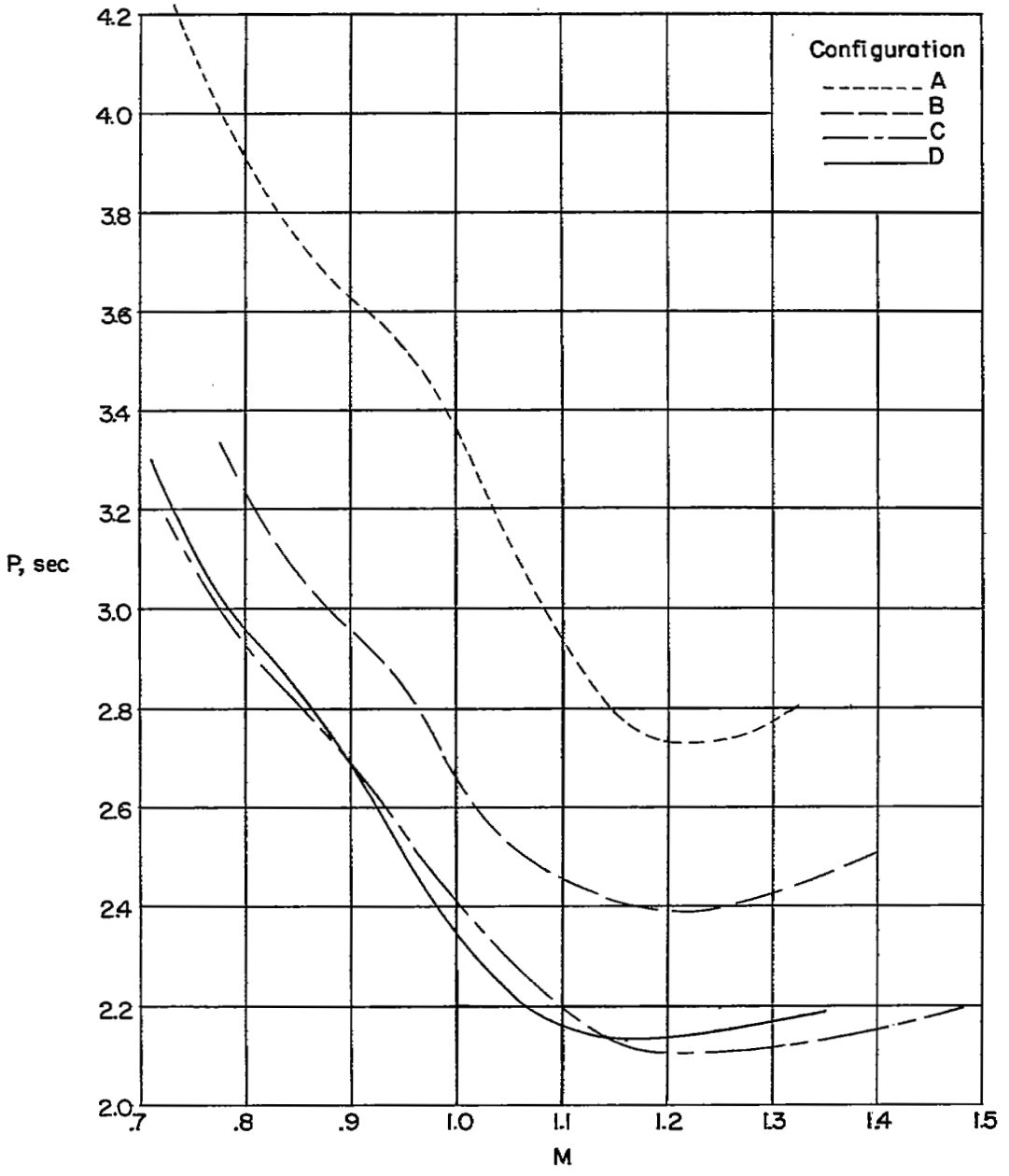

(a) Period characteristics.

Figure 30.- Summary of period and damping characteristics of configurations A, B, C, and D as functions of Mach number at h_p = 40,000 feet; a_n = 1.0.

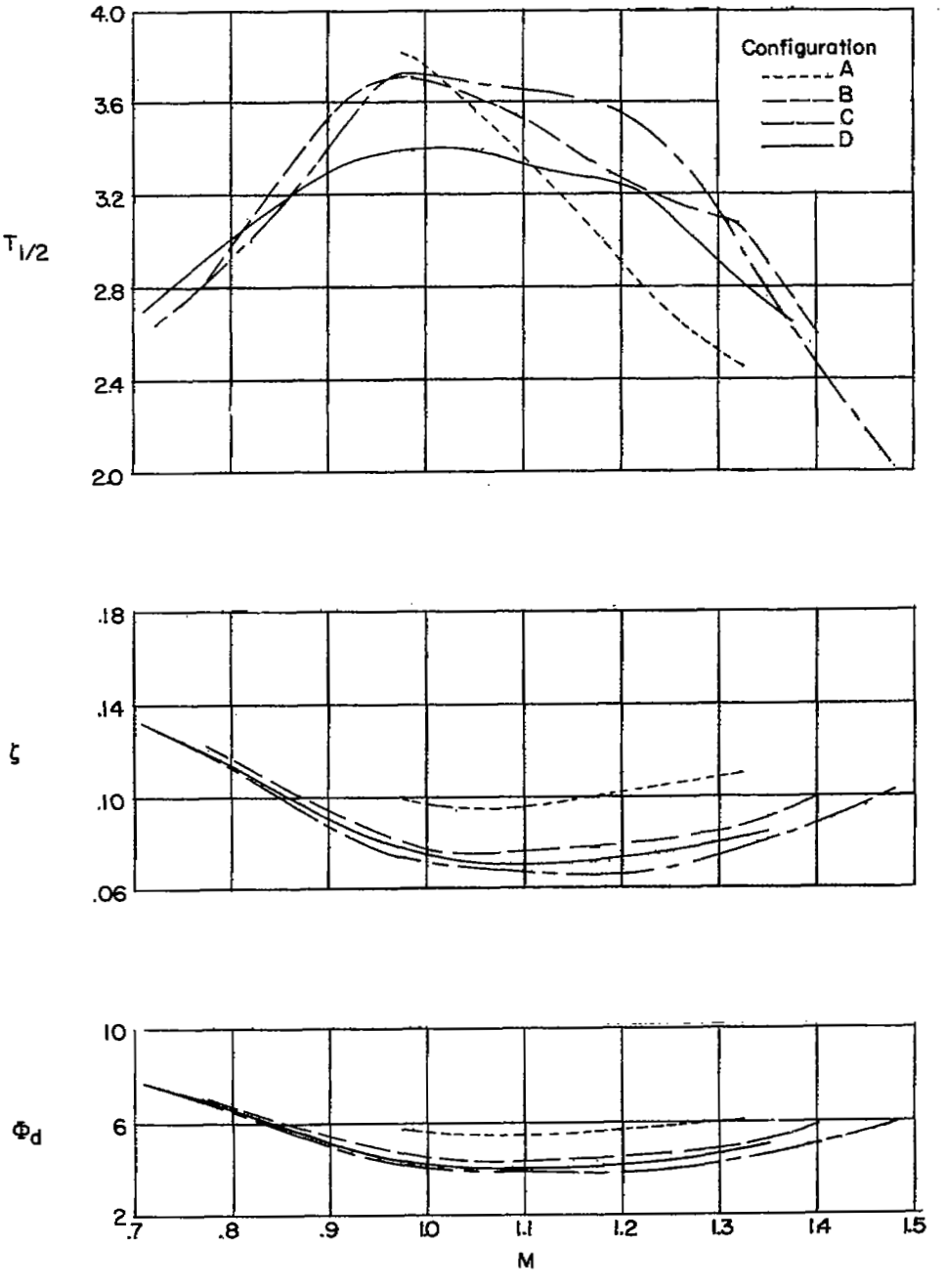

(b) Damping characteristics.

Figure 30.- Concluded.

[redacted]

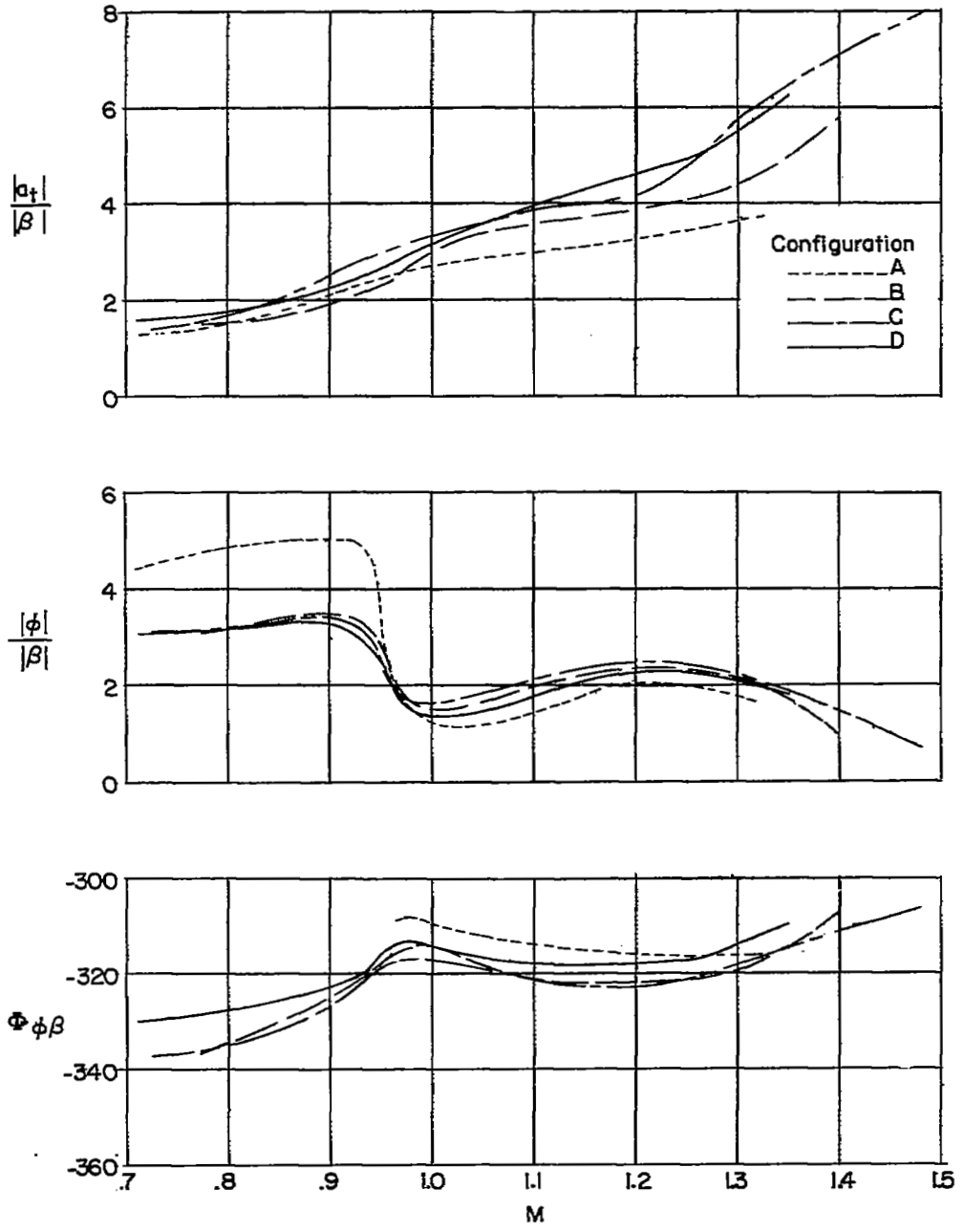

Figure 31.- Summary of the characteristics of the amplitude ratios $\frac{|a_t|}{|\beta|}$ and $\frac{|\varphi|}{|\beta|}$, and the phase angle $\Phi_{\varphi\beta}$ of configurations A, B, C, and D as functions of Mach number at h_p = 40,000 feet; a_n = 1.0.

[redacted]

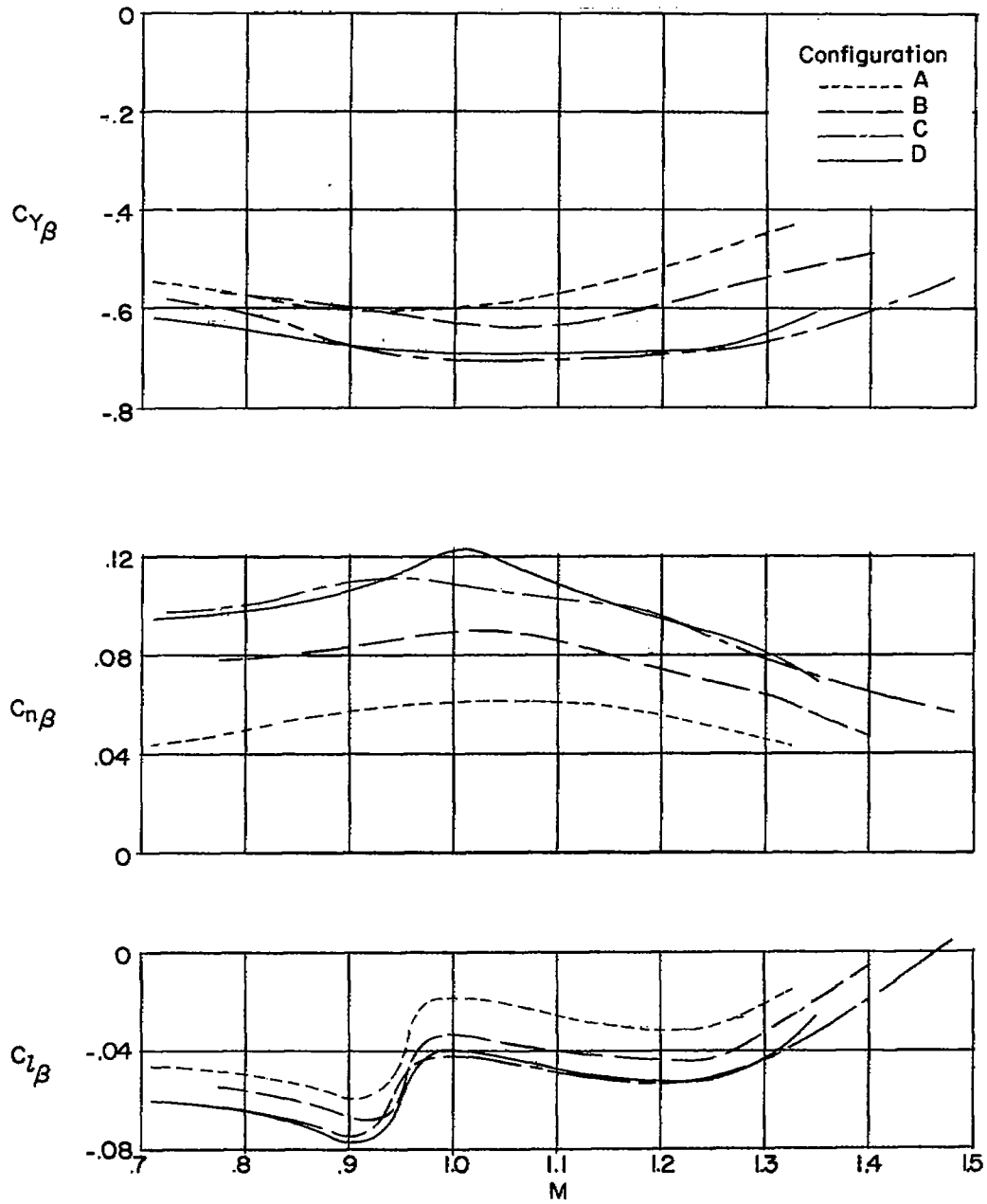

(a) Static derivatives.

Figure 32.- Summary of the lateral stability derivative characteristics of configurations A, B, C, and D as functions of Mach number at h_p = 40,000 feet; a_n = 1.0.

[redacted]

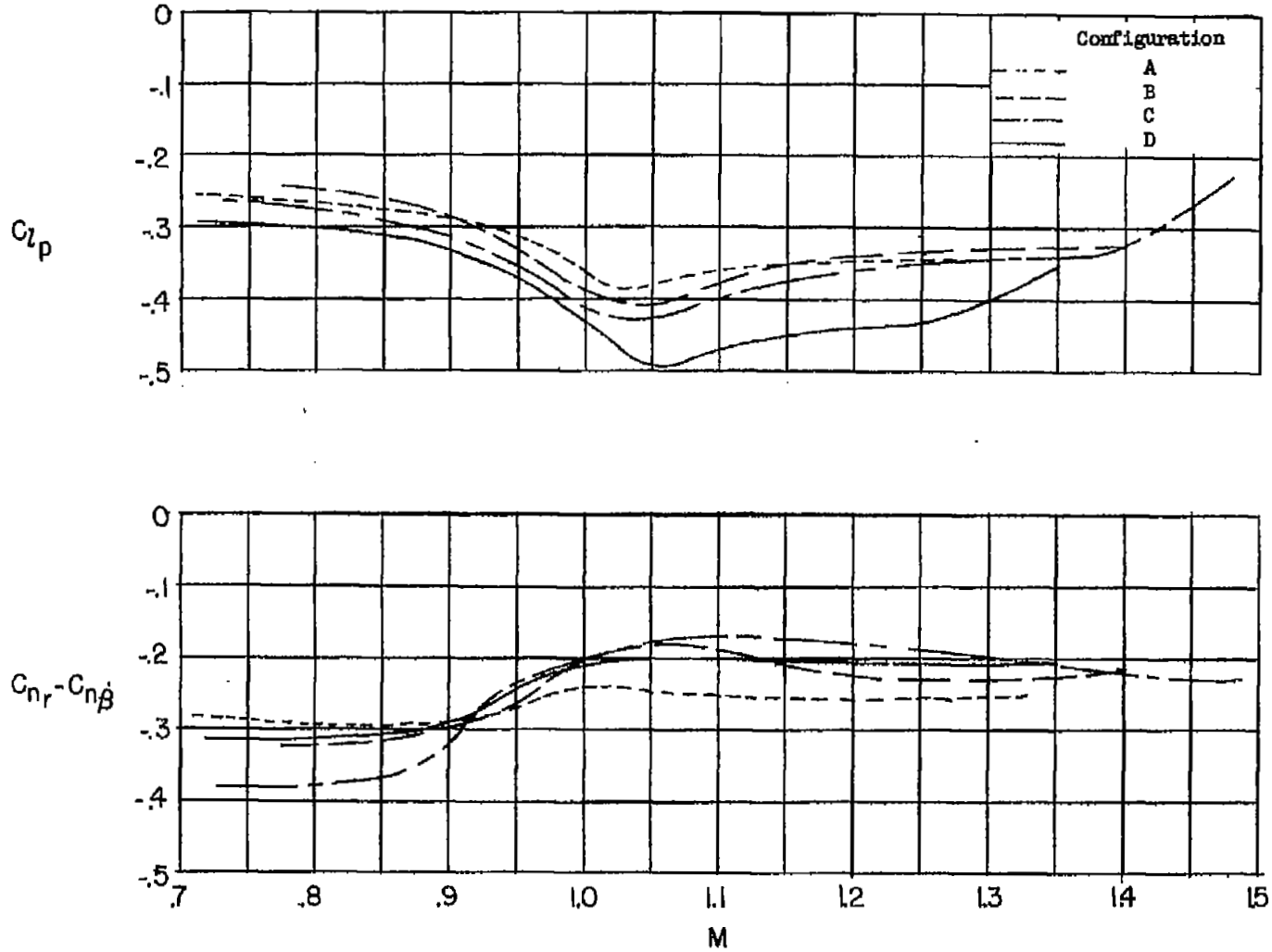

(b) Dynamic derivatives.

Figure 32.- Concluded.

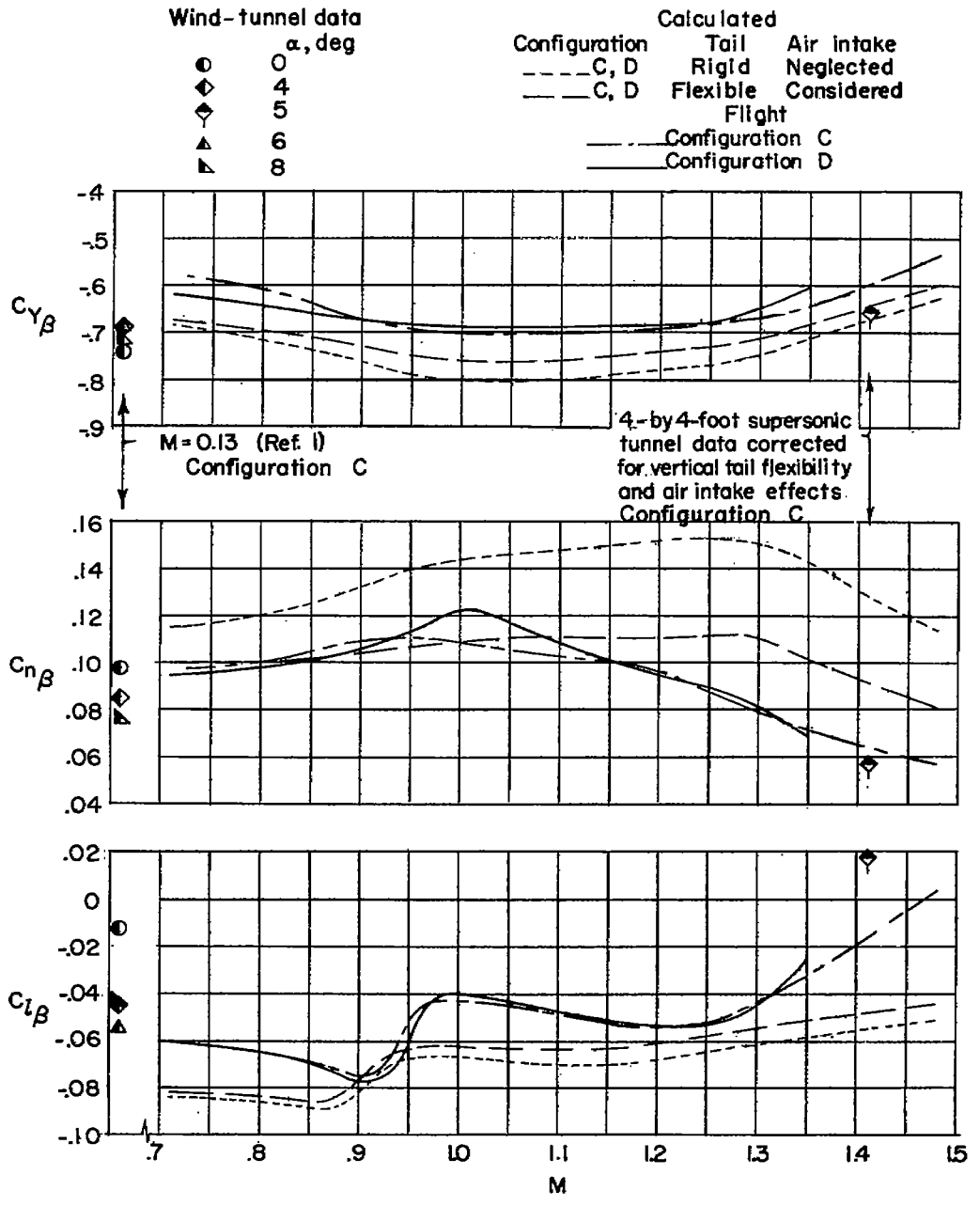

(a) Static derivatives.

Figure 33.- Comparison of the variation of the lateral stability derivatives of configurations C and D with Mach number as determined from flight with calculated variation. h_p = 40,000 feet; a_n = 1.0.

[redacted]

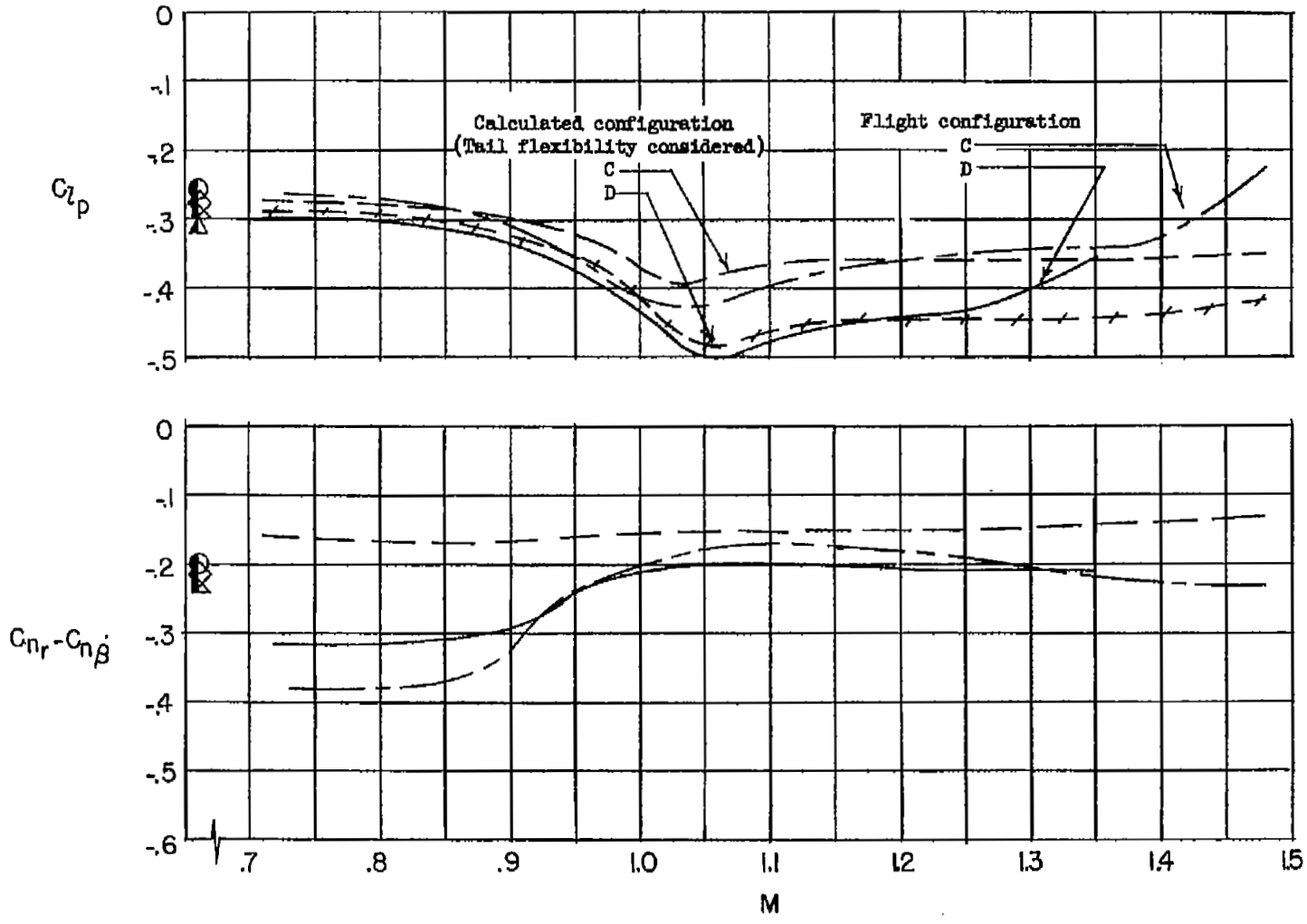

(b) Dynamic derivatives.

Figure 33.- Concluded.

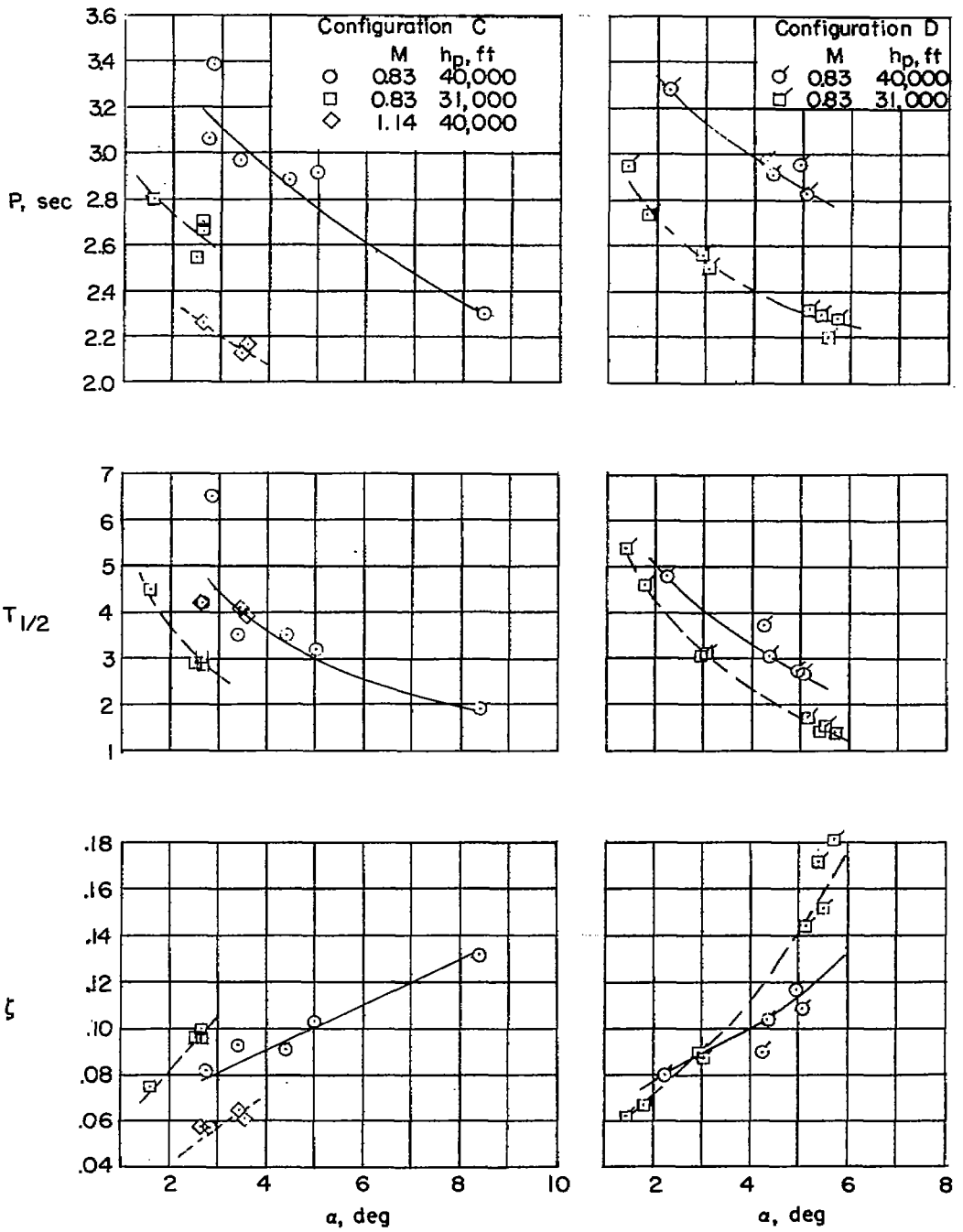

Figure 34.- Period, damping, amplitude ratio $\frac{|\varphi|}{|\beta|}$, and phase angle $\Phi_{\varphi\beta}$ characteristics as functions of angle of attack at constant Mach number. Configurations C and D.

[redacted]

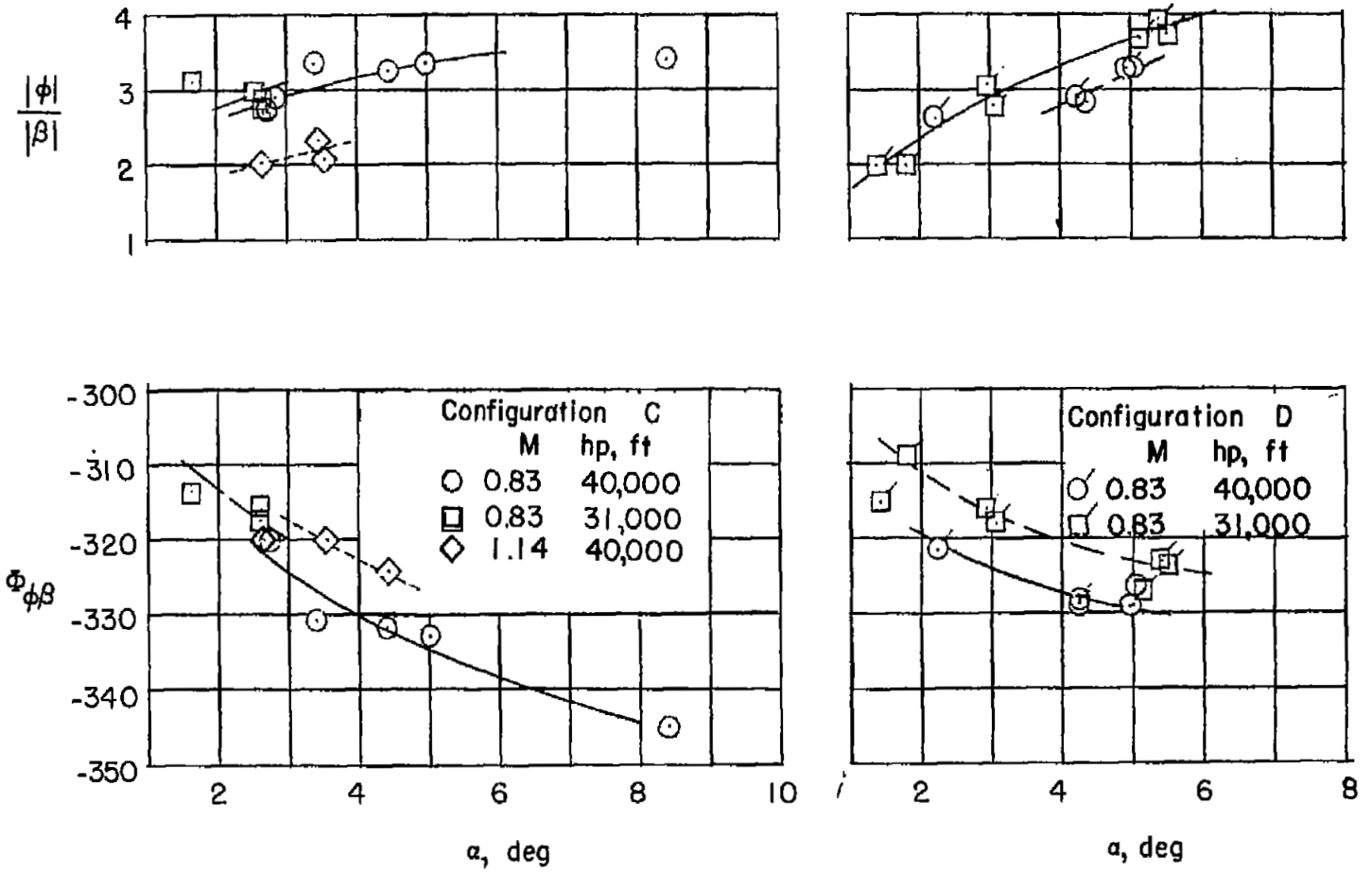

Figure 34.- Concluded.

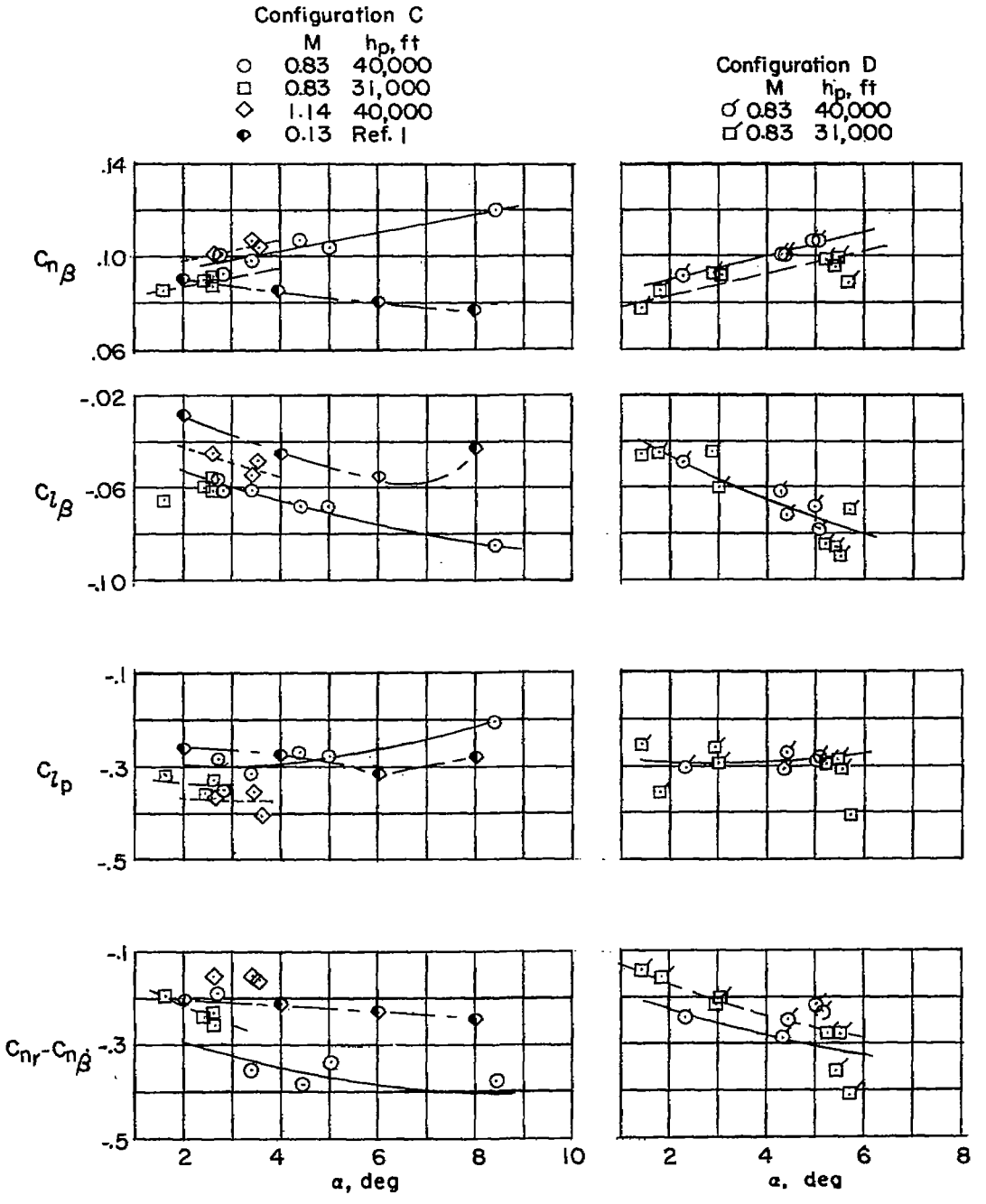

Figure 35.- Static and dynamic lateral stability derivative characteristics as functions of angle of attack at constant Mach number. Configurations C and D.